Chapter 5

Material efficient growth of CIGSe on patterned substrates

In chapter 3, an effective method to characterize and monitor the morphology of thin films was developed for sequential processes. With this, it was possible to measure the composition and monitor the phases formed in the individual micro-dots that make up the arrays of the substrate. In chapter 4, a co-evaporation process was used to grow the absorber on the patterned substrate, as it should yield CIGSe solar cells with high PCEs. It was found that the patterned substrates enhance the diffusion of alkali dopants through the micro-dots. Based on these results, chapter 5 investigates the synthesis of CIGSe absorbers, in patterned substrates, using material efficient methods. The latter are typically more challenging to control and thus harder to achieve high quality material compared to the co-evaporation case. Two synthesis routes are explored. In the first case, the Cu(In,Ga) metal precursor is deposited, inside the micro-dots, by magnetron sputtering, followed by an annealing in a Se-containing atmosphere to form the CIGSe absorber. In the second case, a two-step electrodeposition process is chosen to grow first the Cu layer and second the In and Ga layer inside the micro-dots. Similarly to the first case, the CIGSe absorber are formed by an annealing in a Se-containing atmosphere. For the two cases, Cu-rich (CGI > 1.0) and Cu-poor (CGI < 1.0) precursors are investigated. The aim is to investigate the layer's morphology at each step of the two aforementioned material efficient methods and determine the relevant parameters to obtain working micro solar cells consistently. Also, the impact of using different patterned substrates is discussed. To have an overview of the synthesis routes and substrates discussed in this chapter, the reader may refer to the summary schematics (Figure 2.6) shown in chapter 2.

5.1 Sputtered solar cells

In this section, the first material efficient method, i.e. sputtering and annealing routine, is addressed, starting with the Cu-rich based solar cells. Given that the aim of the present chapter is to focus on material-efficient methods to produce micro solar cells, the Cu(In,Ga) precursor was sputtered only into the micro-dots, as detailed in section 2.1.2.

Note that the difference in the synthesis process, between the material-wasteful sputtering, discussed in section 4.3 and the material-efficient sputtering presented here, is the moment when the resist layer is removed. In the former case, the resist is removed before the sputtering of the Cu(In,Ga) metal precursor, leading to its deposition inside the micro-dots and on the SiO_2 layer. In the latter case, the resist is kept during the sputtering step and only dissolved afterwards, which results in the deposition of Cu(In,Ga) only inside of the micro-dots. The removed resist and excess precursor material can potentially be separated easily and reused, making this method material-efficient. Full details about synthesis process may be found in reference [160].

5.1.1 Cu-rich solar cells

This section is based on the publication [160], which demonstrates a proof-of-principle of working micro solar cells synthesized by sputtering, as a material efficient method.

Given that the lack of Cu-vacancies, i.e. a CGI > 1.0, was demonstrated to hinder the Na diffusion from the substrate, Cu-rich metal precursors were chosen as a starting point. In the following, the morphology and composition of the precursors is investigated and afterwards, the annealed absorbers are characterized.

Precursor characterization

Morphology and composition

The substrates used in this section differ slightly from the other substrates, in previous chapters, in the sense that the SiO_2 thickness is 1 µm. Additionally, the micro-dots are arranged in an hexagonal lattice and are accompanied by a $3\times3\,mm^2$ square hole in the SiO_2 to access the Mo back contact for electrical characterization, as shown in Figure 5.1a.

Looking at the morphology of the precursors, two extremes are observed. On the one hand, the precursor shows a flat and smooth surface with a white appearance, visible in Figure 5.1b. Figure 5.1c presents the corresponding height map, from which the following conclusions can be drawn: First, the smooth surface is confirmed as hardly any height fluctuation is perceived. Conversely, along the perimeter of the precursor, a narrow rim (1-2 µm width) is protruding higher (0.4-1 µm) than the inner region of the precursor. Finally, it stands out that, in this case, the metal precursor is slightly higher ($\sim$100 nm) than the SiO_2 layer, suggesting a precursor thickness of roughly 1 µm. On the other hand, in Figure 5.1d, the precursor has an uneven appearance instead and is populated by black structures, present both inside and outside of the micro-dot region. According to the height map, in Figure 5.1e, these structures can have heights larger than 2 µm. As previously, the underlying precursor itself has a flat morphology, except for the protruding rim along the perimeter.

Focusing first on the origin of the rim, cross-section SEM images were acquired before removing the resist. Figure 5.2a shows an SEM cross-section close-up at the periphery of a micro-dot directly after the sputtering of the Cu(In,Ga) metal precursor.

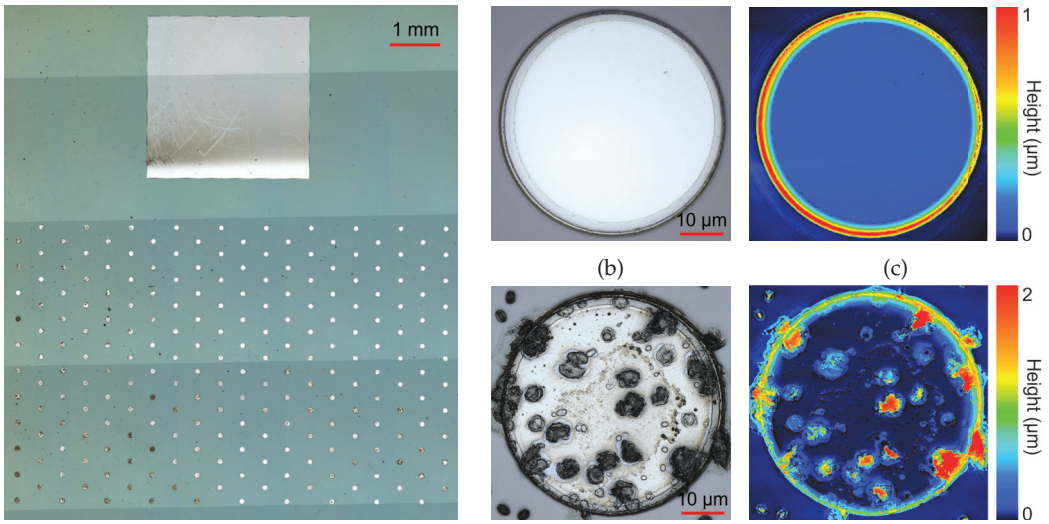

Figure 5.1: a) Top-view optical image of the array of micro-dots containing the Cu(In,Ga) precursor layer. The square at the top of the image is a hole in the SiO_2 matrix to access the Mo back contact. CLSM b) optical image and c) respective height map of a micro-dot containing the metal precursor without apparent contaminants. CLSM d) optical image and e) respective height map of a contaminated micro-dot precursor.

As expected, the topmost layer is the sputtered Cu(In,Ga), which covers the whole substrate. However, focusing at the periphery of the micro-dot (indicated by a double ended arrow in Figure 5.2a), a small fraction ($\sim$1.5 µm) of the SiO_2 layer is neither covered by the resist nor by the Cu(In,Ga). This suggests that the Cu(In,Ga) sputtering damaged and removed the resist. Since the width of the protruding rim is also roughly 1.5 µm, as observed with CLSM, its origin could be related to the abrasion of the resist during the sputtering step, leading to an accumulation of Cu(In,Ga) deposit at the periphery between the resist and the micro-dot. This hypothesis implies that the protruding rim is a blend of organic resist and Cu(In,Ga). Assuming this resist damage happens early on during the sputtering process, the incorporation of resist within the Cu(In,Ga) precursor is not limited to the surface, but might affect the whole micro-dot volume. In fact, damages to photolithography resists by magnetron sputtering processes have already been reported [161]. To verify the contamination hypothesis, EDX mapping of a filled micro-dot, after the removal of resist and similar to that in Figure 5.1b, was measured to have the spatial distribution of C content (signature element of the resist), in Figure 5.2b.

The C EDX mapping shows three regions that can be differentiated by their C content and correspond to the inner region of the micro-dot, the protruding rim and the surrounding SiO_2 layer. The latter acts as a reference for the eventual C deposition during the EDX measurement. According to the map, the rim indeed contains a higher content of C than the inner region of the micro-dot and both are clearly higher than the reference SiO_2 region. This is also demonstrated in Figure 5.2c, where the frequency distributions of C content in the three regions is plotted. The vertical dashed lines indicate the respective average C content in the respective regions and the error bar is the distribution's

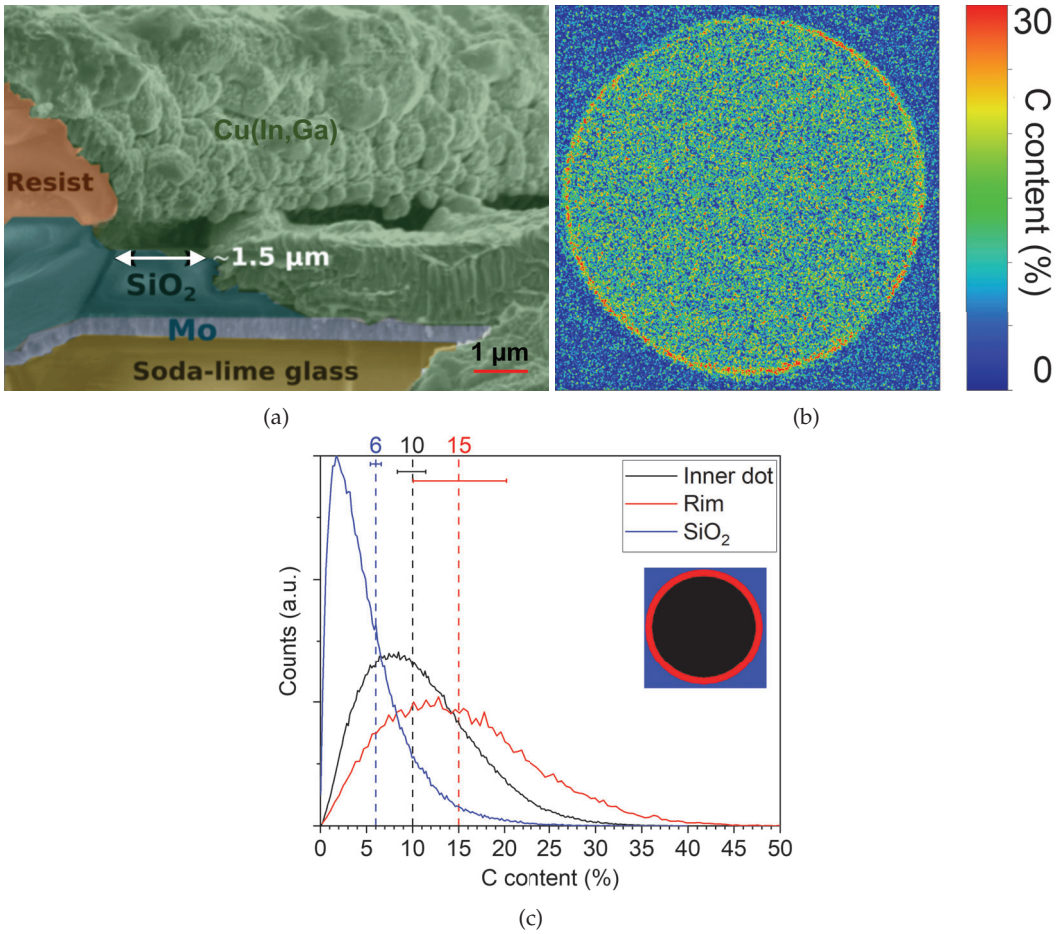

Figure 5.2: a) SEM cross-section image of a micro-dot before removing the organic resist (colors were added for easier distinction). White double arrow indicates region without resist nor Cu(In,Ga). The cross-section image was provided by Dr. Ana Pérez-Rodríguez and adapted here from [160]. b) Spatially resolved EDX map, measured at 10 kV, of a 50 µm diameter micro-precursor with distribution of C content. c) Frequency distributions of C content, extracted from Figure 5.2b, within the three regions schematized as an inset. Blue curve is related to the C content measured outside the micro-dot, black curve to the inner region of the micro-dot, i.e. the precursor, and the red curve related to the rim around the micro-dot.

standard deviation. Here again, the protruding rim shows the highest C content, as well as the broadest distribution, followed by the inner region of the micro-dot, with a lower C content and finally the SiO_2 region which has the lowest C content and sharpest distribution as expected. This observation corroborates with the hypothesis of resist contamination in the rim and within the precursor layer, despite its smooth morphology, suggesting an inherent contamination issue in the sputtering process. It is also speculated that the high density of micro-dots in this pattern, i.e. the reduced spacing between neighbour micro-dots, could also promote the abrasion of resist during the precursor's sputtering.

In terms of composition, the smooth metal precursors show a homogeneous composition within the array with a CGI ratio of 1.5 ± 0.1 and a GGI ratio of 0.46 ± 0.06. This is also verified for the micro-dots containing the observed black structures (see Figure 5.1d).

However, the C content is roughly three times higher in the flat regions, whereas the black structures themselves are made up of C, O and Na, as highlighted by the SEM images and EDX spectra in Figures 5.3a-c. Since the resist itself is organic, this also supports the hypothesis that the sputtering process causes an abrasion of the resist and creates a blend between the metal precursor and the resist within the whole volume of the micro-dot. However, the origin of the Na peak, visible in Figure 5.3c, could not be identified. It is worth mentioning that the dedicated cleaning procedure (ultrasound baths in acetone and deionized water) could not remove these black structures.

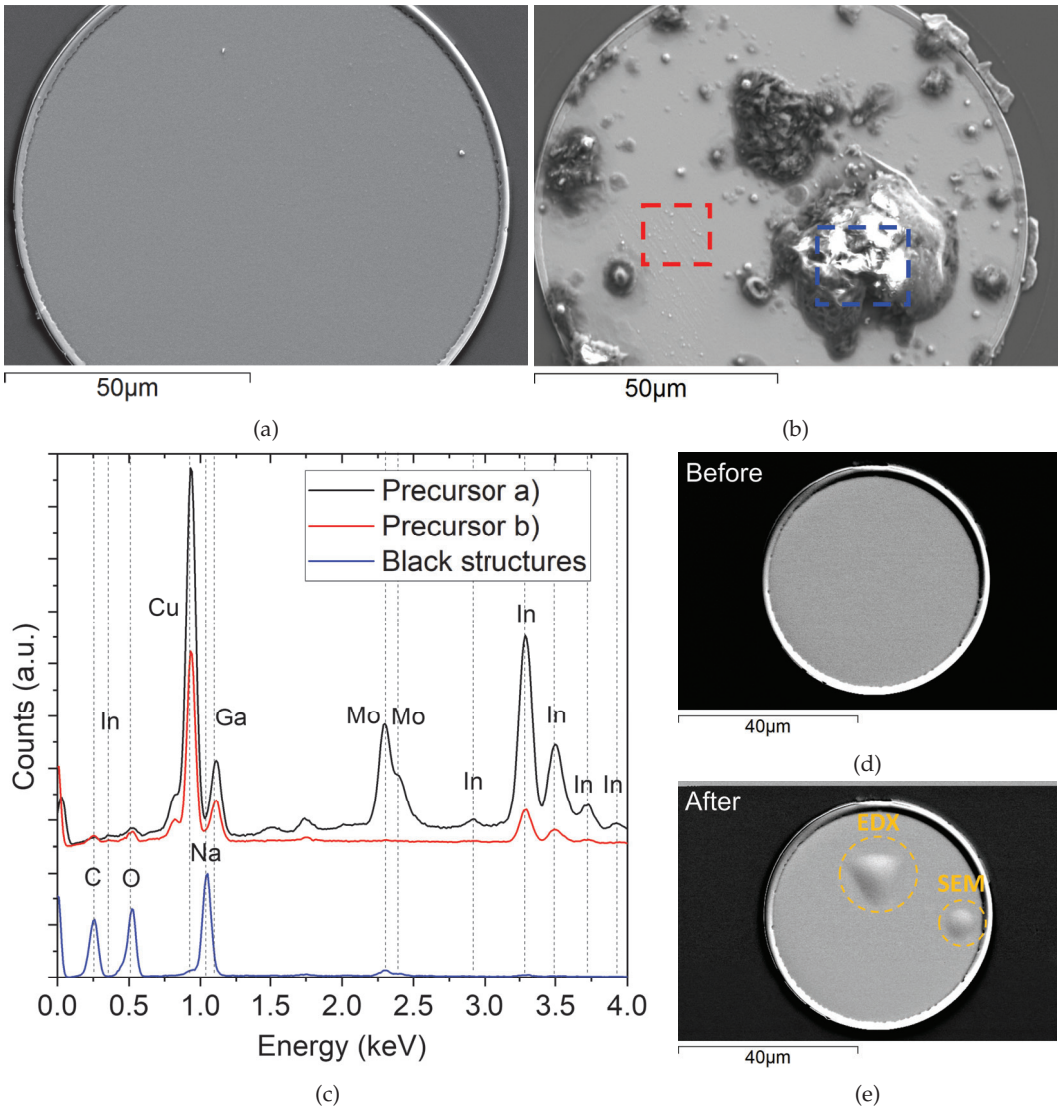

Figure 5.3: SEM image of a micro-dot precursor a) without visible contaminants and b) with contaminants. Dashed squares indicate the regions where EDX spectra, shown in c), were measured. c) EDX spectra measured at 10 kV from the corresponding locations in a) and b). The two spectra from the precursors (black and red) were shifted upwards. The bottom spectrum (blue) is related to the black structures. The relevant peaks were labelled with the corresponding elements. SEM images of a micro-dot precursor d) before and e) after EDX measurement and high focus with SEM electron beam. The respective locations are indicated with dashed circles.

As a side note, it was observed that the morphology of the precursor was irreversibly modified by the SEM/EDX electron beam after a spectrum measurement or when using very high magnification (> 40 kX). Figures 5.3d-e are SEM images of the same precursor micro-dot before and after an EDX measurement and a zoom-in to high magnification at the indicated locations, respectively. In both cases, the morphology of the precursor inflates locally and results in a bump with a height of a few hundreds of nanometers. This effect was not particularly studied, however it is hypothesized that the electron beam heats up the blend of metal precursor and organic resist, causing the latter to expand.

Attempt to remove contamination

In all cases, it is detrimental to have resist leftovers remaining within the metal precursor. A strategy to extract the contaminants from the precursor is to perform an annealing process to potentially vaporize the organics. In the synthesis process, an annealing routine in Se-containing atmosphere is anyway foreseen. Thus, two methods were tested, those are, (i) annealing the metal precursors directly in Se or (ii) perform an additional annealing step in an N_2 inert atmosphere before the annealing in Se. Both results, pertinent to the annealings in Se, are discussed in the following section.

The annealing in N_2 consists of heating the sample inside a sealed, and slightly under-pressure, vacuum chamber filled with N_2, to avoid oxidation of the precursors. The temperature of the annealing was 440 °C for 20 min. Figure 5.4 presents the morphology of two precursor micro-dots before (Figures 5.4a-d) and after (Figures 5.4e-h) the annealing routine to remove the contaminants. For the first micro-dot (Figure 5.4a), the morphology of the precursor looks flat, whereas in the second case (Figure 5.4c), some resist leftovers are already present both within the precursor and on the SiO_2 layer. The respective height maps are found next to the corresponding morphology image.

Addressing the first micro-dot, which looked unaffected by the resist abrasion, after the annealing routine its surface became rougher, marked by an apparently porous and granular morphology. This can be visible both in the SEM image and CLSM height map in Figures 5.4e and 5.4f. Note that the dome on the left side of the precursor was caused by an EDX measurement in between the first SEM image and the annealing routine. In fact, a fraction of the rim, at the periphery of the micro-dot, disappears after the annealing. This agrees with the EDX mapping discussed previously, which confirms the protruding rim to be a blend of Cu(In,Ga) and organic resist. Referring to the phase diagrams of CuGa and CuIn [162, 163], both have a liquid phase above 300 °C. Therefore, the annealing is partially melting the precursor. At 440 °C, the organic resist is expected to vaporize and degas out of the partially liquid Cu(In,Ga) phase, leading to the formation of the porous morphology upon cooling down to room temperature. A similar conclusion can be drawn from the second precursor as pinholes are clearly formed after the annealing. Furthermore, the resist leftovers that were on the SiO_2 layer, before the annealing (see Figure 5.4c), have been vaporized and are barely visible in Figure 5.4g. Regarding the resist on the precursor itself, the height maps before (Figure 5.4d) and after (Figure 5.4h)

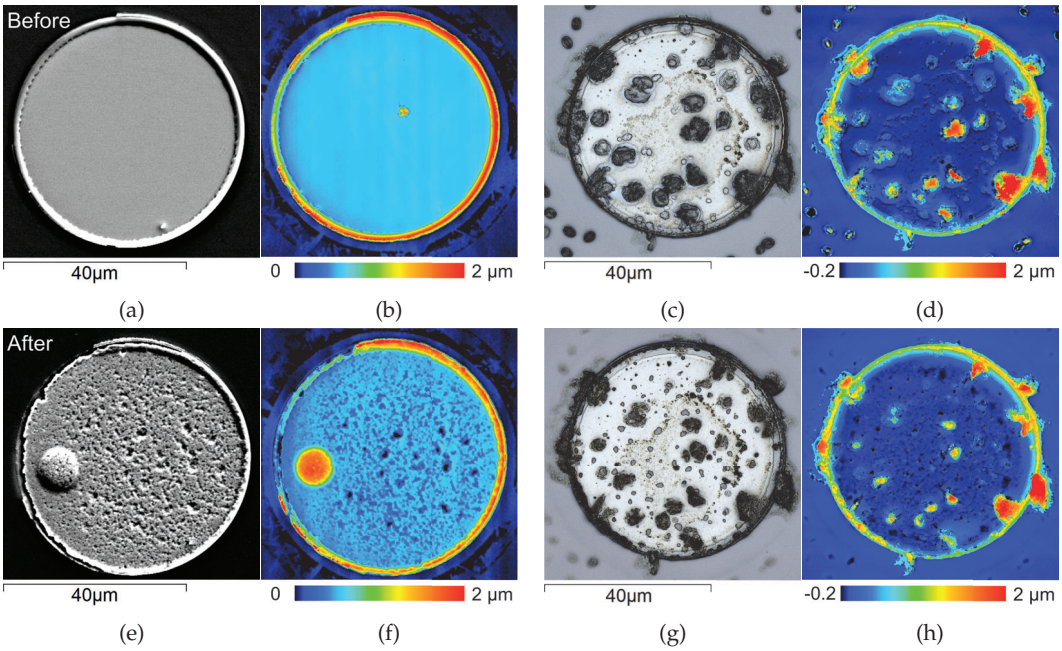

Figure 5.4: SEM and CLSM images of the morphology of two micro-dot precursors (a-d, top row) before and (e-h, bottom row) after the N_2 annealing routine at 440 °C. The CLSM height maps of the respective images are also presented.

the annealing demonstrate that their volume was reduced, meaning that at the very least they were partially vaporized. Thus, the annealing routine in N_2 is indeed effective in at least partly removing the resist leftovers that withstood the cleaning procedure.

Absorber formation

Having investigated how the contaminated metal precursors change after an annealing in inert N_2 atmosphere, the focus goes now to the annealing in Se-containing atmosphere, i.e. selenization, which converts the precursors into CIGSe absorbers. First, the selenization of the pristine precursors is discussed followed by the precursors already annealed in N_2.

The selenization process was performed in a tube oven, as described in chapter 2. The N_2 background pressure was 350 mbar, the amount of Se powder in the graphite box was 150 mg and the annealing time was 20 min for the selenization of pristine precursors, whereas for the already annealed precursors the annealing time was 10 min. For comparison, one N_2-annealed precursor was selenized also for 20 min and the only noticed impact, due to the longer annealing, was the extended damage on the SiO_2 layer. Different annealing temperatures were tested, ranging from 350 °C to 470 °C.

Selenization of pristine precursors

Building up on the results of the previous section, the selenization of the pristine precursors implies that both the vaporization of the contaminants and the formation of the CIGSe absorber happen in parallel. In fact, it was observed previously that the inert

annealing at 440 °C was not enough to completely remove the organics, implying that both processes do happen simultaneously. This is as problematic as it sounds, given that just to prevent the SiO_2 layer from deforming and cracking, the annealing temperature had to be reduced to below 450 °C. This is clearly visible macroscopically, but also at the microscopic level with the CLSM optical image and height map, in Figures 5.5a and b, where the morphology of an absorber annealed at 470 °C is depicted. Regarding the absorber itself, it puts forward a granular morphology that resembles that of CIGSe, as well as some $Cu_{2-x}Se$ platelets, which is expected given the precursor's Cu-rich composition. However, the absorber also seems to be cracked locally and heavily deformed, given its excessive height compared to the SiO_2 layer. The expected thickness of the CIGSe absorber is roughly double that of its precursor, due to the expansion of incorporating Se. In this case, the anticipated thickness of the CIGSe absorber is about 2 µm, that is almost ten-fold less compared to the measured heights.

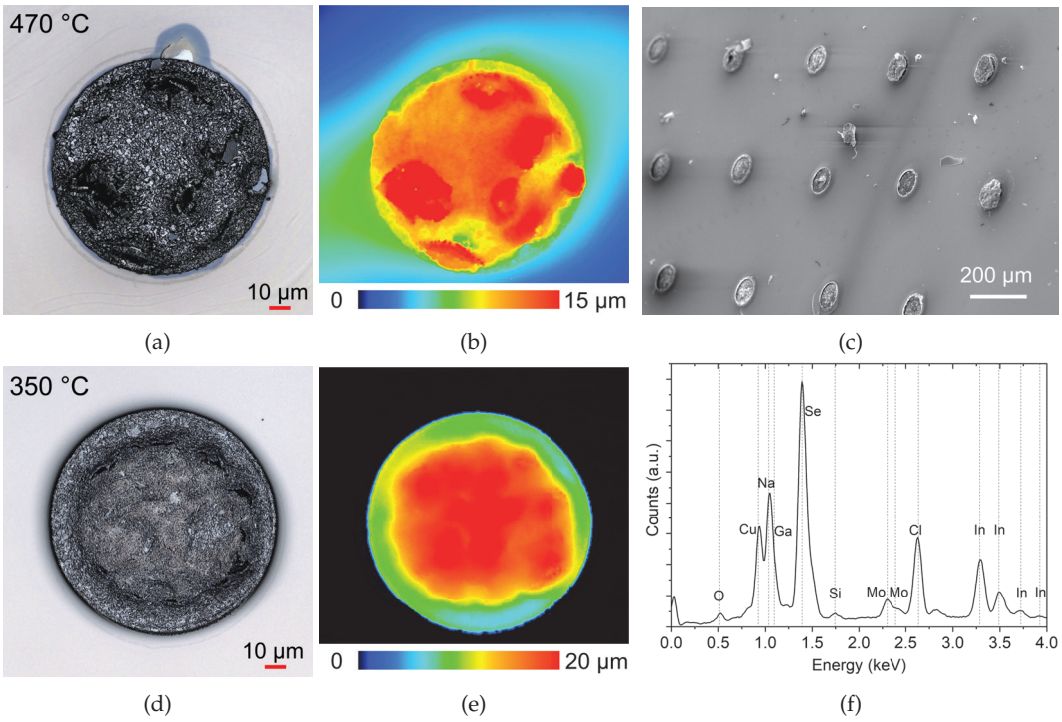

Figure 5.5: CLSM a) optical image and corresponding b) height map of a deformed CIGSe absorber (annealed at 470 °C) and SiO_2 matrix. c) SEM image of a fraction of the micro-dots array, measured with the sample at a 45°angle, to show that the absorbers are barely attached to the substrate. CLSM d) optical image and corresponding e) height map of a deformed CIGSe absorber (annealed at 350 °C). f) EDX spectrum acquired from a deformed CIGSe absorber, measured at 20 kV.

To have a different perspective on the absorber's morphology, an SEM image was captured with the sample inclined at about 45°, as shown in Figure 5.5c. The SEM image shows a fraction of the array of micro-dots, where some have the CIGSe layer barely attached to the underlying substrate, while others only have fractions of the layer and are mostly empty. This demonstrates that most of the absorber's measured volume is hollow,

which drastically compromises the contact between the CIGSe absorber and the Mo back contact layer. In fact, the low adhesion between the two layers also explains why some of the micro-dots were found mostly empty after the annealing. Lowering the annealing temperature to 350 °C did ensure the integrity of the SiO_2 layer, however the CIGSe absorber still shows an excessive deformation, as shown in Figures 5.5d and 5.5e. Obviously, these absorbers cannot be used for solar cells, given the poor adhesion of the CIGSe and the Mo layers. An EDX sprectrum was acquired from a deformed absorber layer and is plotted in Figure 5.5f. Interestingly, a considerable amount of Na (Na/Cu=1.3), and Cl, is observed in the absorber, in addition to the expected elements. Note that this ratio is excessively high compared to standard CIGSe synthesis (Na/Cu < 0.04) [141]. This could either be justified by the presence of Na in the resist contaminants or that the Cu-rich composition alone is not enough to mitigate the Na diffusion from the soda lime glass, at such Se partial pressures. In fact, extrapolating from the observations on the Cu-poor sputtered samples discussed in section 4.3, if the Se partial pressure is too high, the Na diffusion is still consequent, despite the partial blocking due to the suppression of Cu-vacancies. All in all, these results demonstrate that forming the CIGSe phase, having an excess of Na and removing the contaminants simultaneously is not appropriate to obtain a compact CIGSe morphology.

Selenization of N_2-annealed precursors

Given that direct selenization is not viable, in the following the selenization of the precursors, already annealed in N_2, is presented. The introduction of the additional annealing in N_2 improved the selenization process, in the sense that previously problematic annealing temperatures (450 °C), now hardly resulted in cracking of the SiO_2 layer and more importantly the morphology of most (∼60 %) of the arrays of absorbers were compact and within expected thicknesses, as shown in Figures 5.6a and b. Since these absorbers also show quite some Na (Na/Cu=0.4), possible reasons for not reaching 100 % success, may be different Na contents in the soda lime glasses or different amounts of resist contaminants incorporated with the metal precursors, which was also proved to contain Na.

The morphology of the compact absorbers is characterized by a high number of $Cu_{2-x}Se$ platelets on a CIGSe granular layer. To understand if the $Cu_{2-x}Se$ platelets were also present in the bulk of the absorber, a cross-section SEM image was acquired, as shown in Figure 5.6c. Clearly, the metallic-like $Cu_{2-x}Se$ platelets are also present within the absorber's bulk and some are even longer than the layer's thickness, which would make a detrimental shunt path between the top and bottom contact layers, in the case of a solar cell architecture.

An interesting question is how does the CIGSe expand due to the selenization. In fact, it was observed that some absorbers had a larger diameter than their respective precursor, while other absorbers retained a similar diameter. This is visible in Figures 5.7a

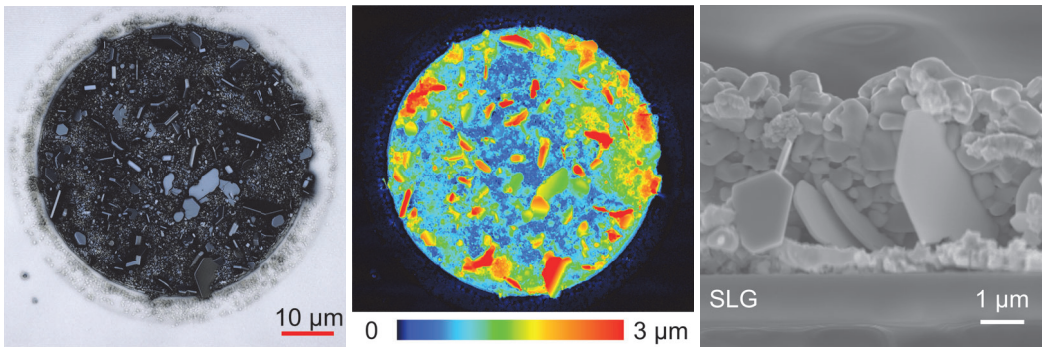

Figure 5.6: CLSM a) optical image and b) respective height map of a compact CIGSe absorber. c) Cross-section SEM of a Cu-rich CIGSe absorber. The $Cu_{2-x}Se$ platelets are visible across the whole absorber's thickness.

and b, where both situations are shown. Additionally, Figures 5.7c and d depict the representative morphology of the precursors to the aforementioned absorbers. In all cases, the measured diameter is highlighted and a schematic cross-section of the hypothesized layer configuration is shown next to the respective height map.

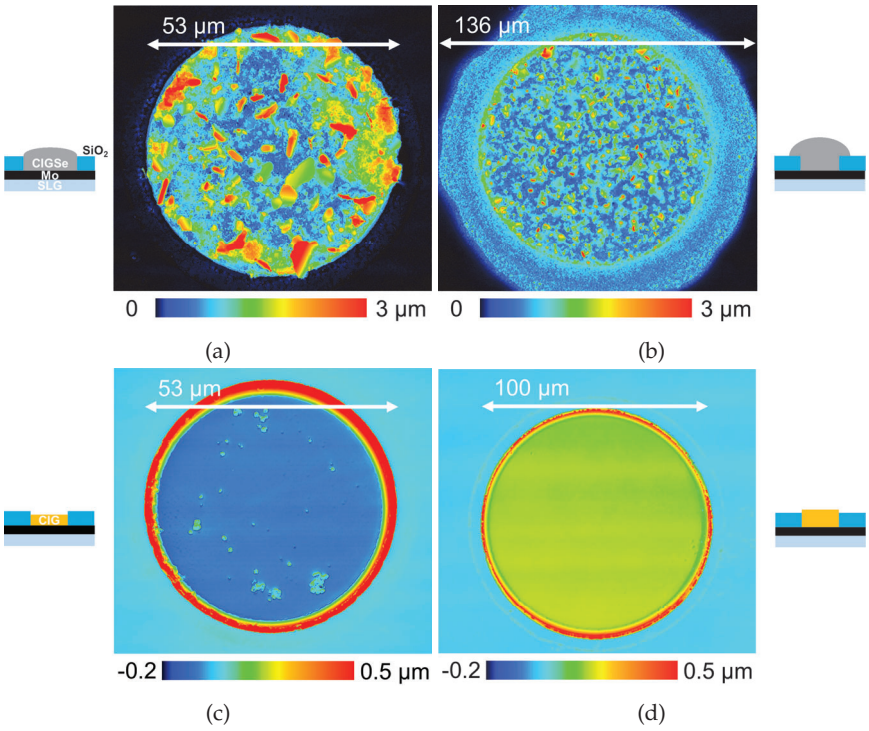

Figure 5.7: CLSM height map of: a) a compact CIGSe absorber. In this case, no expansion beyond the micro-dot's original region is observed. b) a CIGSe absorber that expanded onto the SiO_2 matrix during the annealing in Se. c) a sister micro-dot precursor to the absorber shown in a). Note that the precursor is recessed comparatively to the SiO_2 matrix. d) a sister micro-dot precursor to the absorber shown in b). Note that the precursor is protruding comparatively to the 1 µm thick SiO_2 matrix. A schematic cross-section of the hypothesized layer configuration is depicted next to the respective height map.

The fact that some absorbers have a larger diameter compared to their respective precursor suggests a three-dimensional expansion of the material's morphology during selenization. Although an expansion perpendicular to the substrate (z-direction) was expected, the reason for a growth in the xy-plane, in some cases, is not clear. Raman analysis (spectra not shown), highlight the presence of the chalcopyrite A_1 mode also beyond the micro-dot's original diameter, which confirms the CIGSe absorber is expanding in both directions. The extent of the absorber's lateral expansion seems to be correlated with the height of the respective precursor compared to the SiO_2 layer. More precisely, a precursor with a height lower than the SiO_2 layer, as in Figure 5.7c, resulted in a minimal lateral expansion after selenization, as Figure 5.7a shows. Conversely, a protruding precursor, as in Figure 5.7d, led to a consequent lateral expansion after selenization, as depicted in Figure 5.7b. Assuming that the SiO_2 matrix is not deformed, the observed expansion is likely related to the liquid phase, that the precursor forms at higher temperature, which flows beyond the original micro-dot's diameter.

To discard a deformation of the SiO_2 matrix, EDX was measured from the SiO_2 layer towards the center of the absorber, spatially resolving the Si signal, as shown in Figure 5.8a.

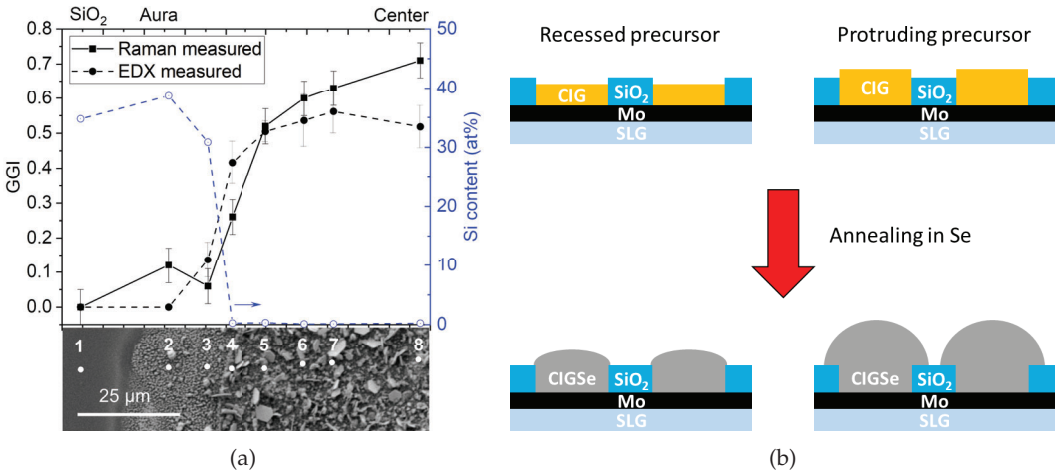

Figure 5.8: a) GGI ratio and Si content measured from the SiO_2 layer towards the center of the CIGSe micro-absorber. b) Schematic cross-section of the sample geometry before and after annealing in Se, illustrating the influence of the precursor's height, relative to the SiO_2 matrix, on the final absorber's morphology.

The Si content stays constant outside the original diameter of the micro-dot, i.e. micro-dot's aura, and quickly decreases to zero inside it. This confirms the CIGSe absorber grows in a muffin-top fashion, as illustrated in Figure 5.8b, and discards the deformation of the SiO_2 layer by the lateral expansion of the CIGSe.

Interestingly, the distribution of Ga in the absorber is different inside the micro-dot and within the aura, as demonstrated in Figure 5.8a through the GGI. The spatially resolved EDX and Raman analysis (GGI deduced from A_1 mode position) both corroborate that no or very low Ga is found in the aura region, whereas a high Ga content is found

inside the micro-dot's original diameter. This suggests that the chalcopyrite phase that lead to the formation of the aura, outside of the micro-dot, is $CuInSe_2$. Mainz et al. have shown that during selenization, In tends to migrate to the surface, causing Ga to segregate at the back of the absorber [164]. Here, it is speculated that the lateral diffusion of In hinders the diffusion of Ga towards the aura. Thus, one function of the SiO_2 layer is to retain the CIGSe film's shape and consequently, composition homogeneity. Since the targeted absorber thickness is in the 2 µm range, a similar SiO_2 thickness is preferable to guide the CIGSe absorber.

Despite clearly improving the outcome of the selenization, with a 60 % success rate, the addition of the inert annealing by itself does not guarantee a controlled absorber morphology and adhesion to the Mo layer. As also suggested in section 4.3 of chapter 4, the high Se partial pressure, during the selenization step, may increase the Na diffusion from the soda lime glass, which compromises the adhesion between the CIGSe and the Mo layer. This shows that controlling the Se partial pressure during the annealing is crucial to obtain compact CIGSe absorbers.

Device characterization

This section covers the characterization of absorbers that were converted into micro solar cells. Given the consequent Cu-rich composition of the absorbers, a KCN (10 wt% for 5 min) treatment [165], followed by the chemical bath deposition of a 50 nm CdS buffer layer are applied to the array. The former has the aim of removing the $Cu_{2-x}Se$ platelets from the absorbers and the CdS buffer layer to improve the CIGSe interface and form the pn-junction. To convert the absorbers into solar cells, the transparent conductive oxide layers (i-ZnO/ZnO:Al) are deposited by sputtering.

To assess the quality of the solar cells in the array, EQE and JV measurements were performed in Figure 5.9. From semi-quantitative EQE spectra on individual micro solar cells, as exemplified in Figure 5.9a, the average bandgap is estimated to $E_{gap}^{EQE} = 1.3 \pm 0.1$ eV. This value agrees well with the bandgap $E_{\text{gap}} = 1.3 \pm 0.2$ eV calculated empirically from the GGI of the metal precursors (GGI=0.46) [166]. The general shape of the EQE suggests a poor carrier collection in the infrared range above the bandgap. Additionally, the drop in the UV-region is associated to parasitic absorption by the CdS buffer layer.

The number of electrically active solar cells was estimated by probing each one with the EQE beam (at 532 nm) and by measuring the resulting current. Out of 198 solar cells, 182 were electrically active. Finally, JV measurements on groups of micro solar cells was performed. The preference of groups over individual solar cells was to facilitate the mechanical scribing of the window layers, meant to electrically isolate each group of solar cells, and to minimize the risk of shunt paths. It is noted that when connected in parallel, the current of each solar cell, in the group, contributes to the total measured current, while the open-circuit voltage of the group is given by the lowest individual open-circuit voltage. Figure 5.9b shows the JV characteristics of a pair of isolated micro solar

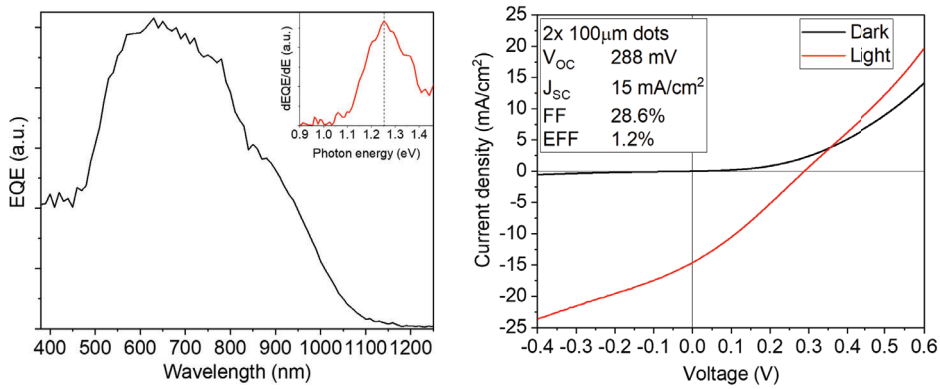

(a) (b)

Figure 5.9: a) Semi-quantitative EQE from one micro solar cell. The energy derivative of the EQE is shown as inset to determine the bandgap. The EQE is semi-quantitative because the laser beam size was larger than the micro solar cell's active area. b) JV characteristics in the dark and under illumination of a group of two micro solar cells connected in parallel. Key parameters are summarized as inset.

cells, connected in parallel. The devices show a diode-like behavior with an efficiency of $(1.2 \pm 0.3)\,\%$ under 1 Sun. A low shunt resistance ($60\,\Omega\text{cm}^2$) and a relatively high series resistance ($3.4\,\Omega\text{cm}^2$) were measured, as well as a voltage-dependent current collection. These are possibly related to shunt paths resulting from the large $Cu_{2-x}Se$ platelets within the absorbers and potential pinholes and defects caused by the platelets during the synthesis process and the KCN treatment. The short-circuit current density Jsc is found to be 15 ± 2 mA/cm^2 which is in line with the EQE showing very poor collection in the near-infrared region. Larger groups of micro solar cells also showed a diode behavior, however the shunt resistance was even lower in these cases. The active area used for the JV measurements was calculated by taking the number of individual micro solar cells in a group and multiplying by the area of a single disc of 100 µm diameter.

To conclude the synthesis of Cu-rich micro solar cells, it was demonstrated that this material-efficient sputtering and annealing route can lead to working micro solar cells, however multiple issues were encountered which limited the achieved PCEs. First, the sputtering process introduces resist contaminants in the precursors, which imposed the introduction of an extra synthesis step to extract the resist and obtain compact CIGSe absorbers. It is speculated that the high density of micro-dots in this pattern, i.e. the reduced spacing between neighbour micro-dots, could promote the abrasion of resist during the precursor's sputtering. Thus, in the following, patterns with a lower density of micro-dots are used. Increasing the space between micro-dots also simplifies the process of electrically isolating individual micro solar cells. Secondly, a significant amount of Na was found in all selenized absorbers, which could originate either from the contaminants or by diffusion from the soda lime glass. Since no Na was detected in the precursors without visible contaminants, the diffusion from the soda lime glass, also observed in chapter 4, seems more likely. In any case, this could explain why not all synthesized absorbers were compact. Finally, it was observed that the thickness of the SiO_2 is important,

as it helps holding the precursor's shape during the annealing step. Indeed, a SiO_2 thickness lower than that of the Cu(In,Ga) precursor will lead to a muffin-top morphology after annealing in Se. This was observed to cause a lateral composition inhomogeneity, which is detrimental for the solar cell's performance. For this reason, a thickness of 2 µm is used in the following. Despite these issues, multiple groups of working micro solar cells were achieved, with the highest PCE being 1.2 % for a group of two devices.

5.1.2 Cu-poor solar cells

Despite having achieved working micro solar cells with Cu-rich CIGSe absorbers, it is of particular interest to investigate Cu-poor CIGSe absorbers. This is the case as the Cu-rich absorbers are known to be limited by interface recombination and by tunnelling enhanced recombination, due to their high doping level, which reduces the resulting solar cell's V_{OC} and J_{SC}, respectively [44].

In chapter 4, an important finding about Cu-poor CIGSe absorbers is that the patterned SiO_2 layer causes a detrimental enhanced diffusion of Na, from the soda lime glass, through the micro-dots. This issue was mitigated by the introduction of a Na blocking layer, like Al_2O_3 or SiO_xN_y. However, completely depriving the CIGSe absorber of Na during synthesis led to the peeling of the material from the substrate. Therefore, the use of substrates with a Na blocking layer is complemented by performing the annealing step in a Na-containing graphite box. In this way, the peeling of the film is expected to be avoided [141].

For this section, a 100 nm Al_2O_3 layer was used as Na barrier and the SiO_2 pattern containing arrays of micro-dots with varying diameter is chosen. This allows to also investigate if the size of the micro-dots is relevant during the synthesis process.

Precursor characterization

In the following, the morphology of the Cu-poor sputtered precursors is investigated. Figures 5.10a and b show the morphology and respective height map of a filled micro-dot. As can be noticed, the morphology of the precursor is identical to that in section 4.3, where the metal precursor had been deposited both inside the micro-dots and on the SiO_2 layer. In short, the morphology consists of a relatively thin Cu-rich compact underlying layer and an In-rich rough top layer made up of irregularly shaped agglomerates. Further EDX analysis show an average compositional ratio CGI of 0.72 and a GGI of 0.21. Although the CGI ratio is rather low compared to stoichiometry, reports have demonstrated relatively high PCEs (∼10 %) can be obtained for CIGSe solar cells from precursors with a similar composition as here [167, 168]. Thus, these precursors are in line with the objectives of this study.

Given the resist contamination issues observed in the case of sputtered Cu-rich, an annealing in N_2 inert atmosphere at 250 °C for 20 min is also performed to cross-check the Cu-poor case. The resulting morphology and height map are depicted in Figure 5.10c and d.

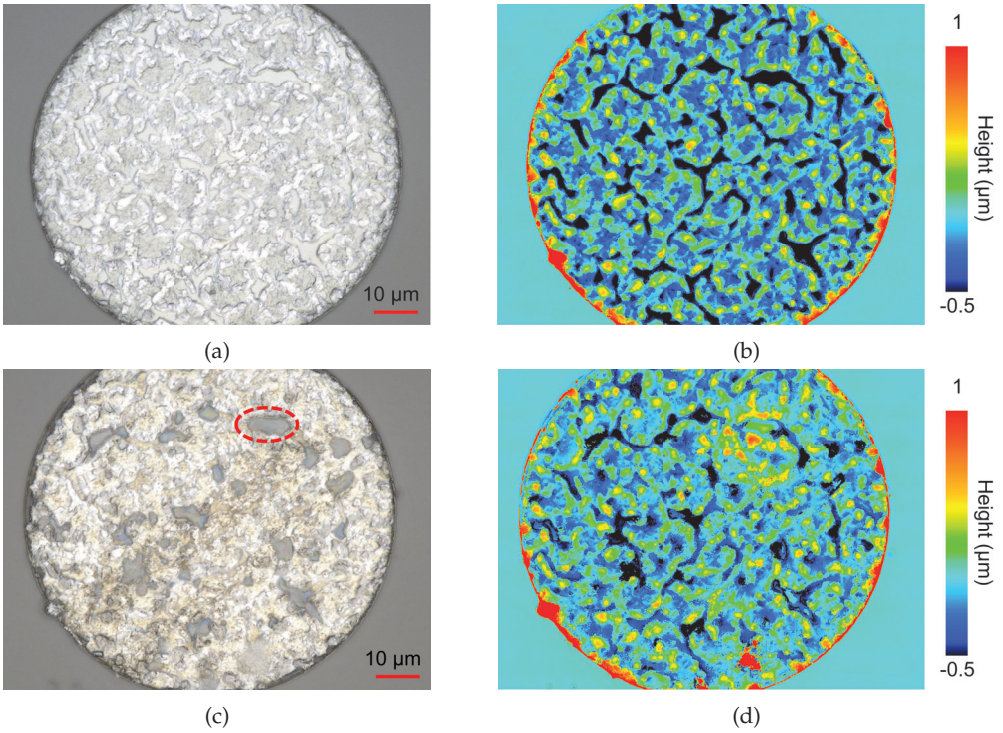

Figure 5.10: CLSM optical image and respective height map of the same micro-dot precursor (a and b) before and (c and d) after an inert annealing in N_2. Red dashed ellipse highlights one of the regions where the Mo layer was exposed after the N_2-annealing.

After annealing, both the appearance and the morphology of the metal precursors are rather different. In fact, the film seems to coalesce and form some holes in between the In-rich agglomerates, where the layer was already thinner. In these regions, the underlying Mo layer is even exposed after the N_2-annealing, as corroborated by EDX analysis (spectrum not shown). Anticipating the consequences for the annealing in Se atmosphere, the formation of these holes reveals an easy access for Se to form the conductive $MoSe_2$ layer, which is detrimental when excessively thick [169]. Additionally to the holes, the precursor layer changed to a yellowish appearance, which suggests that some resist contaminants were still present. Although, no large remnants of resist were found as was the case for the Cu-rich sputtered sample, implying decreasing the density of micro-dots was beneficial. However, the Cu-poor sample (discussed in section 4.3) sputtered without resist, did not show any modification after being annealed in the same way as the present precursors. These observations corroborate with the hypothesis of resist damage during sputtering and demonstrate that increasing the spacing separating micro-dots was not enough to avoid the contamination of the precursors by the resist.

Absorber formation

Impact of precursor's N_2-annealing

To assess the impact of the annealing in N_2, the pristine and N_2-annealed precursors are selenized in identical conditions. In this case, the annealing temperature was 450 °C for 10 min with 100 mbar of N_2 background pressure and 40 mg of Se powder. The morphology of the resulting CIGSe absorbers are discussed in the following, starting with the pristine precursor. Figure 5.11 regroups CLSM optical and height images of the same micro-dot before and after the annealing in Se.

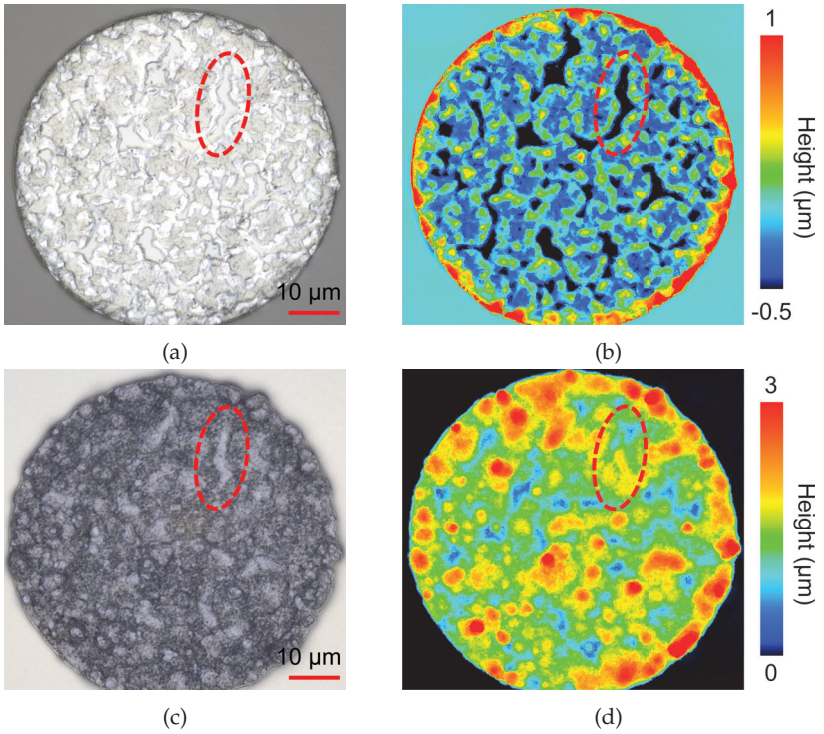

Figure 5.11: CLSM optical image and respective height map of: a) and b) micro-dot Cu(In,Ga) precursor. c) and d) CIGSe absorber after annealing in Se. Red dashed ellipses highlight the same region, in the precursor and in the absorber, where the precursor shows a valley in-between In agglomerates and, after annealing, the same region is identifiable in the absorber, however its morphology is substantially different.

Interestingly, when comparing the optical images of the precursor (Figure 5.11a) and absorber (Figure 5.11c), it appears that some regions, in particular the valleys in between In agglomerates, formed grains with a similar shape after the annealing in Se. However, this correlation between shapes is not visible when comparing the height maps (in Figures 5.11b and d). Nevertheless, the height maps do show a thinner absorber in some of the regions where the precursor was also thin, which suggests that the lateral diffusion of elements during the annealing in Se is rather consequent (estimated to a few micrometers) in the xy plane. Zooming in on a sister absorber, SEM imaging in Figure 5.12a unveils that the absorber layer has some micrometer-sized holes that, according to EDX spectra in Figure 5.12b and Raman in Figure 5.12c, expose the Mo/$MoSe_2$ back contact.

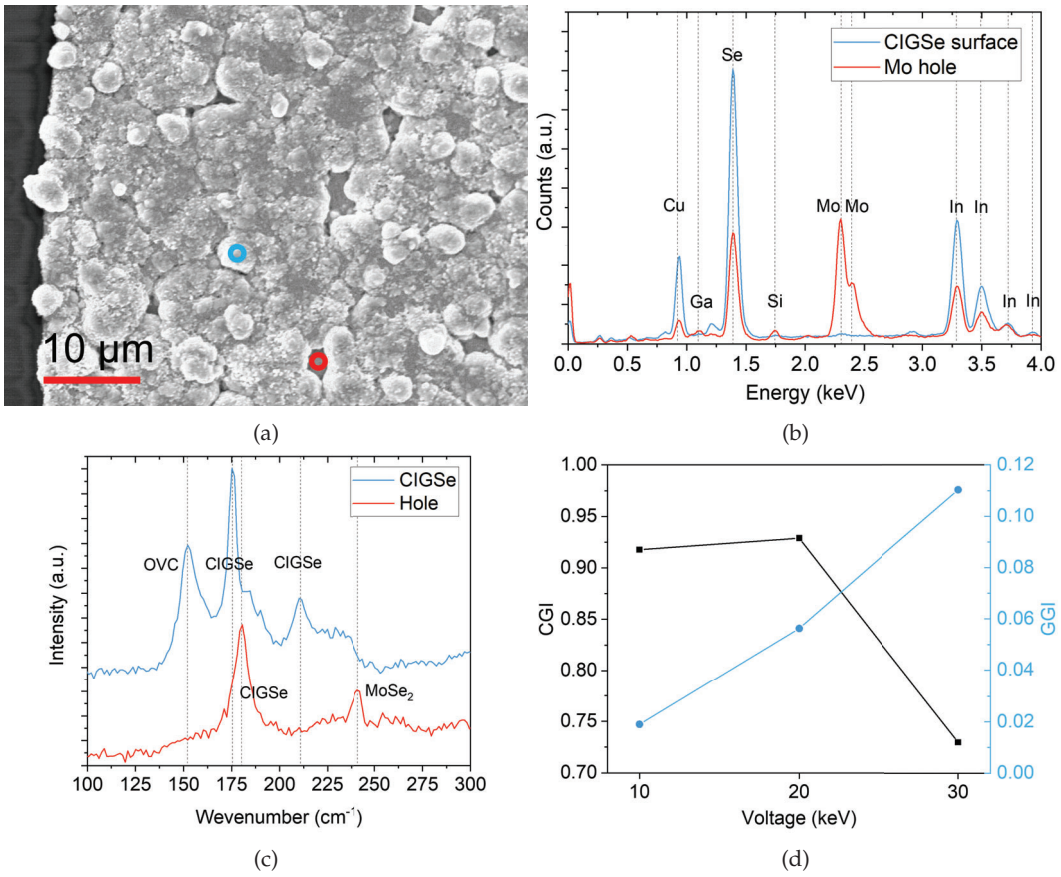

Figure 5.12: a) SEM close-up image on the edge of a micro-dot containing a CIGSe absorber. At this magnification, it is possible to identify microscopic holes in the absorber layer. Red and blue circles indicate the locations where EDX spectra in b) were acquired. b) EDX spectra measured at 20 kV from the locations drawn in a). c) Raman spectra measured from the locations indicated in a). A 532 nm excitation laser was used for surface-sensitivity, as it probes a depth of less than 100 nm [170]. d) Compositional ratios CGI and GGI, calculated from EDX spectra, as a function of the acceleration voltage.

Additionally, the Raman spectrum from the hole, also detects a Ga-rich CIGSe phase at 180 cm^{-1}, which would suggest a GGI of roughly 0.60. At the surface of the CIGSe micro-absorber, Raman detects a Ga-poor (GGI=0.1) CIGSe phase through the A_1 mode wavenumber position at 175 cm^{-1}. The second peak associated with the CIGSe, at 212 cm^{-1}, corresponds to the E/B modes [171]. Furthermore, an ordered-vacancy compound (OVC) phase is also detected, at 152 cm^{-1}, at the surface [172], which was to be expected given the low CGI of the metal precursors (CGI=0.72). To confirm the elemental depth distribution of the CIGSe phase, Figure 5.12d presents the elemental ratios CGI and GGI extracted from EDX spectra acquired at three acceleration voltages (10 kV, 20 kV and 30 kV). Starting with the lowest voltage, i.e., the most surface sensitive measurement, the average measured CGI was 0.92, however locally CGI values as low as 0.67 were measured, which suggests that only a few regions contain the OVC phase, as suggested by Raman. The lowest GGI value was indeed measured at the surface, however its absolute value (0.02) is lower than suggested by Raman. Nevertheless, at 20 kV, the GGI increases whereas the

CGI remains the same. Finally, at the back, or at 30 kV, EDX confirms the highest value for GGI (0.11). Note that despite the absolute GGI values being different, between Raman and EDX, the relative ratio between GGI at the surface and at the back is very similar. Studies on sequential selenization processes show that In diffuses to the front surface, due to the lower surface free energy of formation of $CuInSe_2$ compared to CIGSe [173, 174]. This pushes the Ga-containing phase towards the Mo interface, which corroborates with the above observations. The accumulation of Ga at the back is in fact beneficial, as it induces a Ga-rich phase, i.e. with a higher bandgap, which in turn reduces carrier recombination at the back contact, improving V_{OC} [175]. Interestingly, the micro-absorber shows a depletion of Cu at the back, as the CGI drops to 0.73. Together with Raman, these results suggest that the OVC phase is found either at the front and at the back or throughout the depth of the absorber. It is also worth noting that no Na peak is measured with EDX, which confirms the good behavior of the implemented Na barrier.

Moving to the CIGSe absorber that corresponds to the precursor annealed in N_2, Figure 5.13 presents CLSM optical and height images before and after the annealing in Se.

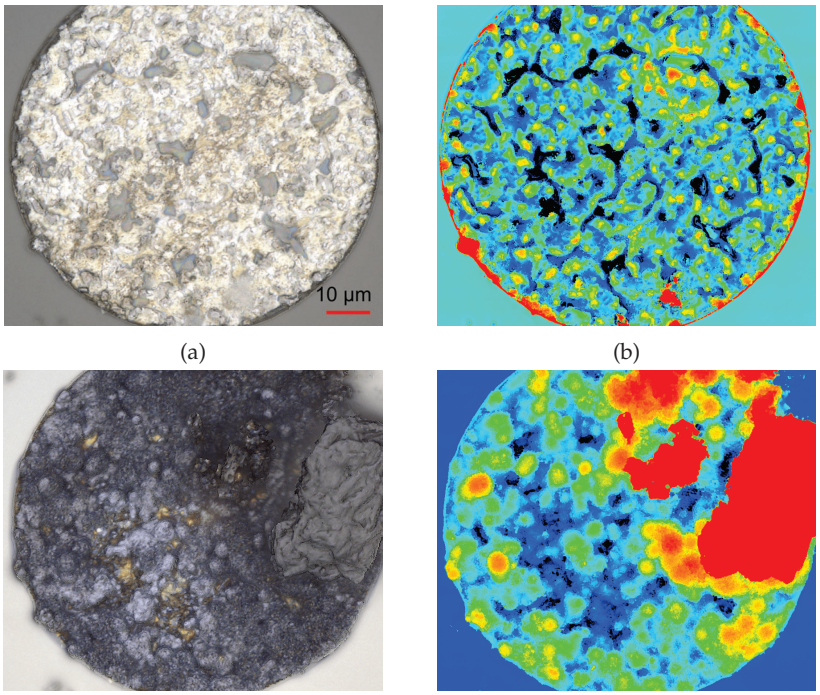

Figure 5.13: CLSM optical image and respective height map of: a) and b) micro-dot Cu(In,Ga) precursor annealed in N_2. c) and d) CIGSe absorber after annealing in Se.

The respective optical images, in Figures 5.13a and c, show that in the regions where the precursor had the Mo exposed, an orange phase seems to form, contrasting with the dark grey CIGSe phase. The orange phases will be discussed later in this section. Note that on the right side of the layer, a lump of Se solidified on the CIGSe layer covering part of the absorber morphology. Nevertheless, comparing the height maps, in Figures 5.13b and d, the holes in the precursor resulted in a thinner absorber in these particular regions,

which makes it prone to be more affected by interface recombination and ultimately result in a worse device performance [56]. Thus, the annealing in N_2 is not beneficial in this case and will therefore not be further investigated.

Influence of Se partial pressure on phase formation

In the following, different annealing conditions are investigated to optimize the morphology and the optoelectronic of the resulting CIGSe micro-absorbers. Literature has shown that a controlled supply of Se is required to optimize the morphological and optoelectronic properties of the resulting CIGSe absorber [55, 176]. On the one hand, an insufficient supply of Se compromises the chalcopyrite phase purity [177]. On the other hand, an excessive supply of Se implies that more Se will reach the Mo interface and form an overly thick $MoSe_2$ resistive layer [178]. Thus, it is of great interest to regulate the influx of Se that reaches the precursors. This is achieved by controlling the Se partial pressure in the system. The graphite box in a tube oven configuration being a common setup [179, 180], for the annealing in Se step, J. J. Scragg originally modelled the partial pressure of Se based on gas pressure equilibrium principle [181]. In short, the model starts with the graphite box and the respective lid inside a closed system. The background pressure, at room temperature, $P_{N,RT}$ is determined by the amount of N_2 introduced in the system before the annealing. At the annealing temperature T_{Anneal}, the Se powder, inside the graphite box, has partially evaporated leading to a Se partial pressure $P_{Se,box}$. This Se partial pressure lifts the lid and a fraction F of the Se gas phase escapes the graphite box until an equilibrium pressure, inside the graphite box and outside, is reached. Han et al. improved the model by additionally considering the pressure from the weight of the lid P_{lid} and the fraction of Se vapor C that condensates at the chamber's cold outer walls [55]. Note that C ranges from 0 to 1 and depends on the specific system configuration. Therewith, the equilibrium partial pressure of Se $P_{Se,eqm}$ inside the graphite box is given by:

$$\frac{P_{Se,eqm}}{P_{Se,box}} = 1 - F = 1 - \frac{P_{Se,box} + C \cdot P_{N,T_{anneal}} - P_{lid}}{(P_{N,T_{anneal}} + P_{Se,box}) \cdot (1 + \frac{V_{box}}{V_{chamber}}(1 - C))} \tag{5.1}$$

With $P_{N,T_{anneal}}$ being the N_2 partial pressure at T_{anneal} and is given by $P_{N,T_{anneal}} = P_{N,RT} \cdot \frac{T_{Anneal}}{T_{RT}}$. As specified above, P_{lid} is the pressure exerted by the lid's weight m with a surface A: $P_{lid} = \frac{mg}{A}$, with g being the gravitational acceleration constant. V_{box} and $V_{chamber}$ are the volumes inside of the graphite box and the chamber respectively. Finally, the partial pressure of Se inside the graphite box $P_{Se,box}$ is calculated with the ideal gas law assuming the Se vapor phase is composed of Se_2 molecules only.

Traditionally, CIGSe is known to demonstrate better device properties when annealed at higher temperatures, usually around 550 °C [182]. However, due to the introduction of the Al_2O_3 diffusion barrier to the stack, it was required to test for the thermal stability of the new stack. Indeed, it was found that the SiO_2 layer is severely cracked at 550 °C, however at 525 °C the cracking seems to be minimal. At these temperatures,

the effect of $P_{Se,eqm}$ on the morphology of micro-absorbers, with different diameters, is clearly visible. In fact, for both temperatures, a $P_{Se,eqm}$ around 120 mbar resulted in heavily damaged CIGSe layers for smaller diameters, whereas reducing $P_{Se,eqm}$ to 11 mbar led to compact CIGSe micro-absorbers independently of their diameter. To illustrate this effect, Figure 5.14a is a plot of the relevant annealing parameters, T_{Anneal} and $P_{Se,eqm}$, as a function of the damage of the CIGSe micro-absorber for the different diameters that were investigated. To assess the damage of the micro-absorber, the average height of the CIGSe, compared to the SiO_2 layer, is used as criteria to color-map the corresponding circle in the plot. To distinguish between the different diameters, the diameter of each circle is proportional to the corresponding micro-absorber's diameter. In other words, for each set of annealing parameters, 13 concentric circles, representing the 13 different diameters, are color-coded according to the respective absorber's extruded height. To exemplify the criteria that define the scale of the color map, the height map of a compact micro-absorber is shown in Figure 5.14b, giving a green ring in Figure 5.14a, and that of a deformed micro-absorber is presented in Figure 5.14c, giving a red ring.

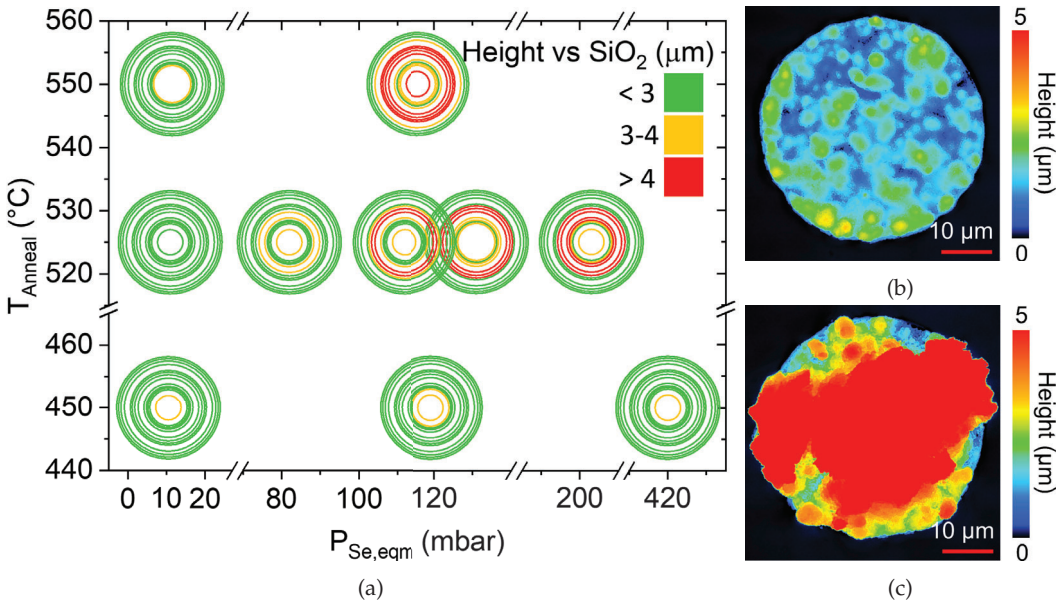

Figure 5.14: a) Colormap representation of the CIGSe absorber's average height, compared to the surrounding SiO_2 matrix, as a function of the annealing parameters (annealing temperature and Se partial pressure). Each group of concentric circles contains 13 data points pertinent to the micro-dots in the same array, i.e. annealed in the same conditions. The diameter of each micro-dot is represented by the diameter of the respective circle, which was calculated with the logarithm of the real micro-dot diameter in order to facilitate visualization. The real diameters are: 500, 400, 300, 200, 100, 80, 60, 40, 20, 15, 12.5, 10 and 5 µm. CLSM height map of a b) compact CIGSe absorber (shown as green in a) - 60 µm diameter, 525 °C and 11 mbar) and a c) deformed absorber (shown as red in a) - 60 µm diameter, 525 °C and 131 mbar).

Independently of the annealing temperature, it is clear that $P_{Se,eqm}$ has a crucial impact on the absorber's morphology. In general, the higher the $P_{Se,eqm}$, the higher the number of damaged micro-absorbers, with those with a smaller diameter being the most

sensitive to $P_{Se,eqm}$. Focusing on the micro-absorbers annealed at 525 °C, each diameter seems to have a different pressure threshold $P_{Se,t}$ above which $P_{Se,eqm}$ causes the absorber to be damaged. Furthermore, this pressure threshold shifts to lower values if T_{Anneal} is increased and to higher values if the T_{Anneal} is decreased. As an example, the micro-absorber with 100 µm diameter is damaged when annealed at 550 °C and 120 mbar, whereas it remains intact when annealed at 525 °C with the same $P_{Se,eqm}$. As a side note, a higher $P_{Se,eqm}$ was also observed to cause more fissures and further damage to the SiO_2 layer. To compare with the previous Cu-rich section, where only 60 % of the micro-absorbers were undamaged, the Na-barriered Cu-poor micro-absorbers annealed at the same conditions (450 °C, 150 mg Se, $P_{N,RT} = 350$ mbar, $P_{Se,eqm} = 420$ mbar) did not show any damage. This further emphasizes the importance of the Na barrier, even for Cu-rich micro-absorbers.

From the front surface, the morphology appearance of all the Cu-poor micro-absorbers, damaged or intact, is similar. Thus, to investigate the reason why the diameter is relevant for particular $P_{Se,eqm}$ and T_{Anneal} parameters, it is of interest to explore the interface between the Mo back contact and the CIGSe layer. To access the back side, the micro-absorbers are transferred onto a strip of kapton tape. CLSM optical images are then acquired from micro-absorbers with different diameters, both from the substrate side (see Figures 5.15a-b) and from the micro-absorber back side (in Figures 5.15c-d). Note that with this method, the damaged micro-absorbers, i.e. with smaller diameters, easily transferred to the tape, leaving behind mostly an empty micro-dot. However, for the intact micro-absorbers, only a small portion of the absorber was transferred to the tape and the rest remained attached to the back contact, proving their superior adhesion to the Mo.

Comparing the back interface of the different micro-absorbers, it is evident that those with smaller diameter show an orange crystalline phase that covers most of the back side. In contrast, the micro-absorbers with larger diameters show mostly a grey phase with a granular structure, which resembles the CIGSe phase. Nevertheless, some orange crystals are also visible, however to a much lower extent. This suggests that the holes with smaller diameter induce the formation of micro-absorbers with a double layer structure, whereas the larger holes show the formation of mostly a single phase. Assuming the double layer structure is responsible for the peeling of the micro-absorbers, it seems that the $P_{Se,eqm}$ greatly influences the formation mechanism of the CIGSe phase, as in the cases of lower $P_{Se,eqm}$, all micro-absorbers were intact.

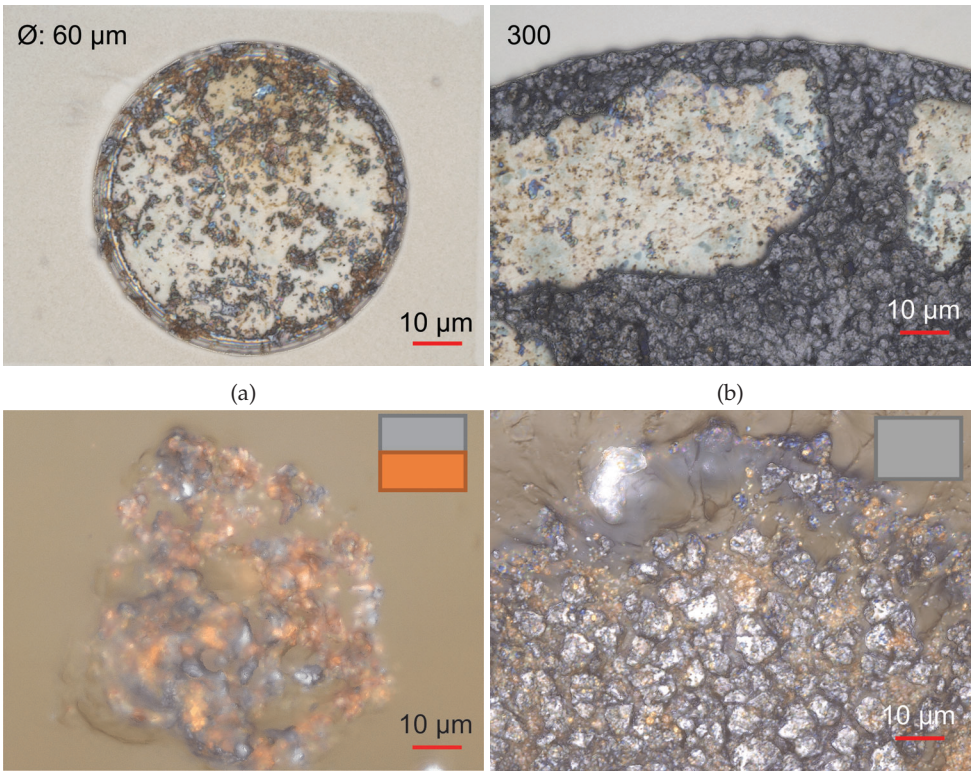

Figure 5.15: CLSM optical image of a a) 60 µm and b) 300 µm diameter micro-dots after removal attempt of the CIGSe absorber. CLSM optical image of the back side of the extracted CIGSe absorber from the c) 60 µm and d) 300 µm micro-dots. The brown background is the kapton tape. A side-view schematic of the double and single layer phase is depicted in the respective image, on the top right corner.

EDX analysis show no sign of Na in this case, which means the Na barrier was effective and these orange crystals are a different phase than that observed in the co-evaporation case, in chapter 4. Furthermore, independently of the diameter of the holes, EDX (at 10 kV) shows a composition ratio (Cu:III:Se) of 1:1:2 at the surface of the micro-absorbers, suggesting a Cu(In,Ga)Se_2 phase. However, concerning the back interface, the analysis could not identify an individual phase. Instead, Raman analysis is able to differentiate phases at the surface and at the back, as shown in Figure 5.16. Figures 5.16a and b are CLSM optical images of micro-absorbers with a large and a small diameter, respectively, to help identifying the investigated regions.

Starting from the front side of the micro-absorbers, remaining inside the holes (spectrum 1), a similar spectrum is obtained for both diameters. The typical modes of CIGSe are observed at 175 cm^{-1} (A_1 mode) at in the range 210-230 cm^{-1} (B_2 and E mixed modes). The A_1 mode's position suggests a low Ga content as also measured with EDX. Additionally, the main peak (A_1 mode) of the the OVC phase, $CuIn_3Se_5$, is measured at 154 cm^{-1} [121]. Focusing on the back interface of the large diameter micro-absorber (spectrum 2), the leftover grey phase shows again the typical modes of the CIGSe phase (A_1 and mixed

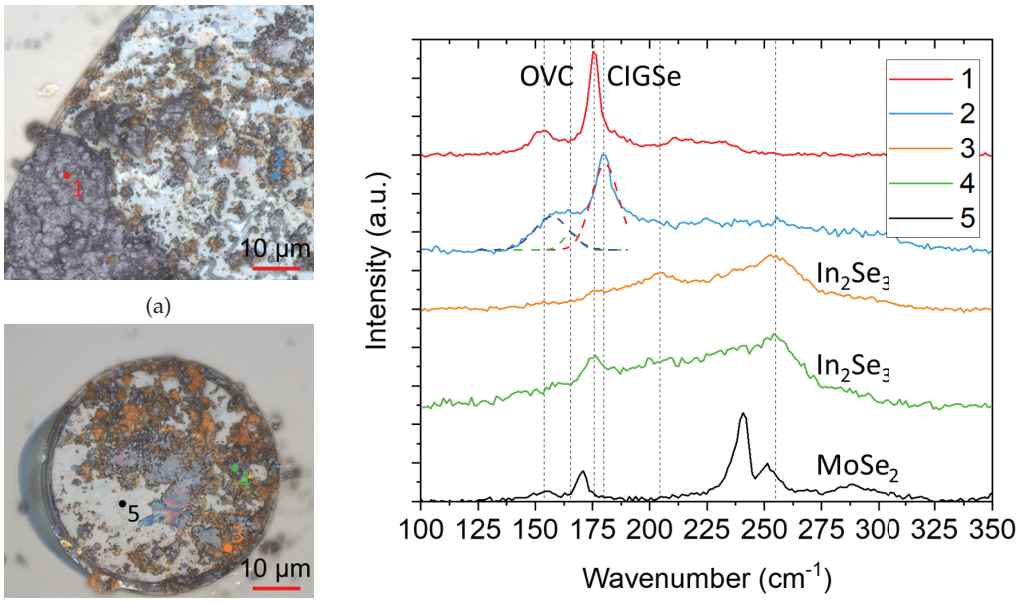

Figure 5.16: CLSM optical image of a a) 400 µm and b) 80 µm diameter micro-dots after removal attempt of the CIGSe absorber. Raman measurement locations are numbered and color-matched to the respective spectra. c) Raman spectra measured from the locations indicated in a) and b). Dashed curves are fittings to the spectrum in location 2, in the 150-190 cm^{-1} range, based on the modes of from the two OVC phases ($CuIn_3Se_5$ - blue peak and $CuGa_3Se_5$ - green peak) and the A_1 mode of CIGSe (red peak).

B_2, E modes), however the wavenumber of the A_1 mode is shifted to 180 cm^{-1}, confirming a Ga-rich CIGSe phase at the back interface. Additionally, a fitting to the 150-190 cm^{-1} range, suggests the presence of two OVC phases at 157 cm^{-1} and 166 cm^{-1}, which match the main modes of $CuIn_3Se_5$ and $CuGa_3Se_5$ phases [121]. Finally, it is possible that some signal from the neighboring orange crystals is measured in the 200-260 cm^{-1} range, as the background level is not reached. To measure these crystals more objectively, two measurements were taken in the hole with smaller diameter, where the density of orange crystals is larger. In both cases (spectra 3 and 4), the most intense peak is located at 255 cm^{-1}, followed by a secondary peak at 204 cm^{-1}. According to literature, this could correspond to a In_2Se_3 phase, where the main peak, at 254 cm^{-1}, is associated with the Se_8 ring vibrations [183, 184]. Given the low CGI (0.72) of the precursor, this phase is in fact expected to be formed. A low intensity Ga-poor CIGSe A_1 mode is also measured at 176 cm^{-1}, given the proximity of the two phases. Lastly, the Raman spectrum of $MoSe_2$ is also shown to insure they do not match with those observed in the In_2Se_3 phase.

To conclude, measurements suggest that the diameter of the micro-absorbers has an influence in the phase formation, where the smaller diameters result in a configuration closer to a double layer of CIGSe and In_2Se_3, whereas the larger diameters form mostly a single layer with a few In_2Se_3 crystals. Since the initial composition was similar, it is hypothesized that the distribution and density of OVC phases is different for distinct diameters.

Influence of Se partial pressure on absorber's ΔE_F

To solve the morphology issue, one could simply anneal with lower $P_{Se,eqm}$, as this reduced the peeling of the micro-absorbers. However, the morphology of the micro-absorbers does not provide direct information about their optoelectronic properties, thus it is relevant to also investigate how the quasi-Fermi level splitting ΔE_F is impacted when the annealing conditions are changed, as it is a figure of merit for the solar cell devices. To separate the effect of the annealing parameters from the effects of the micro-dots diameter, Figure 5.17a shows the ΔE_F measured only from 500 µm micro-absorbers prepared under different annealing parameters, i.e., at different temperatures and different $P_{Se,eqm}$. To address the effects of the micro-dots diameter, Figure 5.17b compares the maximum photoluminescence (PL) counts measured from micro-absorbers with different diameters synthesized under the same conditions.

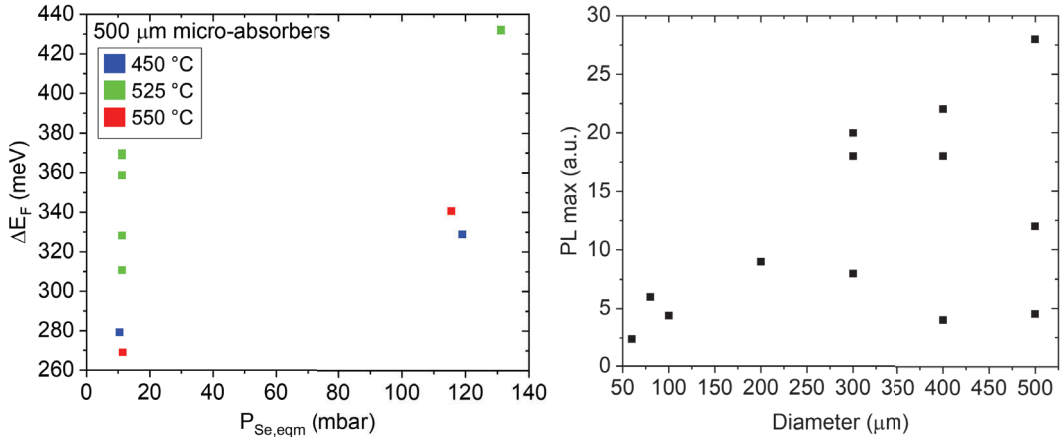

Figure 5.17: a) ΔE_F as a function of the Se partial pressure and temperature during the absorber annealing for micro-dots with a diameter of 500 µm. b) Maximum PL counts as a function of the absorber's diameter. All absorbers compared here were annealed at 525 °C with a $P_{Se,eqm}$ of 130 mbar.

Concerning the impact of the annealing parameters, it stands out firstly that a higher $P_{Se,eqm}$ results in a higher ΔE_F for all annealing temperatures. Conversely, Han et al. had observed that in large area CIGSe the V_{OC}, which is directly connected to ΔE_F, hardly changed (< 5 % change over 1 order of magnitude $P_{Se,eqm}$) with $P_{Se,eqm}$ and was around 400 mV [55]. Here, it is assumed that, like in our process, the deposition of the buffer and window layer only leads to marginal losses in ΔE_F, making it possible to directly compare ΔE_F and V_{OC}. Note that Han et al's process is similar to ours here, except for the annealing temperature which is lower in our case (525 °C compared to 600 °C). Back to Figure 5.17a, increasing the $P_{Se,eqm}$, allowed to improve the ΔE_F up to 430 meV. This highlights that the annealing conditions have a larger impact when using the patterned substrates compared to the typical unpatterned substrates. Regarding the effect of annealing temperature, it is observed that 525 °C had the best result. As mentioned previously, literature has proven that a higher temperature leads to a better performance, which is

also observed here when comparing to 450 °C. However, 550 °C shows a lower performance, which is likely due to the extra stress introduced by the thermal expansion of the SiO_2 matrix and the Na-barrier. Nevertheless, a ΔE_F of 430 meV (or equivalently a ΔE_F loss of 300 meV), without particular process optimization, regarding T_{Anneal} and $P_{\text{Se,eqm}}$, nor post-deposition treatment is encouraging. For comparison, world record CIGSe solar cells have a ΔE_F loss of 106 meV [29].

Moving on to the impact of the micro-absorbers' diameter on their PL signal (proportional to $\exp(\Delta E_F)$), Figure 5.17b suggests a trend where PL signal increases with increasing diameter. However, it also shows an important discrepancy on the PL signal from sister micro-absorber with the same diameter. With the current data, it is not possible to objectively explain the discrepancy, however it could be related to their relative position in the graphite box [141]. Regarding the diameter dependency, it is worth noticing that some of the smaller diameters presented a "damaged" morphology, but still had a significant PL signal. Just like in the discussion about the micro-absorbers' morphology it was observed that different annealing parameters were necessary for each diameter, it is hypothesized that to maximize PL signal in each diameter, a particular set of annealing parameters is required. Thus, from the current dataset, it is not possible to conclude whether or not a particular diameter is better.

A first attempt at performing Na post-deposition treatment, by evaporation in the PVD chamber, was tested with the aim of improving the absorber's ΔE_{F}. This method has generally been adopted for standard sized CIGSe to further improve the absorber's ΔE_{F} [111]. The procedure applied to the standard sized CIGSe absorbers was reproduced with the micro-absorbers. It was observed that, given the low amount of CIGSe material in the micro-dots, the flux of NaF was too large and easily formed large alkali secondary phases, which were detrimental for the morphology of the micro-absorbers. Nevertheless, a slight ($\sim$ 40 meV) improvement in ΔE_{F} was observed, which demonstrates the benefits of the method also in micro-absorbers.

Device characterization

The control of $P_{\text{Se,eqm}}$ was demonstrated to be crucial to obtain a compact morphology and to improve the absorber's ΔE_{F}, both being important parameters to fabricate micro solar cells. In the following, the characterization of absorbers that were converted into micro solar cells is discussed. Given the Cu-poor composition of the absorbers, a KCN (5 wt% for 30 s) treatment [165] is applied to the array, directly followed by the chemical bath deposition of a 50 nm CdS buffer layer. In this case, the KCN treatment is mostly to refresh the absorber's surface from the oxides and Cu-Se phases that may have formed due to air exposition [185]. Stripes of tape were used to form a mask around the individual micro-absorbers. Finally, the transparent conductive oxide layers (i-ZnO/ZnO:Al) are deposited by sputtering, after which the stripes of tape are removed to ensure each cell is electrically isolated from the other.

Figure 5.18a shows the EQE spectrum measured from a 500 µm micro solar cell. The expected parasitic absorption by the CdS buffer layer can be identified in the blue wavelength region, whereas the lower EQE, at longer wavelengths, can be attributed to multiple factors like an incomplete absorption of long-wavelength photons and/or the carrier recombination at the unpassivated back interface. The J_{SC} is calculated by integrating the product of the EQE and the solar spectrum, as detailed in section 2.2.9 of chapter 2, and equates to 31.6 mA/cm^2. Also, the measured bandgap is around 1.0 eV, which agrees with the Cu-poor and low Ga content composition measured from the absorbers [39].

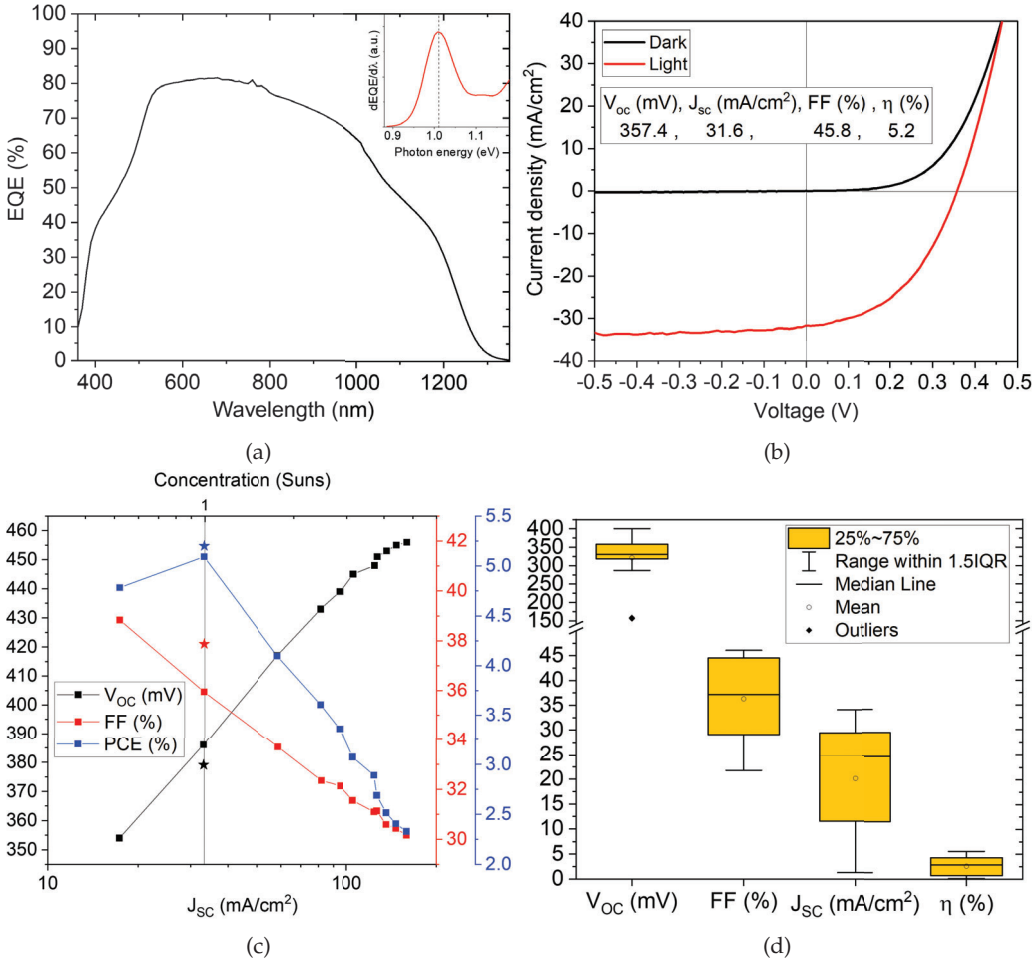

Figure 5.18: a) EQE spectrum measured from a 500 µm micro solar cell, with the respective energy derivative as inset to determine the bandgap. Small bump at 760 nm is an experimental artifact, due to the change of the excitation lamp. b) JV characteristics, in the dark and under illumination, of the same micro solar cell measured in a). Current was corrected based on J_{SC}^{EQE} value measured from EQE. Main JV parameters are shown in a table as inset. c) Concentration series on a sister micro solar cell using a red laser as illumination source. Main JV parameters are reported as a function of the light concentration factor (top axis, shown in log-scale) or equivalently the J_{SC} (bottom axis, shown in log-scale). V_{OC}, FF and PCE were measured for a light concentration up to about 5 Suns. The same micro solar cell was measured with the standard 1 Sun setup and the respective JV parameters are indicated by color-coded star symbols. A vertical black line indicates the 1 Sun illumination. d) Box plot of the main JV parameters, under 1 Sun illumination, covering all 16 measured micro solar cells.

The dark and illuminated JV curves of the same micro solar cell are shown in Figure 5.18b. The champion device showed a V_{OC} of 357 mV, a FF of 45.8 % and a J_{SC} of 31.6 mA/cm^2, leading to a PCE of 5.2 % under 1 Sun. On the one hand, the shunt resistance shows a relatively low value of 100 Ωcm^2, both in the dark and under illumination. On the other hand, the series resistance was estimated to 1-2 Ωcm^2, which is worse than the value measured for the Cu-rich co-evaporated devices (0.1 Ωcm^2), discussed in section 4.2.2 in chapter 4. This difference in series resistance could also explain the lower FF observed here (46 % compared to 60 % for the co-evaporated case).

A light concentration series was measured from a sister micro solar cell using the dedicated micro-setup (red laser as illumination source) and the main JV parameters are plotted in Figure 5.18c as a function of illumination intensity. For comparison purposes, the main JV parameters measured with the standard setup under 1 Sun conditions are also shown. As expected, the V_{OC} increases logarithmically with the excitation intensity, allowing to achieve 456 mV around 5 Suns, which represents an improvement of 70 mV. However, the FF is lower than when measured with the standard setup under 1 Sun conditions. This translates the worse (smaller) shunt resistance measured with the micro-setup (∼23 Ωcm^2 compared to ∼62 Ωcm^2 in the standard setup), the origin of which could not be identified. With higher illumination intensity, even worse values of the shunt resistance were observed, which justifies the observed decrease of the FF. One possible issue could be an inhomogeneous illumination of the micro solar cell. Independently of the setup, it is clear that further efforts are required to improve the shunt resistance, which will allow to further benefit from the PCE gains due to light concentration.

From all the compact CIGSe absorbers in the previous section, 16 micro solar cells with diameters down to 100 µm, were characterized and a box plot of the main JV parameters is plotted in Figure 5.18c. In general, the V_{OC} values are rather close (10-30 mV lower) to the $\Delta E_F/q$ measured from the respective absorbers (see Figure 5.17a). This implies a good band alignment between the absorber, buffer and window layers, which is crucial for optimal device performance. It is worth noting that higher V_{OC} values (400 mV) were measured compared to the champion device (357 mV), however these devices suffered from low FF and J_{SC}, due to a higher series resistance and lower shunt resistance.

To summarize the synthesis of sputtered Cu-poor micro solar cells, it was observed that using a substrate pattern with a higher spacing in-between micro-dots reduced the contamination issues encountered in the previous section. Nevertheless, some level of resist contamination seems to persist. Conversely to the Cu-rich case, an annealing in inert atmosphere was detrimental, given that it led to the formation of larger holes in the absorber's morphology, down to the Mo back contact, and promoted the formation of a secondary phase. In both cases (Cu-rich and Cu-poor), it was highlighted that the precursor's morphology has an important impact in the formation of pure CIGSe. Regarding

the annealing in Se, it was shown that the Se partial pressure and the annealing temperature are key parameters to control the morphology, optoelectronic properties and phase purity of the CIGSe absorber. Furthermore, depending on the diameter of the micro-dot, a different set of parameters were necessary to obtain compact morphologies, which suggests that each diameter requires a distinct set of annealing parameters to optimize the performance of the respective absorber. Finally, multiple Cu-poor micro solar cells were completed and the champion device showed a PCE of 5.2 % under 1 Sun, which is the highest value achieved for bottom-up synthesis of island-shaped micro solar cells. A concentration series was measured and the expected logarithmic increase of the V_{OC} was observed.

To conclude on the sputtering and annealing route, it was demonstrated that the method can produce arrays of CIGSe-based micro solar cells in both Cu-rich and Cu-poor conditions. In the latter case, the implementation of the Na barrier was crucial, as anticipated in chapter 4, however it is hypothesized that it could also be beneficial in the Cu-rich phase, where significant amounts of Na were measured only after annealing in Se. In addition to the Na barrier implementation, further key synthesis parameters for this method were highlighted, which sets guidelines on how to optimize the process in terms of device performance. More precisely, the method has an inherent contamination issue, i.e. resist abrasion into the precursor during the sputtering process, that can be limited by reducing the density of micro-dots in the substrate pattern. In fact, the design of the pattern and the SiO_2 matrix, play important roles in the synthesis process. For instance, the height of the SiO_2 matrix helps shaping the CIGSe absorber, whereas the diameter of the micro-dots has an influence in the formation mechanism. Finally, the Se partial pressure and the annealing temperature have paramount influence in determining the morphology and optoelectronic performance of the CIGSe based micro solar cells.

5.2 Electrodeposited solar cells

The second material efficient method that is explored is a two-step electrodeposition of the metal precursors, followed by the same annealing in a Se-containing atmosphere. The distinction of the electrodeposition steps is that the metal precursors are deposited only in the regions where the metallic Mo layer is exposed, as the SiO_2 layer has the function of masking. This implies that only the required material is deposited locally, resulting in an optimal material consumption. It is worth emphasizing that the substrate, onto which the precursors are deposited, contains no resist layer. Thus, in this case, no resist contamination issues are expected, since the resist is removed before the electrodeposition of the precursor layers, unlike in the sputtering process.

5.2.1 Cu-rich solar cells

Similarly to the sputtered Cu-rich (CGI > 1.0) precursors, no Na blocking layer was used in this case, given the diffusion blocking aspect of Cu-rich precursors observed in chapter 4. The aim here is to also confirm if a different precursor synthesis impacts the Na diffusion.

Precursor characterization

To illustrate the distinct steps in this electrodeposition route, Figure 5.19 presents the optical image, and respective height map, of the same micro-dot at each step of the process. The starting point is the patterned substrate, where the Mo layer is exposed only within the micro-dot structure (in Figures 5.19a and e). The first electrodeposition step is that of Cu, which results in the growth of a Cu layer inside the micro-dots, as exemplified in Figures 5.19b and f. This is followed by the co-electrodeposition of In and Ga, leading to a (In,Ga) layer stacked on the Cu deposit, as visible in Figures 5.19c and g.

An optional step is also shown, in Figures 5.19d and h, that is the annealing of the precursor stack in N_2 inert atmosphere. Focusing on the optical images of the (In,Ga) layer before (Figure 5.19c) and after (Figure 5.19d) annealing, the morphology of the stack does change, as discussed in chapter 3, however the appearance, or color, of the layer remains identical. This again confirms the resist contamination issue, observed in the sputtering synthesis route, is due to the presence of the resist layer during the precursor sputtering step.

The correlative analysis of the electrodeposited precursor layers, discussed in chapter 3, shows that the layers' morphology influences the composition and phase purity of the resulting CIGSe absorber, but also the morphology of the precursor stack itself, which is clearly highlighted here again by the sequence of height maps (Figures 5.19e-g).

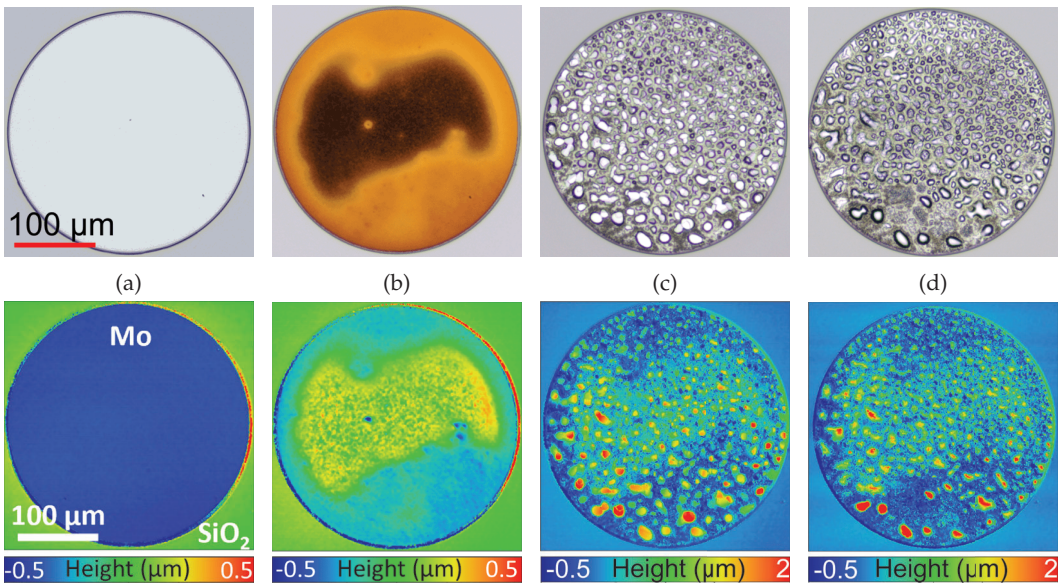

Figure 5.19: CLSM optical images of the same 300 µm diameter micro-dot at each step of the process: a) empty micro-dot. b) electrodeposition of Cu film. c) electrodeposition of In, Ga film. d) inert annealing in N_2. e-h) CLSM height maps of the corresponding optical images (a-d).

Absorber formation

As previously, to convert the precursor stack into the CIGSe absorber, an annealing in Se-containing atmosphere is performed in a tube oven, inside a graphite box. Similar annealing conditions, as for the Cu-rich sputtered precursors, were chosen here. Specifically, the N_2 background pressure was 350 mbar, the mass of Se powder was 150 mg and the annealing duration, at the target temperature, was 10 min. Three different temperatures were considered 450 °C, 500 °C and 550 °C. The range of CGI composition of the absorbers discussed here is 1.1-1.4.

Figure 5.20 shows optical images and height maps illustrating the morphology of a representative absorber synthesized at 550 °C. At this temperature, a few cracks in the SiO_2 are observed, but mostly connected to a micro-dot. Also, at the edge of the sample, the Mo (or $MoSe_2$) layer is peeling locally (not shown). Both observations together suggest that the combination of high temperature and high N_2 background pressure, that is the high resulting Se partial pressure (450 mbar), is causing the growth of an excessively thick $MoSe_2$ layer which leads to the damage observed in the micro-dots and on the SiO_2 layer. This suggests that the thermal expansion is not a problem for this stack (sodalime glass/Mo/SiO_2) and annealing parameters.

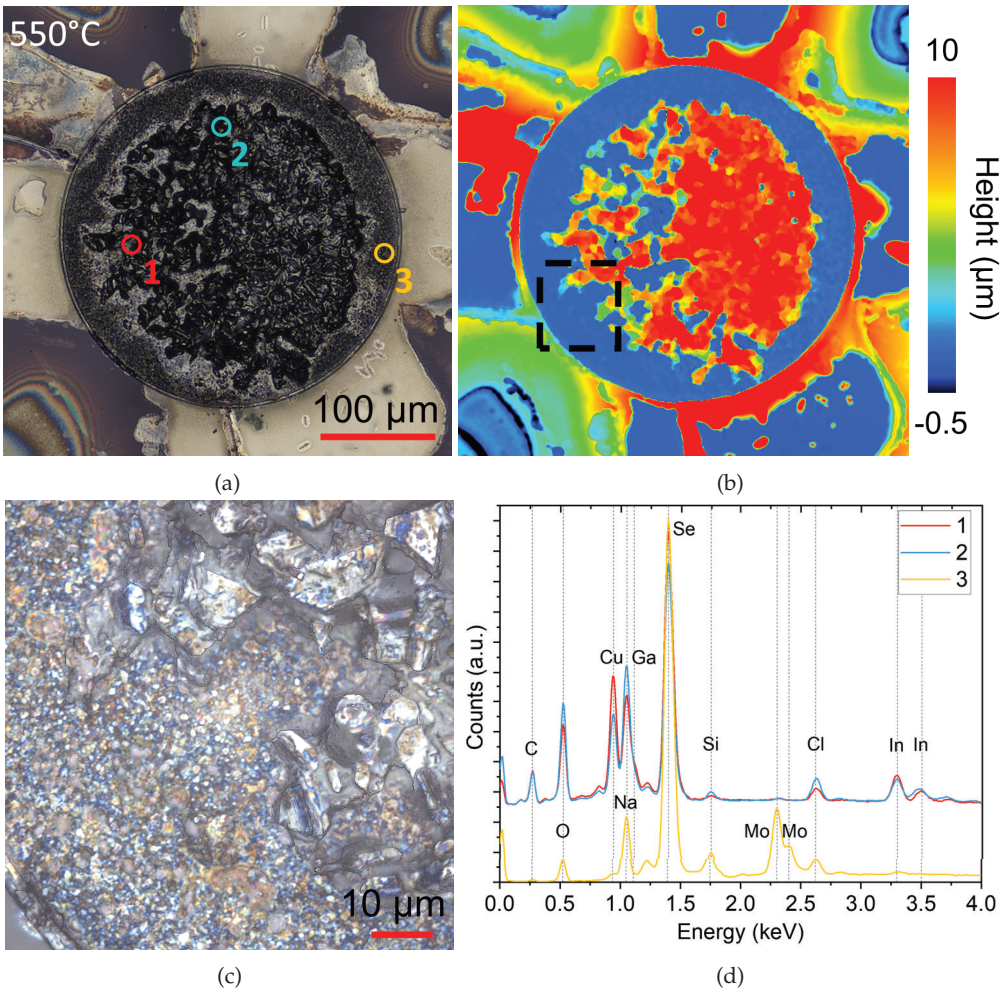

Figure 5.20: a) CLSM optical image of a 300 µm wide micro-dot after an annealing in Se at 550 °C. b) CLSM height map associated with the region shown in a). c) Zoom-in CLSM optical image of the region highlighted by the black dashed box in b). d) EDX spectra acquired from the locations indicated in a). Spectra were measured with 10 kV acceleration voltage.

Focusing on the micro-dot, a damaged $MoSe_2$ layer is clearly visible in dark brown around the micro-dot structure. Inside the 300 µm wide micro-dot, only a portion of the damaged CIGSe absorber remains, leaving the underlying layer also exposed. Figure 5.20c is a zoom-in to the region indicated in the height map, in Figure 5.20b. Here, one can distinguish three different phases by color, which can be guessed from the knowledge acquired with the optical analysis in section 3.3 in chapter 3. In grey, it is the CIGSe phase, in brown/orange the $MoSe_2$. The blue phase was also observed with the Cu-poor sputtered absorber in chapter 4, which allows to guess this phase is Na-related. The EDX spectra analysis, in Figure 5.20d, shows that the composition, in the regions indicated in Figure 5.20a, agree with the suggestions from CLSM analysis. In addition, the presence of the Cl peak allows to further anticipate the formation of NaCl, similarly to the Cu-poor sputtered absorber. Yet again, the Cu-rich precursor was not enough to contain the Na diffusion, as was the case in the co-evaporated absorber.

Reducing the annealing temperature to 500 °C, and thus the Se partial pressure to 420 mbar, considerably reduced the expansion of the $MoSe_2$ layer. Nevertheless, it is still possible to identify an overly thick $MoSe_2$ layer surrounding the micro-dot, in the morphology optical image in Figure 5.21a. Nevertheless, the CIGSe seems intact, as also suggested by the corresponding height map. However, the morphology of the CIGSe layer displays circular lumps, which are considerably higher compared to the remainder of the layer. The optical zoom-in, in Figure 5.21c, does not provide directly a reason for the origin of the lumps, however, in terms of phases, one can identify the light grey CIGSe, a few $Cu_{2-x}Se$ platelets in dark grey and numerous Na-related phases in blue. Here, they are only visible at the surface, as the CIGSe absorber is intact, however they are very likely distributed throughout the absorber's thickness and interfaces, like for the absorber discussed above.

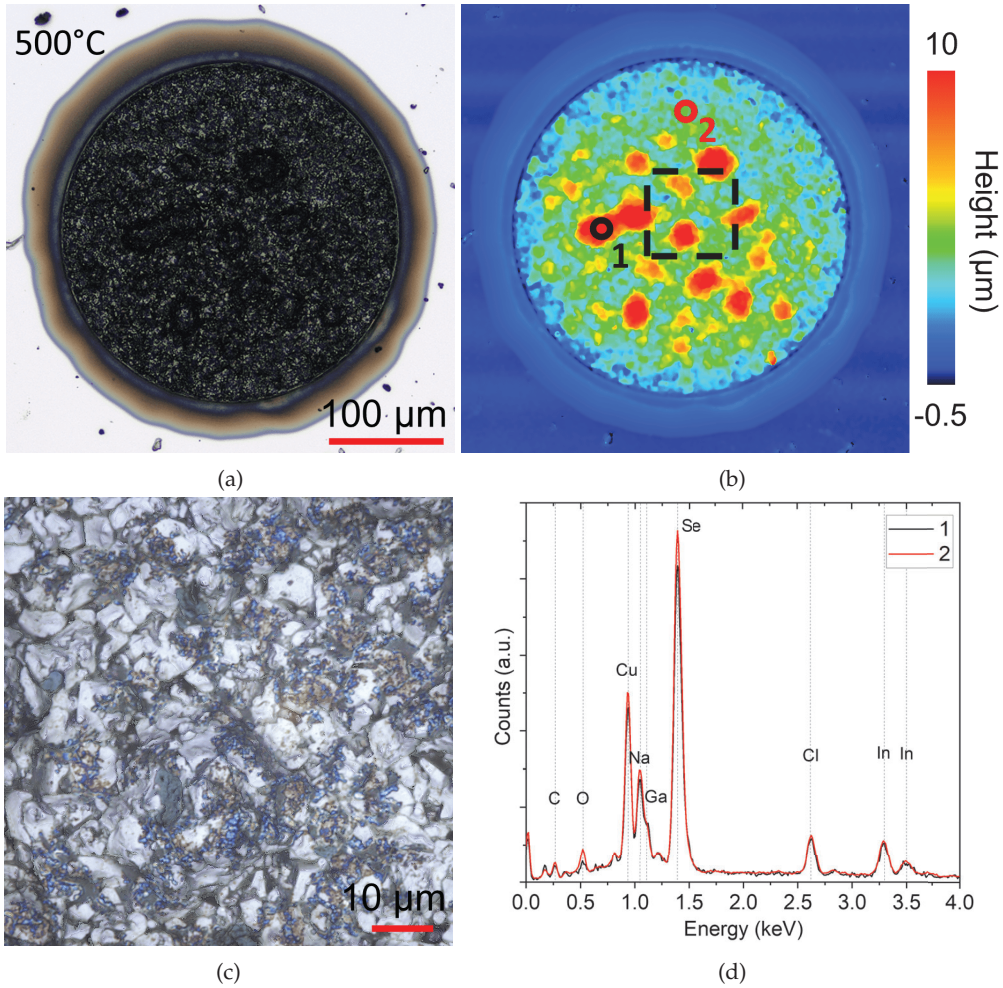

Figure 5.21: a) CLSM optical image of a 300 µm wide micro-dot after an annealing in Se at 500 °C. Brightness adjusted in image a) for visual purposes. b) CLSM height map associated with the region shown in a). c) Zoom-in CLSM optical image of the region highlighted by the black dashed box in b). d) EDX spectra acquired from the locations indicated in b). Spectra were measured with 10 kV acceleration voltage.

Figure 5.21d shows the EDX spectra, taken in the two regions indicated in Figure 5.21b. Both spectra are identical, showing no composition difference. The Cl peak is still present, which indicates that a consequent Na content is present in the absorber, despite the temperature decrease and the Cu-rich composition. It is worth noting that despite using a Na-containing electrolyte for the electrodeposition of the Cu layers, no Na was detected in the precursor stack, which attributes the Na appearance exclusively to its diffusion from the soda lime glass substrate. Although, no particular correlation is observed between the lumps and the Na content, it is worth noting that the average Na/Cu ratio is 1.1, which is excessively high compared to standard CIGSe synthesis (< 0.04) [141]. Thus, it is hypothesized that the excessive Na content is directly or indirectly responsible for the anomalous morphology. Also, as was the case for the highest temperature, the Cu-rich composition does not completely block the Na diffusion, from the substrate, when high Se partial pressures are used. Thus, a Na barrier is also required for the Cu-rich cases.

Further reducing the annealing temperature down to 450 °C (Se partial pressure of 390 mbar), allowed to obtain a promisingly compact absorber morphology, as shown in Figures 5.22a and b. Also, no excessive $MoSe_2$ layer is visible beyond the diameter of the micro-dot. In fact, the optical zoom-in, in Figure 5.22c, shows a light grey CIGSe phase with relatively large grains and dark grey platelets of $Cu_{2-x}Se$, as expected given the Cu-rich precursor's composition. No further phases are visible at the surface and EDX analysis, in Figure 5.22d, confirms that the Na content is considerably reduced in the different regions of the absorber. Note that the Cl signal is also suppressed and this despite using the same Cl-contaminated graphite box. Otherwise, the different regions show distinct relative compositions due to the inhomogeneous Cu layer, as was discussed in chapter 3.

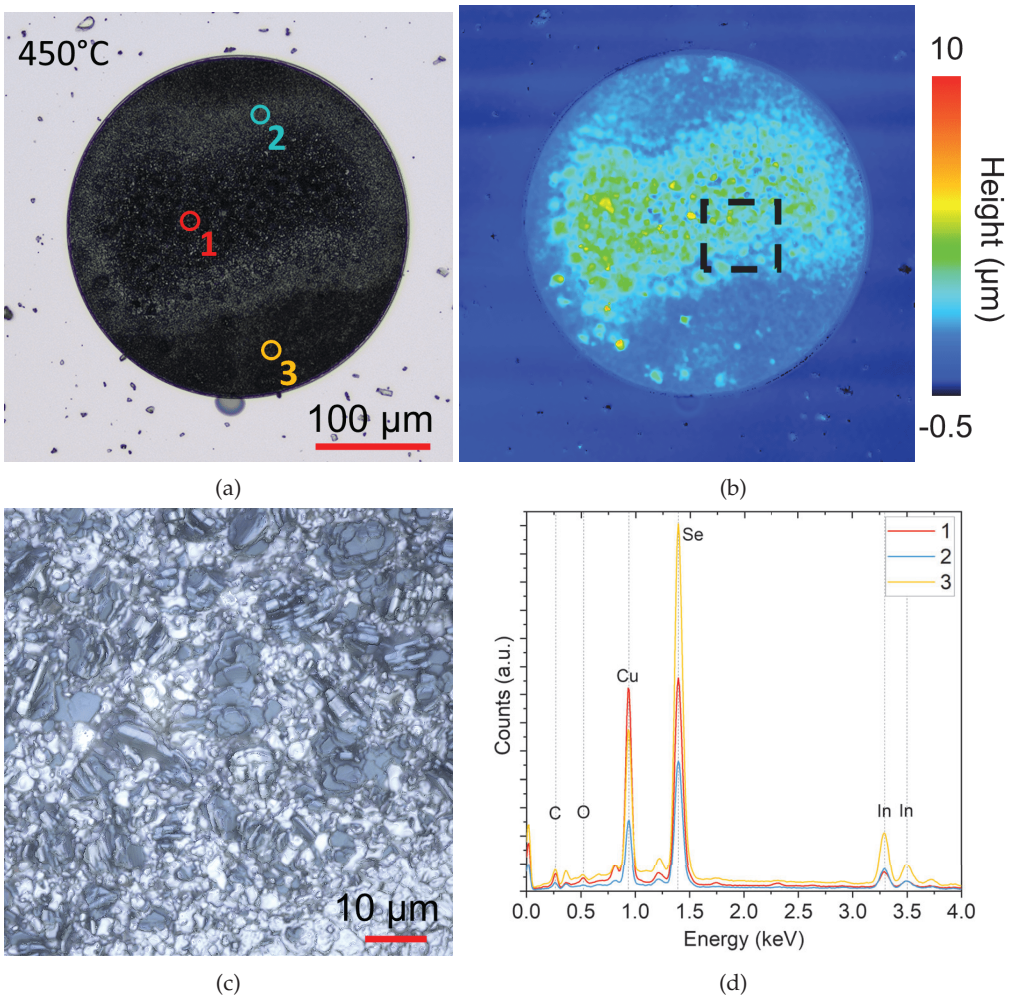

Figure 5.22: a) CLSM optical image of a 300 µm wide micro-dot after an annealing in Se at 450 °C. Brightness adjusted in image a) for visual purposes. b) CLSM height map associated with the region shown in a). c) Zoom-in CLSM optical image of the region highlighted by the black dashed box in b). d) EDX spectra acquired from the locations indicated in a). Spectra were measured with 10 kV acceleration voltage.

Strikingly, despite the same annealing conditions as the sputtered Cu-rich case, no Na is observed here in the absorber, unlike the sputtered case, where a significant amount of Na was present after the annealing in Se. This suggests that the synthesis of the precursor somehow affects the diffusion of Na.

An interesting trend is observed when comparing the morphology of the precursor and that of the absorber. For this, Figure 5.23 regroups the height maps of two absorbers, and respective precursors, synthesized at 450 °C and likewise, two absorbers produced at 500. °C. The top row contains the precursors and bottom row the CIGSe absorbers.

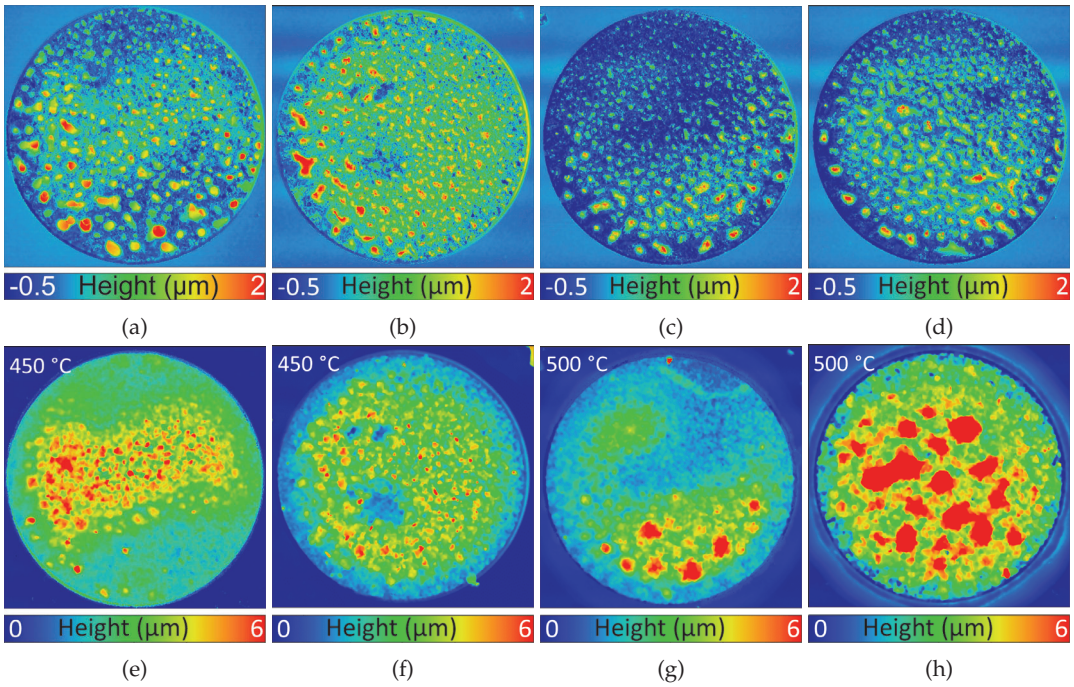

Figure 5.23: CLSM height maps of four (a-d) Cu and (In,Ga) precursor stacks with distinct morphologies and (e-h) respective resulting absorber's morphologies after annealing in Se. The annealing temperatures are indicated at the top left corner of the height map.

As discussed in the precursor section, the particular morphologies of the precursor stacks are mostly induced by the Cu layer. Interestingly, these features remain apparent after the annealing in Se atmosphere, independently of the temperature. This suggests that the diffusion of elements is mostly vertical when forming the CIGSe phase. Furthermore, these results put forward the importance of the precursor's morphology, as it is reflected in the corresponding absorber's morphology. Having achieved compact CIGSe absorbers, in the following, the absorbers were finished into solar cells and characterized.

Device characterization

To assess the optoelectronic quality of the absorbers, synthesized at 450 °C, spectrally-resolved photoluminescence was measured and is plotted in Figure 5.24a in logarithmic scale. The PL signal of the absorber is characterized by the band-to-band transition at around 1.1 eV. Additionally, a broad defect is visible around 0.75 eV, which shows a luminescence of about 1 order of magnitude higher compared to the band-to-band transition. This defect transition seems to be present in low Ga content Cu-rich CIGSe absorbers [186]. This is expected to greatly impact the V_{OC} of the final solar cell.

After completing the absorbers into micro solar cells, JV measurements were performed to measure their efficiency. However, only the solar cells with the absorbers synthesized at 450 °C show a diode behavior, whereas those deposited at 500 °C displayed an ohmic behavior, likely due to the excess of Na observed previously. Figure 5.24b shows the JV characteristics of the best Cu-rich micro solar cell, with the main parameters as

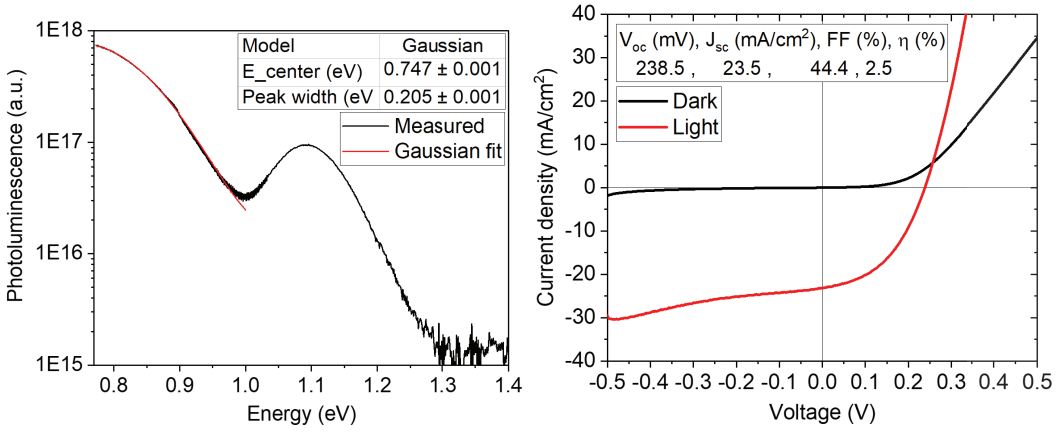

Figure 5.24: a) PL spectrum measured from the Cu-rich CIGSe absorber. Fitting parameters of the broad defect are shown as inset. b) JV characteristics in the dark and under illumination of an electrically isolated micro solar cell. Key parameters are summarized as inset.

inset. As suggested by the PL analysis, V_{OC} of the device is rather limited due to the broad defect observed. The measured J_{SC} also seems to be limited by a shunt path, i.e. a too low shunt resistance, which could not be identified. Thus, the resulting efficiency for the device is 2.5 %.

In summary, Cu-rich micro solar cells were synthesized with the two-step electrodeposition and annealing method. The achieved PCEs are superior to the Cu-rich micro solar cells, made by sputtering and annealing, possibly due to the absence of contaminants during the growth of the precursor layers. A common aspect of the two methods was the presence of Na in the absorber after annealing in Se and this despite that in one case the precursor is a blend of metals and in the second case it is a stack of metal layers. This confirms that the Cu-rich composition is not enough to block the Na diffusion from the soda lime glass, when high Se partial pressures are used in the annealing. Thus, implementing a Na barrier here, like was done for the Cu-poor case, is also beneficial. Furthermore, it was shown that a two-step electrodeposition process requires careful control of the layers' morphology as it dictates the morphology, and phase formation, in the subsequent steps.

5.2.2 Cu-poor solar cells

In the following, Cu-poor CIGSe absorbers are investigated. As for the Cu-poor sputtered case, the precursors were deposited on a patterned substrate with a Na barrier (100 nm SiO_xN_y) below the Mo back contact. The pattern used here was the square pattern with a fix micro-dot diameter (300 µm) to minimize flux inhomogeneities during the electrodeposition of the precursor layers. In terms of synthesis, there is no particular difference between the Cu-rich and Cu-poor precursors, except for the relative thickness of the Cu and In, Ga layers. Except that, due to a technical error during the Cu electrodeposition, also some Ag (from the counter electrode) was deposited.

In sections 4.3 (chapter 4) and 5.1.2 (chapter 5), it was observed that the Se partial pressure (or $P_{Se,eqm}$) influences the morphology of the absorber and its adhesion to the Mo back contact. Given that here the precursor is synthesized with a different method, the question that is addressed in this section is if a distinct precursor synthesis method also impacts the morphology and adhesion of the final CIGSe micro-absorber to the back contact. For this, sister electrodeposited precursors were annealed at distinct $P_{Se,eqm}$ and their morphology is monitored with CLSM. Figures 5.25a, b and 5.25c show CLSM optical images of representative micro-absorbers annealed at 525 °C with a $P_{Se,eqm}$ of 11 mbar, 40 mbar and 131 mbar respectively.

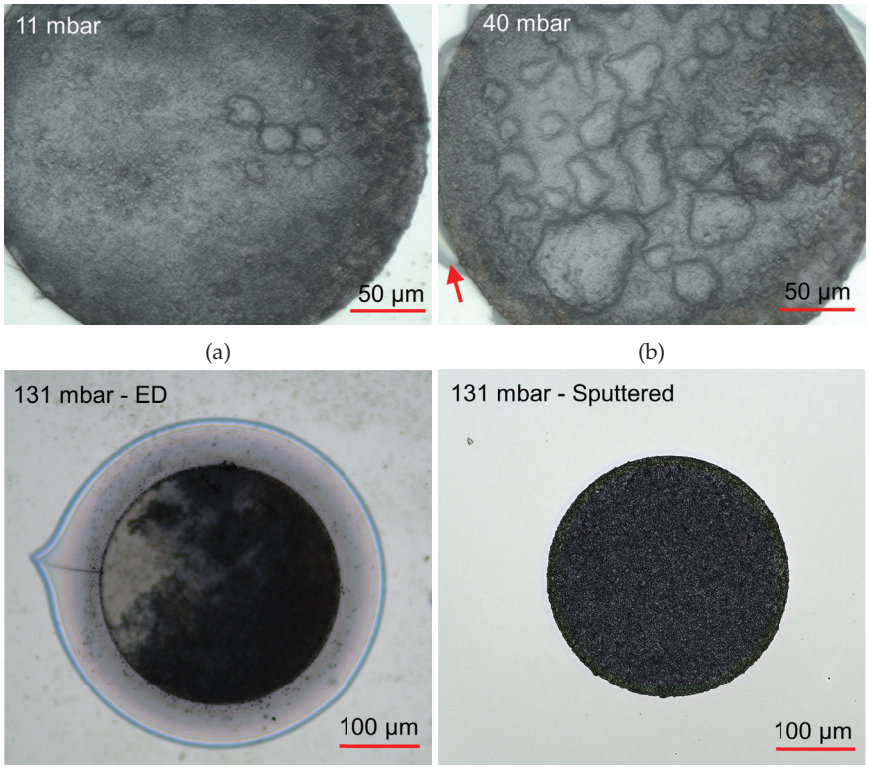

Figure 5.25: CLSM optical image of 300 µm wide CIGSe micro-absorbers after the annealing in Se of the electrodeposited precursors at 525 °C with a Se partial pressure of: a) 11 mbar, b) 40 mbar and c) 131 mbar. Contrast was adjusted in images a) and b) for visual purposes. The red arrow in c) indicates a region where $MoSe_2$ formed (underneath the SiO_2 layer). For comparison purposes, d) is a CLSM optical image of a sputtered micro-absorber annealed under the same conditions as the micro-absorber shown in c).

For the two lower $P_{Se,eqm}$, the absorbers did remain at least partially attached to the Mo back contact, however for the higher $P_{Se,eqm}$ (131 mbar), no absorber material was left inside the micro-dot after the annealing. Furthermore, it can be seen in Figure 5.25c that a $MoSe_2$ layer formed underneath the SiO_2 matrix and even extended about 50 µm beyond the diameter of the micro-dot. Clearly, in this case, too much Se was provided to the precursor, causing the formation of an overly thick $MoSe_2$, compromising the adhesion of the CIGSe itself. Reducing $P_{Se,eqm}$ to 40 mbar ensured that the absorber layer

remained intact and within the micro-dot, nevertheless some $MoSe_2$ can still be identified in some regions along the perimeter of the micro-dot, as highlighted by a red arrow in Figure 5.25b. Regarding the morphology of the absorber itself, multiple protruding lumps are visible, with some reaching heights of 20 µm above the rest of the layer. This suggests that these are hollow lumps, which in turn implies a weak adhesion of the CIGSe to the Mo layer. Both the excess $MoSe_2$ and the lumps are considerably reduced with the lowest $P_{Se,eqm}$ (11 mbar). For comparison purposes, Figure 5.1e shows a CIGSe micro-absorber synthesized from a sputtered precursor at the same conditions as the micro-dot shown in Figure 5.25c (131 mbar). In this case, no $MoSe_2$ is visible. This suggests that for the sputtered case, the Se atoms take longer to diffuse through the precursor/absorber and reach the Mo back contact comparatively to the electrodeposition case, implying a thinner $MoSe_2$ layer and consequently a better CIGSe adhesion.

To also illustrate the impact of $P_{Se,eqm}$ on the morphology of the electrodeposited absorbers, Figure 5.26 shows the average height of the absorbers, compared to the SiO_2 layer, as a function of the $P_{Se,eqm}$, for an annealing temperature of 525 °C. The results for the sputtered absorbers, that were prepared under similar conditions, are also shown. Note that in both cases, a precursor thickness of 0.6-0.8 µm is estimated.

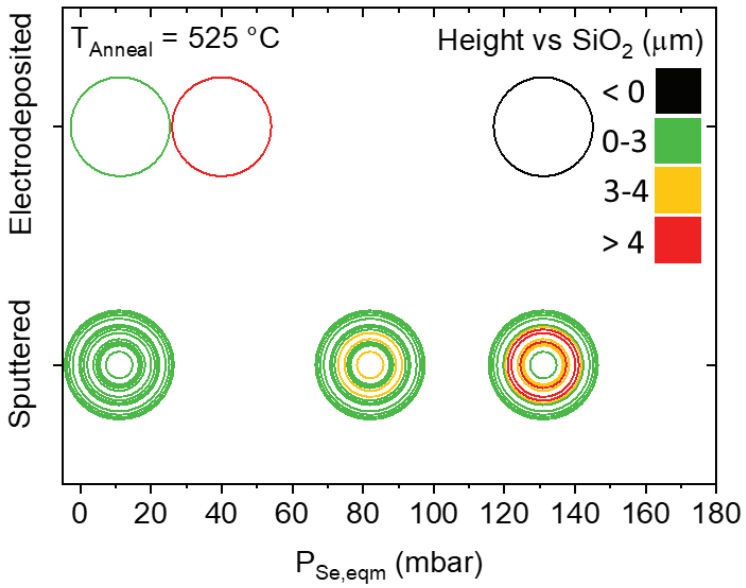

Figure 5.26: Colormap representation of the CIGSe absorber's average height, compared to the surrounding SiO_2 matrix, as a function of the Se partial pressure for electrodeposited and sputtered micro-absorbers. The annealing temperature is 525 °C. The data related to the sputtered samples is the same shown in Figure 5.14. Note that the y-axis here differentiates synthesis method and not annealing temperature. For the electrodeposited samples, the average height of the micro-absorbers is shown as all have the same diameter (300 µm).

In this representation, it is clear the range of $P_{Se,eqm}$, that results in a compact CIGSe absorber, shifts to lower pressure values for the electrodeposited precursor. This implies that the synthesis of the precursor indeed impacts the morphology and adhesion of the CIGSe absorber. Based on these observations, it is speculated that the precursor's double

layer structure, i.e. Cu/(In,Ga) stack, in the electrodeposition case, requires more diffusion of the elements to form the binary $Cu_{2-x}Se$ and In_xSe_y phases, and eventually form the CIGSe phase, which implies that a higher flux of Se atoms (from a higher $P_{Se,eqm}$) increases the possibility of Se atoms to reach the back contact and form $MoSe_2$. By decreasing $P_{Se,eqm}$, less Se atoms are available, effectively slowing down the reaction mechanisms that require Se, allowing for the binary selenides to form without an excess of Se atoms. Conversely, the sputtered precursor is already an alloy, which could facilitate the formation of the binary selenides, and thus the CIGSe phase, at higher $P_{Se,eqm}$.

Device characterization

Given the better adhesion of the CIGSe layers, the absorbers annealed at the lowest $P_{Se,eqm}$ (11 mbar) were finished into micro solar cells. However, since some regions still had an apparent low adhesion, a double layer of CdS buffer layer was deposited to minimize the risk of a shunt path between the window layers and the Mo back contact. The thicker buffer layer is expected to reduce the JV parameters by at most 10 % [187]. For the deposition of the window layers, a similar procedure as for the Cu-poor sputtered case was followed (see section 5.1.2). Prior to the deposition of the window layers, PL measurements were taken from the absorbers made through the electrodeposition route. For comparison, the PL spectrum from a sputtered absorber, with a ΔE_F of 430 meV, is also plotted in Figure 5.27a.

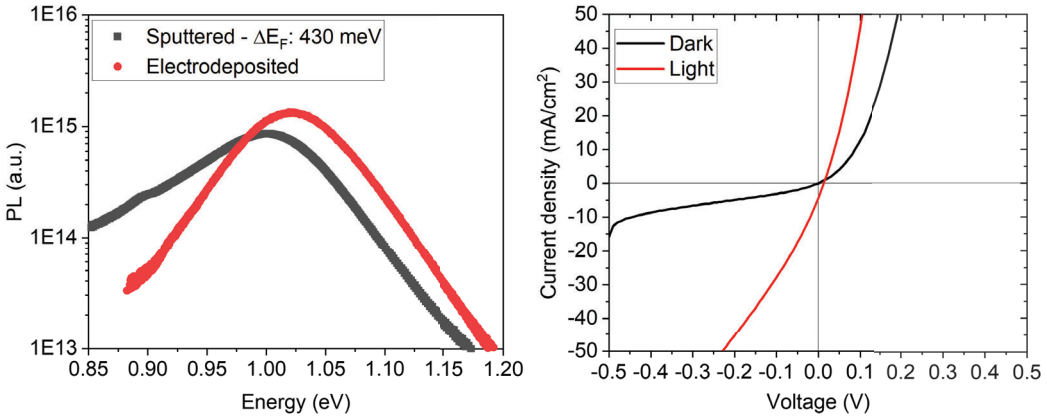

Figure 5.27: a) PL spectra measured, under the same conditions, from an electrodeposited Cu-poor CIGSe absorber and a sputtered Cu-poor CIGSe absorber. b) JV characteristics in the dark and under illumination of a micro solar cell resulting from the electrodeposition synthesis route.

Since the two absorbers were measured under the same conditions, one can compare their PL. In this case, the electrodeposited absorber shows a slightly higher PL signal, which suggests a similar ΔE_F. The shift in the PL peak, of the electrodeposited absorber, may be due to the Ag inclusion [188]. Despite the promising PL signal, both JV curves, in the dark and under light, show issues with the resulting micro solar cell, as is visible in Figure 5.27b. Indeed, the JV in the dark shows a rather low shunt resistance of 40 Ωcm^2.

Under illumination, the observed shunt resistance is further reduced to $5\,\Omega cm^2$, and a very low V_{OC} is observed. It is possible that, given the initially not so good adhesion of the CIGSe to the Mo layer, the deposition of the window layers further damaged the absorber, leading to a very poor conversion of the measured ΔE_F into V_{OC}.

In short, it was observed the synthesis of the precursor layer has an impact on the range of Se partial pressures that result in a compact CIGSe absorber and thus, with better adhesion to the Mo back contact. Specifically, it is suggested that depending on which metallic phases are in the precursor, different fluxes of Se are required to form a similarly compact CIGSe layer.

To conclude the two-step electrodeposition and annealing method, it was demonstrated that also this route requires the implementation of a Na barrier independently of the CGI ratio, reflecting the fact that the Na diffusion is induced by the substrate's geometry. Furthermore, it was observed that the synthesis of the precursor, in particular which phases are formed, impacts how the subsequent annealing in Se should be performed to ensure compact CIGSe absorbers. Finally, although micro solar cells with lower PCE were achieved, it is expected that, with little optimization, this method could yield PCEs similar to those achieved with the sputtering route.

5.3 Summary

In this chapter, two material efficient methods are investigated with the aim of growing CIGSe based micro solar cells on patterned array substrates. For each method, both Cu-rich and Cu-poor CIGSe compositions were synthesized and working devices were obtained, demonstrating the potential application of the two methods.

The implementation of the Na barrier in the array stack was essential, not only for the Cu-poor case, as first anticipated, but also for the Cu-rich CIGSe absorbers. Indeed, the Se partial pressure, during the annealing step, was shown to enhance the diffusion of Na from the soda lime glass, which overcomes the blocking effect of the lack of Cu-vacancies. Furthermore, the morphology, phase purity and optoelectronic properties are also influenced by the Se partial pressure, which puts forward that a fine control of the Se supply is crucial independently of the specific annealing method that is used. This also defines the direction of research on how to optimize the different properties of the CIGSe absorbers. Additionally, the morphology of the metal precursors must also be optimized in both synthesis methods to avoid phase inhomogeneities. As anticipated, Cu-poor CIGSe micro solar cells led to higher PCEs compared to Cu-rich.

The sputtering and annealing method suffers from a contamination issue, during the sputtering of the precursor, which can affect the potential PCEs achieved. Nevertheless, the issue can be partly addressed by adjusting the design of the substrate pattern, more precisely, by increasing the space in-between neighbour micro-dots. Following up on the substrate pattern, the height of the SiO_2 matrix plays an important role in shaping

the CIGSe absorber and the diameter of the micro-dots has an influence in the formation mechanism.

Chapter 6

Energy balance - A pedagogical approach to energy

The previous chapters focused on the scientific work on the investigation of the material efficient synthesis and characterization of CIGSe-based micro solar cells using patterned substrates. As hinted to in the introduction, in addition to pushing the boundaries of science and technology, experts can educate the general public in order to popularize science and give the opportunity to the average citizen to follow the scientific progress and grasp its implications, both at the research level as well as at a societal level. In this way, every citizen can better assess the situation at hand and form their own opinion regarding the latest topics. The current climate crisis is a perfect example of a problem that directly affects the biosphere, and in particular every human being. Therefore, everyone should be able to be informed and discuss it on an equal footing with the pertinent metrics. For this, pedagogic tools can help to overcome the understanding of complex concepts and directly discuss the implications of the actions themselves, which depend on and affect everyone. In this context, experts can fill the gap.

In his book, David MacKay takes an objective approach to assess the anthropogenic environmental impact and presents a methodology on how to attribute meaningful and comparable numbers to the multiple facets that are involved in the problematic of climate change [189]. Based on his approach, the Energy4Life (E4L) team has developed an online pedagogical tool to answer the following question: Can the G.-D. of Luxembourg meet its energetic needs using renewable energy sources and how much land area would it need to deploy? [190]. In a nutshell, by answering a few simple questions on our energy lifestyle, one can find out the approximate land area that would need to be covered with renewable energy sources, to sustain that lifestyle. To provide the audience with more than numbers, the Energy balance game was designed and is a materialization of the E4L online tool. The aim was to develop a pedagogic tool to present the E4L concept to the general public and high school students in a concise and revealing experience. This chapter is a tutoring on how the realisation of the Energy balance, as a pedagogical tool, was developed and may serve as a support for other concepts. The tutoring is showcased for Luxembourg, but can be adapted to any region or country.

In short, the following sections offer a description of the design of the Energy balance game, which is based on a pedagogic approach to address the complex and often intangible concept of energy. A description of the different components is given, as well as, the details of the calculations used to convert the energies into tangible quantities. Additionally, a rules description of the current version of the game is presented along with a discussion of possible expansions or adaptations that could widen the utility of the game into other concepts.

6.1 Components

The different components that make up the energy balance are: (i) a weighing scale, (ii) a question sheet, (iii) an answer sheet, (iv) weighted tokens, representing the possible consumption and production possibilities (v) a map of the region of interest. In the following, an overview of the conception and principle behind each component of the energy balance.

6.1.1 Weighing scale

The weighing scale was chosen to be a wooden two-plate scale based on the *Zenzi-Werken* model [191]. In this configuration, one plate is used as the energy consumption side, whereas the second plate is reserved for the energy production. The mass resolution of the fabricated scale was in the range of 1-2 g, which also defines the lowest mass value to be used. This value mostly depends on the friction of the different parts of the scale. In this case, plywood was used as the base material and individual parts were laser cut. Figure 6.1 is an optical image of the assembled wooden weighing scale.

Figure 6.1: Optical image of the assembled wooden weighing scale.

6.1.2 Question and answer sheets

The next components that are addressed are the question and answer sheet, as these are similar. For ease of visualization and to highlight the answers that are chosen, a separate question and answer sheets are used. Nevertheless, the answer sheet is identical to the question sheet, except that the fields containing the answer tokens are left blank. Given the dimensions of the weighted answer tokens, A3 format sheets are utilized. Figure 6.2 displays the question sheet with and without the weighted answer tokens.

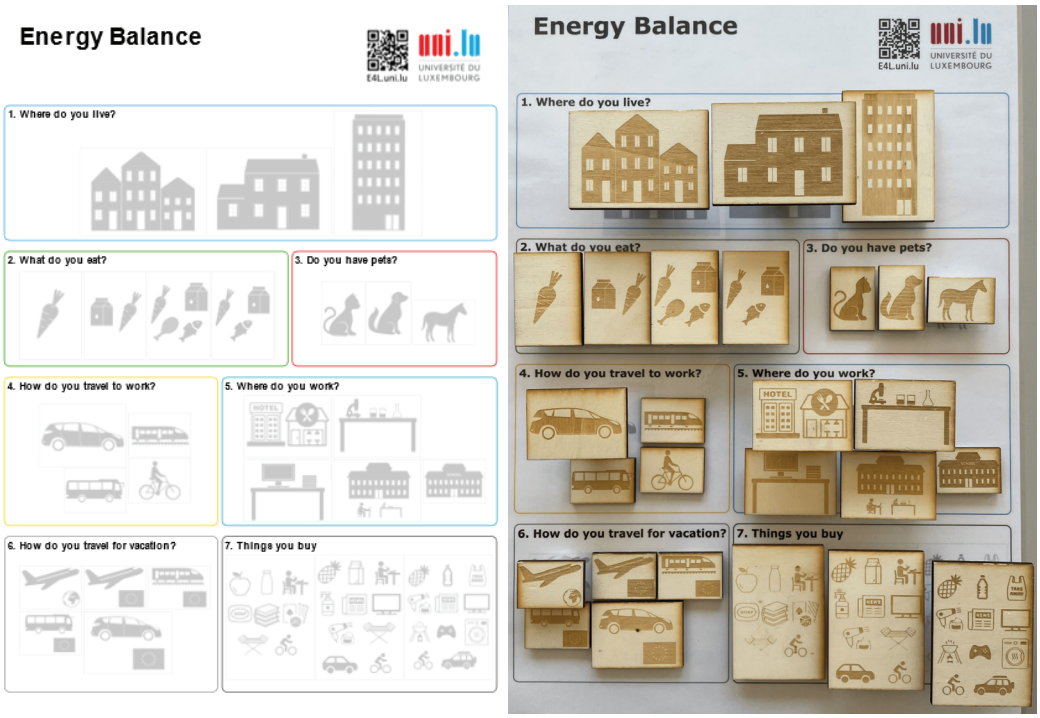

(a) (b)

Figure 6.2: a) Question sheet. b) Optical image of the question sheet with answer tokens prepared.

6.1.3 Production map

The production map is intended to display the percentage area of the region of interest (ROI) that needs to be covered with production units, in order to satisfy the amount of energy consumption. For this, the map consists of the ROI divided in a grid with 100 squares, each having the same dimensions as an individual production unit.

To provide the reader with the most flexibility in terms of dimensions and materials, different constraints for the map areas and tokens' weight and dimensions are suggested. For the production map, two constraints can be considered, either one chooses the dimensions of the ROI in the map sheet (G.-D. of Luxembourg, in this case) or the area of a single production unit (solar cells for instance). Given that A3 sheets are used to print the map, it is more convenient to proceed with the first constraint. For this, one can start from a geographic map, showing the delimitations of the ROI, and rescale it to

the desired real dimensions (to fit an A3 sheet in our case). By measuring the total area of the ROI $A^{ROI}_{A3\,sheet}$ (in cm^2) and dividing it by 100, one can calculate the real area that occupies a single production unit $A_{1\,unit}$. Taking the square root of this value, yields the side length $d_{1\,unit}$ of the equivalent square.

$$d_{1\,unit} = \sqrt{A_{1\,unit}} = \sqrt{\frac{A^{ROI}_{A3\,sheet}}{100}} \tag{6.1}$$

To generate the map itself, one can create a grid of squares, each with an area $A_{1\,unit}$, and overlap it with the map of the ROI. Although this concludes the production map itself, it is required to calculate the equivalent energy $E^{prod.}_{1\,unit}$ that a single production unit can generate, for latter reference. In this case, one can simply calculate an area conversion factor f_{area}, which is the ratio of the real area of the ROI A^{ROI}_{Real} to $A^{ROI}_{A3\,sheet}$.

$$f_{area} = \frac{A^{ROI}_{Real}}{A^{ROI}_{A3\,sheet}} \tag{6.2}$$

The conversion factor allows to calculate the area to which a single production unit corresponds to in real scale. Therewith, one can determine $E^{prod.}_{1\,unit}$ as follows:

$$E^{prod.}_{1\,unit} = A_{1\,unit} \cdot f_{area} \cdot E^{prod.}_{density} \tag{6.3}$$

In our case, $E^{prod.}_{density}$ is the yearly energy density produced by solar cells. As an example, Figure 6.3 shows the finalized map for the G.-D. of Luxembourg.

6.1.4 Weighted tokens

Moving on to the weighted tokens, the aim is to associate each individual token with a possible answer (for consumption and production) and have its mass proportional to the energy that is associated with the answer. Three information channels are thus being used to convey the associated amount of energy: the icon that represents the answer, the dimensions of the token (area and height) and the weight of the token, as shown in Figure 6.4. Note that the tokens are made up of two parts, the wooden plate with the engraving and the aluminum rod for the weight. For simplicity, the description below neglects the weight of the wooden plate itself, since it is much lower than the rod. Also, the choice of using two materials (wooden plate and aluminum rod), instead of one (single weight with the icon engraved on it), was only determined by the availability of resources and services.

The calculations to determine the corresponding mass of each token, relies on defining an energy-mass conversion factor f_{energy}, which depends on the constraint that is chosen. Different approaches can be taken, for instance, define the maximum or minimum weight, impose a specific range of dimensions, the density of material(s) used, etc.

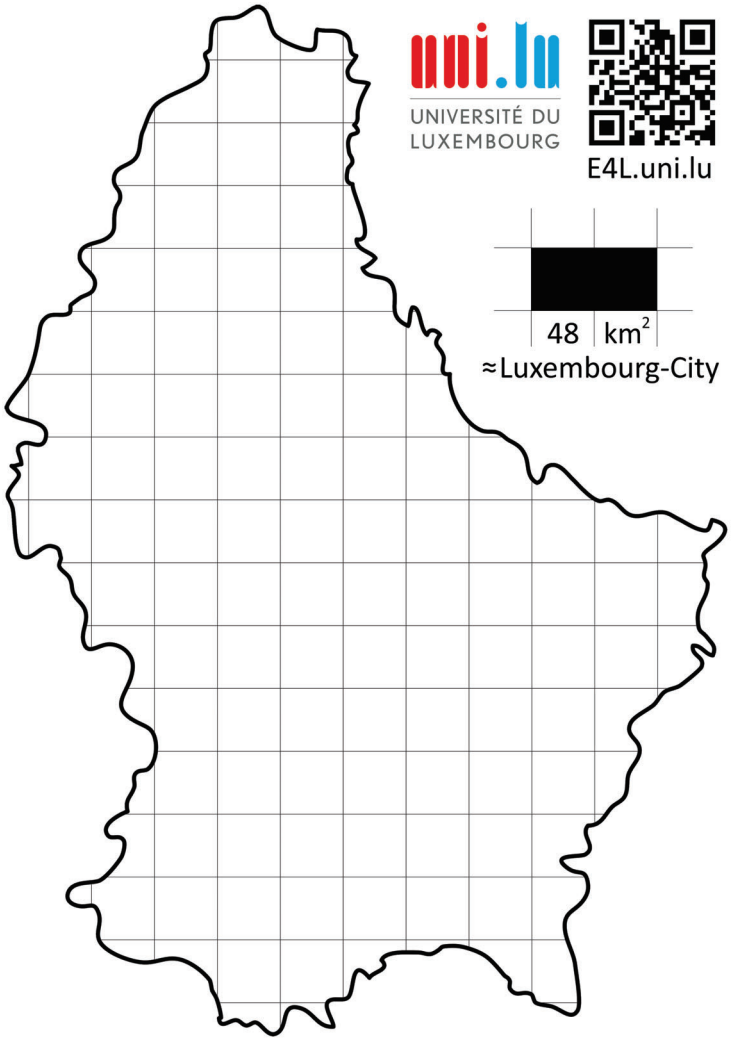

Figure 6.3: Production map for the G.-D. of Luxembourg.

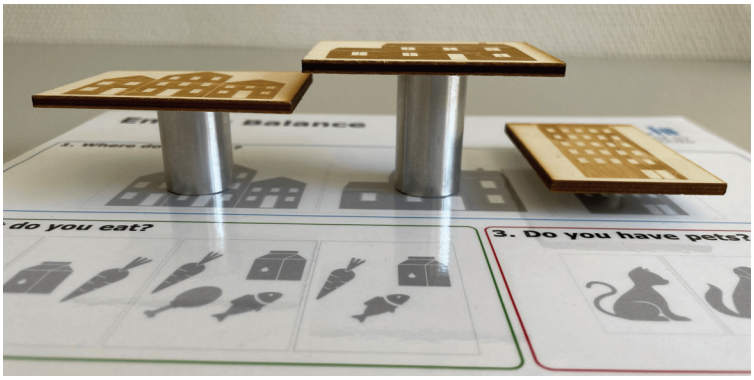

Figure 6.4: Side view of three answer tokens with different areas, heights and weights.

In all cases, the calculations are based on the equations discussed below and only the calculation order changes depending on which constraints are chosen.

To define f_{energy}, one requires to know the energy associated with one unit (of consumption or production) and the mass associated with that unit. An example would be to pick the unit with highest energy requirement and decide on the maximum mass desired for the set of tokens. Alternatively, one can calculate the mass of a unit based on dimensions and material requirements. Taking a production unit as reference, its mass $m^{prod.}_{1\,unit}$ is given by the density of the material $\rho_{material}$, used to fabricate the token's weight, multiplied by its volume $V_{1\,unit}$, as shown in equation 6.4. The weight's volume is given by its cross-section area $A_{1\,unit}$ and height $h_{1\,unit}$.

$$m_{1\,unit} = \rho_{material} \cdot V_{1\,unit} = \rho_{material} \cdot A_{1\,unit} \cdot h_{1\,unit} \tag{6.4}$$

From the previous section, the dimensions of the production map were imposed, which led to the calculated area of one production unit $A_{1\,unit}$. Setting $h_{1\,unit}$ allows to calculate $m_{1\,unit}$, which in turn is used to define f_{energy} (see equation 6.5).

$$f_{energy} = \frac{m_{1\,unit}}{E^{prod.}_{1\,unit}} \tag{6.5}$$

Having determined f_{energy}, the mass of each individual token m_i can be calculated based on the respective yearly energy E_i:

$$m_i = E_i \cdot f_{energy} \tag{6.6}$$

Note that the units of f_{energy} are given by those used for $m_{1\,unit}$ and $E^{prod.}_{1\,unit}$. This means that if a yearly energy is used in equation 6.5, when calculating a mass of a particular token, the input energy E_i must also be a yearly energy. Also, it is worth mentioning that the energies for consumption E_i were scaled to the whole population of the G.-D. of Luxembourg.

Finally, for each token, one can still vary the individual height h_i, area A_i and even the material's density $\rho_{material,\,i}$, if using different materials for the weights. If the individual areas and densities are fixed, then h_i can be calculated as follows:

$$h_i = \frac{m_i}{A_i \cdot \rho_{material,\,i}} \tag{6.7}$$

With this, each token has a calibrated weight, proportional to its energy requirement, and thus can be compared within the set of tokens. This concludes the calculations for the design of the different components.

For completeness, the calculation to determine the required production area ratio $A_{land\%}$, needed to offset the energy consumption is also presented. Note that this is the

answer that the energy balance gives after going through the game. Nevertheless, $A_{land\%}$ can be found with the following equation:

$$A_{land\%} = \frac{\sum_i E_{\mathrm{i}} / E^{prod.}_{density}}{A^{ROI}_{real}} \tag{6.8}$$

Alternatively, one can calculate the number of production units needed $n_{prod.}$:

$$n_{prod.} = \frac{A_{land\,\%} \cdot A^{ROI}_{A3\,sheet}}{A_{1\,unit}} \tag{6.9}$$

This finalizes the description of each of the components of the Energy balance and in the following a brief tutorial on how to run the game is presented.

6.2 How to play the Energy balance game

The game can be divided in three phases. In the first phase, players answer questions by choosing the token(s), that exhibits the answer that best represents their habits, from the Question Sheet and place it on the Answer Sheet. After all questions being covered, the Answer sheet represents energetic footprint of the player.

The second phase consists in placing the answer tokens on the Personal Consumption side of the weighing scale. Then, use the production units (solar modules) on the Renewable Generation side to counterbalance the Personal Consumption.

In the third phase, the player takes the production units that were required to counterbalance his/her consumption, and distributes them on the production map. Since each module fills one square out of the 100 that make up land area of the ROI, one can directly see the equivalent percentage of production land area that would be needed to cover the consumption. In our case, all energies were scaled to the population of the G.-D. of Luxembourg, implying that the area percentage, that is found from the production map, would cover the energetic needs of the whole population, assuming everyone has the same energetic requirement as the player. Thus, to find the equivalent area at an individual level, one has to divide the required area by the population. To have an overview of all the components, Figure 6.5 shows a complete set after a playthrough.

After going through the three phases, the player can change their answers and see what the impact on their energy consumption would be.

6.3 Expanding the game

Multiple directions can be explored to expand or adapt the Energy balance game. In the following, a few suggestions are shortly discussed.

Figure 6.5: Overview of the components of the Energy balance game after a playthrough. The Answer sheet is printed on the back of the Production map.

Climate change being a vast and complex problem, it could be of interest to simply add more possible tokens, both for consumption and production. On the consumption side, distinguishing between electric and combustion cars is of importance given the political discussions on the topic, or as a second example, considering the energetic impact of server-based services, which have energivorous requirements and are consumed without second thoughts. On the production side, one can consider additional renewable sources, like wind and hydroelectric energy, and offer the possibility to choose what combination is most applicable for the situation at hand.

Instead of broadening the choice spectrum, one can subdivide the weights for some of the tokens. This would be particularly pertinent to distinguish the energy consumption of buildings in summer and winter, or to differentiate between car-sharing commuting and a single passenger car commuting. Indeed, in the presented version, the Energy balance game does not consider seasons, but average energies over a year. This avoids the discussion of energy management and energy storage throughout the year. Subdividing the weights allows to change the energy of the tokens (using magnets or attachments) and opens up a winter or summer mode for the tokens. This allows to follow more realistically the consumption and production in a year. Making the production units also modular to summer and winter, opens up the discussion about batteries, which would store the excess of produced energy in summer. These also require land area, in the production map, and would be included in the consumption side during summer and in the production side during winter.

Finally, the parameter chosen for comparison is the energy, however one could also

discuss in terms of CO_2 emissions, given that the majority of the energy is currently generated by burning fossil fuels. In this context, the production side would need to be adapted to represent the impact the renewable production units would have in reducing the CO_2 emissions.

6.4 Summary

To conclude, this chapter addresses the educational gap that exists between entities with diverse background knowledge and suggests a method to design and materialize a pedagogical tool to allow pertinent discussions on the basis of a common denominator, in this case, energy consumption and production for the topic of climate change. A description of the Energy balance game and the details of the respective design calculations are presented, while highlighting the constraints and the possibilities to reproduce the same game with different materials and dimensions. Indeed, the Energy balance game, presented here, allows to easily identify the distribution of energy consumption and meaningfully quantify the abstract concept of energy into PV equivalent land area. It converts a lifestyle into a land use without visible calculations, which hopefully everyone can understand. This provides a common scale to discuss the problem of CO_2 emissions and directly determine and assess the impact of hypothetical measures to be applied.

Chapter 7

Summary and outlook

The objectives of this thesis were (i) to investigate the synthesis of CIGSe on silicon oxide (SiO_2) patterned substrates using material efficient methods, in order to improve the resulting PCE of the respective micro solar cells and (ii) to develop a pedagogical tool to help popularizing scientific topics, in this case energy consumption and provision.

To address the first objective, three distinct steps were followed and are summarized in the following. First, given the high number of individual micro solar cells on each substrate and the multiple steps involved in the synthesis processes, a new methodology, based on CLSM, was developed to characterize the individual micro structures, in order to monitor each step of the synthesis process and perform statistical analysis. More precisely, CLSM was demonstrated to effectively measure the thickness of individual layers, their roughness and assess the evolution of the layers' morphology, for each step in the synthesis process. A detailed analysis both at the individual micro-dot level, as well as, at the array level allowed to identify a thickness gradient during one of the electrodeposition steps. Beyond the usual capacities associated with CLSM, a new methodology to measure relative composition in sequential processes, based on the CLSM morphology maps, was proposed and verified with EDX. Furthermore, combining the composition information with the material's phase diagram, spatial predictions were made of which phases would form at the end of the synthesis process. This demonstrated the impact the initial precursor's morphology has on the final absorber's spatial composition, and consequently on the formed phases. Lastly, examples of how optical microscopy can be used to quickly differentiate phases in a material were discussed. In short, CLSM was shown to be a versatile characterization and diagnosis tool to confirm the good progression of the multi-step synthesis or to rapidly pinpoint possible issues, allowing to intervene at an early stage.

Second, to assess the influence that using a patterned substrate, designed for micro solar cells, has on the synthesis of CIGSe, a reference co-evaporation technique was used to grow CIGSe on patterned substrates and on conventional, unpatterned, substrates. It was found that due to the geometry of the patterned substrate and to the diffusion blocking property of the SiO_2 patterned layer, a locally enhanced diffusion of Na takes place, from the soda lime glass and through the holes in the SiO_2 layer. This interferes with

the growth of the CIGSe absorber, leading to a poor adhesion of the CIGSe layer to the Mo back contact and to the formation of a Na-enriched secondary phase (suggested here to be $Na(In,Ga)_3Se_5$). Both consequences compromise the absorber's final performance, compared to the reference. Three mitigation strategies were tested, in order to reduce the enhanced flux of Na from the patterned substrate, and the implementation of a Na barrier was proven to be the most effective. Nevertheless, with this method, providing some Na externally is essential to ensure CIGSe adhesion. Furthermore, by comparing two annealing routines with widely distinct Se partial pressures, it was demonstrated that the Se partial pressure regulates the Na diffusion from the patterned substrate, and it also influences the morphology and phase formation of the resulting absorber.

Third, with the characterization methodology developed and the knowledge on how to avoid the enhanced Na diffusion from the patterned substrates, two material efficient methods were investigated with the aim of growing CIGSe based micro solar cells. Both are two-step processes (precursor deposition followed by annealing in Se), where the precursor layer is either sputtered or electrodeposited. For each method, both Cu-rich and Cu-poor CIGSe compositions were synthesized. In both cases, the implementation of a Na barrier in the substrate stack is essential. This is the case, given that both synthesis methods require a relatively high Se partial pressure to obtain better absorber properties, and that a higher Se partial pressure enhances the diffusion of Na from the substrate. In fact, the Se partial pressure was shown to influence the morphology, phase purity and optoelectronic properties of the resulting CIGSe absorbers, highlighting the need for a fine control during the annealing in Se. Additionally, the morphology of the metal precursors must also be optimized in both synthesis methods to avoid phase inhomogeneities.

It was observed that the sputtering and annealing method suffers from a contamination issue, occurring during the deposition of the precursor, which was partly addressed by adjusting the design of the substrate pattern. Working micro solar cells were achieved with both material efficient methods, with the champion device having a power conversion efficiency (PCE) of 5.2 % under 1 Sun. Although the gap to top down approaches was indeed reduced, there are multiple directions that can be explored to further develop material efficient methods. A first suggestion is the optimization of the precursor's composition, which for state-of-the-art CIGSe solar cells translates to a CGI in the range 0.8-0.95 [29, 192]. This should already improve the CIGSe phase purity and lead to a higher open-circuit voltage (V_{OC}) independently of the micro-dots diameter. During the annealing in Se, one could additionally introduce alkali salts (like NaCl, RbF, etc) in order to dope the CIGSe absorber directly during its formation, which is expected to improve its V_{OC} without adding an extra synthesis step. Similarly, Na post-deposition treatment was demonstrated, in this work, to improve the absorber's quasi-Fermi level splitting by 40 meV, without particular process optimization. This suggests that micro absorbers can benefit from the potential gains of Na and heavier alkali post-deposition treatments (like Rb) that are reported in literature for planar CIGSe absorber [108, 193]. In the context of resource optimization, it would be interesting to replace the annealing strategy used in

this work with laser annealing. Indeed, most of the heat generated during the annealing in the tube oven is used to heat up the graphite box and the sodalime glass, which makes up most the sample's volume. Since only the absorbers require high temperatures, laser annealing is an adequate annealing technique given its high localized energy input.

Finally, with the aim of bridging the knowledge gap between experts and regular citizens on abstract concepts, a pedagogical tool was presented to allow pertinent discussions on the topic of energy production and consumption. A description of the Energy balance game and the details of the respective design calculations are presented, while highlighting the constraints and the possibilities to reproduce the same game with different materials and dimensions. Indeed, the Energy balance game, presented here, allows to easily identify the distribution of energy consumption and meaningfully quantify the abstract concept of energy into PV equivalent land area.

List of Publications

[1] **R. G. Poeira** et al. "Direct fabrication of arrays of Cu(In,Ga)Se_2 micro solar cells by sputtering for micro-concentrator photovoltaics". In: *Materials & Design* (2023). DOI: 10.1016/j.matdes.2023.111597.

[2] **R. G. Poeira** et al. "Optical Measurement of the Stoichiometry of Thin-Film Compounds Synthetized From Multilayers : Example of Cu(In,Ga)Se_2". In: *Microscopy and Microanalysis* (2023). DOI: 10.1093/micmic/ozad105.

[3] A. Pérez-Rodríguez, **R. G. Poeira** et al. "Current status of bottom-up fabrication approaches for Cu(In,Ga)Se_2 micro-concentrator solar cells". In: *AIP Conference Proceedings*, 2022. DOI: 10.1063/5.0104440.

[4] P. Santos, P. Anacleto, D. Brito, S. Shital, **R. G. Poeira** et al. "Fabrication of semi-transparent Cu(In,Ga)Se_2 solar cells aided by Bromine etching". In: *Thin Solid Films* (2023). DOI: 10.1016/j.tsf.2023.139778.

[5] A. JC. M. Prot, M. Melchiorre, T. Schaaf, **R. G. Poeira** et al. "Improved sequentially processed Cu(In,Ga)$(S,Se)_2$ by Ag alloying". In: *Sol. RRL.* (2024). DOI: 10.1002/solr.202400208.

[6] O. Ramírez, E. M. Lanzoni, **R. G. Poeira** et al. "How much gallium do we need for a p-type Cu(In,Ga)Se_2?". In: *APL Mater*. (June 2022). DOI: 10.1063/5.00916765.

[7] T. Wang, L. Song, S. Gharabeiki, M. Sood, A. JC. M. Prot, **R. G. Poeira** et al. "Shifting the paradigm: a functional hole selective transport layer for chalcopyrite solar cells". In: *Sol. RRL*. (2024). DOI: 10.1002/solr.202400212.

Bibliography

[1] Hannah Ritchie and Pablo Rosado. "Energy Mix". URL: https://ourworldindata.org/energy-mix. *Our World in Data. Accessed on 07-03-2024*.

[2] Gavin A. Schmidt et al. "Attribution of the present-day total greenhouse effect". In: *Journal of Geophysical Research: Atmospheres* 115.D20 (Oct. 2010), pp. 1–6. ISSN: 0148-0227. DOI: 10.1029/2010JD014287 (cit. on p. 15).

[3] V. Ramanathan and Anand Inamdar. "The radiative forcing due to clouds and water vapor". In: *Frontiers of Climate Modeling*. Vol. 9780521791. Cambridge University Press, Aug. 2006, pp. 119–151. ISBN: 9780511535857. DOI: 10.1017/CBO9780511535857.006 (cit. on p. 15).

[4] Michael Ghil and Valerio Lucarini. "The physics of climate variability and climate change". In: *Reviews of Modern Physics* 92.3 (July 2020), p. 035002. ISSN: 0034-6861. DOI: 10.1103/RevModPhys.92.035002 (cit. on p. 15).

[5] Wenyi Zhong and Joanna D. Haigh. "The greenhouse effect and carbon dioxide". In: *Weather* 68.4 (Apr. 2013), pp. 100–105. ISSN: 0043-1656. DOI: 10.1002/wea.2072 (cit. on p. 15).

[6] UNFCCC. *United Nations Framework Convention on Climate Change*. Tech. rep. 1992, pp. 1–33. URL: https://unfccc.int/files/essential_background/background_publications_htmlpdf/application/pdf/conveng.pdf (cit. on p. 15).

[7] Rebecca Lindsey. "Climate Change: Atmospheric Carbon Dioxide". URL: https://www.climate.gov/news-features/understanding-climate/climate-change-atmospheric-carbon-dioxide. *Climate.gov. Accessed on 07-03-2024*.

[8] Rebecca Lindsey and Luann Dahlman. "Climate Change: Global Temperature". URL: https://www.climate.gov/news-features/understanding-climate/climate-change-global-temperature. *Climate.gov. Accessed on 07-03-2024*.

[9] UNFCCC. *Paris Agreement to the United Nations Framework Convention on Climate Change*. Tech. rep. 2015. URL: https://unfccc.int/sites/default/files/resource/parisagreement_publication.pdf (cit. on p. 15).

[10] WMO. "WMO confirms that 2023 smashes global temperature record". URL: https://wmo.int/news/media-centre/wmo-confirms-2023-smashes-global-temperature-record. *Press release. Accessed on 30-04-2024*.

[11] Scott Nicholson and Garvin Heath. *Life Cycle Greenhouse Gas Emissions from Electricity Generation: Update*. Tech. rep. NREL, 2021, pp. 1–4. URL: https://www.nrel.gov/docs/fy21osti/80580.pdf (cit. on p. 16).

[12] Y-m Wei et al. *Climate Change 2022: Mitigation of Climate Change - Energy Systems*. Tech. rep. 2022. Chap. 6, pp. 613–746. URL: https://www.ipcc.ch/report/ar6/wg3/downloads/report/IPCC_AR6_WGIII_Chapter06.pdf (cit. on p. 16).

[13] IEA. "Massive expansion of renewable power opens door to achieving global tripling goal set at COP28". URL: https://www.iea.org/news/massive-expansion-of-renewable-power-opens-door-to-achieving-global-tripling-goal-set-at-cop28. *Press release. Accessed on 01-05-2024*.

[14] IPCC. *Climate Change 2022 - Mitigation of Climate Change - Full Report*. 1. 2022, pp. 1–30. ISBN: 9781107415416 (cit. on p. 16).

[15] Fraunhofer Institute for Solar Energy Systems. "Fraunhofer ISE develops the world's most efficient solar cell with 47.6 percent efficiency". URL: https://www.ise.fraunhofer.de/en/press-media/press-releases/2022/fraunhofer-ise-develops-the-worlds-most-efficient-solar-cell-with-47-comma-6-percent-efficiency.html. *Press release. Accessed on 19-02-2024*.

[16] Hao Lin et al. "Silicon heterojunction solar cells with up to 26.81% efficiency achieved by electrically optimized nanocrystalline-silicon hole contact layers". In: *Nature Energy* 8.8 (May 2023), pp. 789–799. ISSN: 2058-7546. DOI: 10.1038/s41560-023-01255-2 (cit. on p. 17).

[17] Marina Alves et al. "Thin-film micro-concentrator solar cells". In: *Journal of Physics: Energy* 2.1 (Nov. 2019), p. 012001. ISSN: 2515-7655. DOI: 10.1088/2515-7655/ab4289 (cit. on pp. 17, 19, 44).

[18] Giles E. Eperon et al. "Formamidinium lead trihalide: A broadly tunable perovskite for efficient planar heterojunction solar cells". In: *Energy and Environmental Science* 7.3 (2014), pp. 982–988. ISSN: 17545692. DOI: 10.1039/c3ee43822h (cit. on p. 18).

[19] P. T. Landsberg and P. Baruch. "The thermodynamics of the conversion of radiation energy for photovoltaics". In: *Journal of Physics A: Mathematical and General* 22.11 (June 1989), pp. 1911–1926. ISSN: 0305-4470. DOI: 10.1088/0305-4470/22/11/028 (cit. on p. 18).

[20] Marcus Chuang. "Shockley Queisser limit: Theoretical Solar Cell Efficiencies calculator and visualizer". URL: https://github.com/marcus-cmc/Shockley-Queisser-limit. *Github. Accessed on 14-04-2022*.

[21] William Shockley and Hans J. Queisser. "Detailed Balance Limit of Efficiency of p-n Junction Solar Cells". In: *Journal of Applied Physics* 32.3 (Mar. 1961), pp. 510–519. ISSN: 0021-8979. DOI: 10.1063/1.1736034 (cit. on p. 18).

[22] Myriam Paire. "Highly efficient solar cells in low dimensionality based on Cu(In,Ga)Se2 chalcopyrite materials". PhD thesis. Sorbonne Universités, UPMC, 2016. URL: https://hal.science/tel-01393784 (cit. on pp. 17, 18, 44).

[23] J. R. Tuttle et al. "The Performance of Cu(In, Ga)Se2-Based Solar Cells in Conventional and Concentrator Applications". In: *MRS Proceedings* 426.January (Feb. 1996), p. 143. ISSN: 0272-9172. DOI: 10.1557/PROC-426-143 (cit. on p. 18).

[24] Myriam Paire et al. "Physics of Cu(In, Ga)Se2 solar cells in high injection regime". In: *2011 37th IEEE Photovoltaic Specialists Conference*. IEEE, June 2011, pp. 000140–000143. ISBN: 978-1-4244-9965-6. DOI: 10.1109/PVSC.2011.6185863 (cit. on pp. 18, 19, 44).

[25] Sascha Sadewasser. "Geometry and materials considerations for thin film micro-concentrator solar cells". In: *Solar Energy* 158 (Dec. 2017), pp. 186–191. ISSN: 0038092X. DOI: 10.1016/j.solener.2017.09.035 (cit. on p. 18).

[26] Myriam Paire et al. "Thin film microcells for concentrated applications". In: *2013 IEEE 39th Photovoltaic Specialists Conference (PVSC)*. IEEE, June 2013, pp. 2118–2122. ISBN: 978-1-4799-3299-3. DOI: 10.1109/PVSC.2013.6744892 (cit. on p. 19).

[27] Pierre Albert et al. "Miniaturization of InGaP/InGaAs/Ge solar cells for micro-concentrator photovoltaics". In: *Progress in Photovoltaics: Research and Applications* 29.9 (2021), pp. 990–999. ISSN: 1099159X. DOI: 10.1002/pip.3421 (cit. on p. 19).

[28] Myriam Paire et al. "Cu(In, Ga)Se2 microcells: High efficiency and low material consumption". In: *Journal of Renewable and Sustainable Energy* 5.1 (2013), pp. 1–6. ISSN: 19417012. DOI: 10.1063/1.4791778 (cit. on p. 19).

[29] Jan Keller et al. "High-concentration silver alloying and steep back-contact gallium grading enabling copper indium gallium selenide solar cell with 23.6% efficiency". In: *Nature Energy* (Feb. 2024). ISSN: 2058-7546. DOI: 10.1038/s41560-024-01472-3 (cit. on pp. 19, 67, 127, 156).

[30] A. Duchatelet et al. "Self-aligned growth of thin film Cu(In,Ga)Se2 solar cells on various micropatterns". In: *Applied Physics Letters* 109.25 (Dec. 2016), p. 253901. ISSN: 0003-6951. DOI: 10.1063/1.4971975 (cit. on p. 19).

[31] Sascha Sadewasser, Pedro M.P. Salomé, and Humberto Rodriguez-Alvarez. "Materials efficient deposition and heat management of CuInSe2 micro-concentrator

solar cells". In: *Solar Energy Materials and Solar Cells* 159.October 2016 (Jan. 2017), pp. 496–502. ISSN: 09270248. DOI: 10.1016/j.solmat.2016.09.041 (cit. on pp. 19, 24).

[32] F. Ringleb et al. "Regularly arranged indium islands on glass/molybdenum substrates upon femtosecond laser and physical vapor deposition processing". In: *Applied Physics Letters* 108.11 (Mar. 2016), p. 111904. ISSN: 0003-6951. DOI: 10.1063/1.4943794 (cit. on p. 19).

[33] Berit Heidmann et al. "Local growth of CuInSe 2 micro solar cells for concentrator application". In: *Materials Today Energy* 6 (Dec. 2017), pp. 238–247. ISSN: 24686069. DOI: 10.1016/j.mtener.2017.10.010 (cit. on p. 19).

[34] Martina Schmid et al. "Locally grown Cu(In,Ga)Se2 micro islands for concentrator solar cells". In: *Physics, Simulation, and Photonic Engineering of Photovoltaic Devices VII*. Ed. by Alexandre Freundlich, Masakazu Sugiyama, and Laurent Lombez. Vol. 10527. SPIE, Feb. 2018, p. 7. ISBN: 9781510615397. DOI: 10.1117/12.2288253 (cit. on p. 19).

[35] Ana Pérez-Rodríguez et al. "Current status of bottom-up fabrication approaches for Cu(In,Ga)Se2 micro-concentrator solar cells". In: *AIP Conference Proceedings*. Vol. 2550. September. 2022, p. 060005. ISBN: 9780735443921. DOI: 10.1063/5.0104440 (cit. on p. 19).

[36] Daniel Siopa et al. "Micro-sized thin-film solar cells via area-selective electrochemical deposition for concentrator photovoltaics application". In: *Scientific Reports* 10.1 (Dec. 2020), p. 14763. ISSN: 2045-2322. DOI: 10.1038/s41598-020-71717-0 (cit. on pp. 19, 26, 52).

[37] M.I. Alonso et al. "Optical functions of chalcopyrite CuGaxIn1-xSe2 alloys". In: *Applied Physics A: Materials Science & Processing* 74.5 (May 2002), pp. 659–664. ISSN: 0947-8396. DOI: 10.1007/s003390100931 (cit. on p. 20).

[38] F. B. Dejene and V. Alberts. "Structural and optical properties of homogeneous Cu(In,Ga)Se2 thin films prepared by thermal reaction of InSe/Cu/GaSe alloys with elemental Se vapour". In: *Journal of Physics D: Applied Physics* 38.1 (Jan. 2005), pp. 22–25. ISSN: 0022-3727. DOI: 10.1088/0022-3727/38/1/005 (cit. on p. 20).

[39] Jae-Cheol Park et al. "Bandgap engineering of Cu(In_1-xGa_x)Se_2 absorber layers fabricated using CuInSe_2 and CuGaSe_2 targets for one-step sputtering process". In: *Optical Materials Express* 6.11 (Nov. 2016), p. 3541. ISSN: 2159-3930. DOI: 10.1364/OME.6.003541 (cit. on pp. 20, 128).

[40] Jeyakumar Ramanujam and Udai P. Singh. "Copper indium gallium selenide based solar cells – a review". In: *Energy & Environmental Science* 10.6 (2017), pp. 1306–1319. ISSN: 1754-5692. DOI: 10.1039/C7EE00826K (cit. on p. 20).

[41] E. Romero et al. "Phase identification and AES depth profile analysis of Cu(In,Ga)Se2 thin films". In: *Brazilian Journal of Physics* 36.3b (Sept. 2006), pp. 1050–1053. ISSN: 0103-9733. DOI: 10.1590/S0103-97332006000600067 (cit. on p. 20).

[42] Maxim Guc et al. "Evaluation of defect formation in chalcopyrite compounds under Cu-poor conditions by advanced structural and vibrational analyses". In: *Acta Materialia* 223 (Jan. 2022), p. 117507. ISSN: 13596454. DOI: 10.1016/j.actamat.2021.117507 (cit. on pp. 20, 21).

[43] Tilo Gödecke, Thomas Haalboom, and Frank Ernst. "Phase Equilibria of Cu-In-Se I. Stable States and Nonequilibrium States of the In2Se3-Cu2Se Subsystem". In: *International Journal of Materials Research* 91.8 (Aug. 2000), pp. 622–634. ISSN: 2195-8556. DOI: 10.1515/ijmr-2000-910802 (cit. on p. 20).

[44] Susanne Siebentritt et al. "Why do we make Cu(In,Ga)Se2 solar cells non-stoichiometric?" In: *Solar Energy Materials and Solar Cells* 119 (Dec. 2013), pp. 18–25. ISSN: 09270248. DOI: 10.1016/j.solmat.2013.04.014 (cit. on pp. 20, 91, 92, 116).

[45] C.H. Chang et al. "Thermodynamic assessment of the Cu-In-Se system and application to thin film photovoltaics". In: *Conference Record of the Twenty Fifth IEEE Photovoltaic Specialists Conference - 1996*. IEEE, 1996, pp. 849–852. ISBN: 0-7803-3166-4. DOI: 10.1109/PVSC.1996.564261 (cit. on p. 21).

[46] F. Hergert et al. "A crystallographic description of experimentally identified formation reactions of Cu(In,Ga)Se2". In: *Journal of Solid State Chemistry* 179.8 (Aug. 2006), pp. 2394–2415. ISSN: 00224596. DOI: 10.1016/j.jssc.2006.04.033 (cit. on p. 20).

[47] Peter Würfel and Uli Würfel. *Physics of Solar Cells*. 3rd ed. Vol. 6. August. Wiley, Jan. 2005, p. 128. ISBN: 9783527404285. DOI: 10.1002/9783527618545 (cit. on pp. 21, 40, 42, 43).

[48] Antonio Luque and Steven Hegedus, eds. *Handbook of Photovoltaic Science and Engineering*. 2nd editio. Wiley, Dec. 2010. ISBN: 9780470721698. DOI: 10.1002/9780470974704 (cit. on p. 21).

[49] Dominik Matthias Berg. "Kesterite Equilibrium Reaction and the Discrimination of Secondary Phases from Cu2ZnSnS4". PhD thesis. University of Luxembourg, 2012, p. 187. URL: http://hdl.handle.net/10993/15414 (cit. on p. 26).

[50] A. C. Fisher. *Electrode Dynamics*. Illustrate. Oxford University Press, 1996, p. 84. ISBN: 9780198556909 (cit. on p. 26).

[51] Yuliy D. Gamburg and Giovanni Zangari. *Theory and Practice of Metal Electrodeposition*. Vol. 35. 8. New York, NY: Springer New York, 2011, pp. 1–25. ISBN: 978-1-4419-9668-8. DOI: 10.1007/978-1-4419-9669-5 (cit. on p. 26).

[52] David Fuster et al. "System for manufacturing complete Cu(In,Ga)Se2 solar cells in situ under vacuum". In: *Solar Energy* 198.January (Mar. 2020), pp. 490–498. ISSN: 0038092X. DOI: 10.1016/j.solener.2020.01.073 (cit. on pp. 26, 27).

[53] Rainer Behrisch. *Sputtering by Particle Bombardment I*. Ed. by Rainer Behrisch. Vol. 47. Topics in Applied Physics. Berlin, Heidelberg: Springer Berlin Heidelberg, June 1981, p. 284. ISBN: 978-3-540-10521-3. DOI: 10.1007/3-540-10521-2 (cit. on p. 26).

[54] S. Swann. "Magnetron sputtering". In: *Physics in Technology* 19.2 (Mar. 1988), pp. 67–75. ISSN: 0305-4624. DOI: 10.1088/0305-4624/19/2/304 (cit. on p. 26).

[55] Jeong Hyeob Han et al. "Actual partial pressure of Se vapor in a closed selenization system: quantitative estimation and impact on solution-processed chalcogenide thin-film solar cells". In: *Journal of Materials Chemistry A* 4.17 (2016), pp. 6319–6331. ISSN: 2050-7488. DOI: 10.1039/C6TA00145A (cit. on pp. 28, 121, 126).

[56] Taowen Wang. "Comprehending and mitigating backside recombination in Cu(In,Ga)Se2 solar cells". PhD thesis. University of Luxembourg, 2023, p. 213. URL: https://hdl.handle.net/10993/57142 (cit. on pp. 28, 68, 121).

[57] Sebastian Schleussner et al. "Effect of gallium grading in Cu(In,Ga)Se2 solar-cell absorbers produced by multi-stage coevaporation". In: *Solar Energy Materials and Solar Cells* 95.2 (Feb. 2011), pp. 721–726. ISSN: 09270248. DOI: 10.1016/j.solmat.2010.10.011 (cit. on pp. 28, 67).

[58] Mohit Sood et al. "Absorber composition: A critical parameter for the effectiveness of heat treatments in chalcopyrite solar cells". In: *Progress in Photovoltaics: Research and Applications* 28.10 (Oct. 2020), pp. 1063–1076. ISSN: 1062-7995. DOI: 10.1002/pip.3314 (cit. on p. 29).

[59] Amicia D. Elliott. "Confocal Microscopy: Principles and Modern Practices". In: *Current Protocols in Cytometry* 92.1 (Mar. 2020), pp. 139–148. ISSN: 1934-9297. DOI: 10.1002/cpcy.68 (cit. on p. 30).

[60] Weichang Xie. "Transfer characteristics of white light interferometers and confocal microscopes". PhD thesis. University of Kassel, 2017, p. 275. URL: http://files/336/WeichangXie_Dissertation.pdf (cit. on p. 30).

[61] David J. Whitehouse. *Handbook of Surface and Nanometrology*. Vol. 3. 1. CRC Press, Dec. 2010, pp. 10–27. ISBN: 9780429140693. DOI: 10.1201/b10415 (cit. on p. 32).

[62] Peter Eaton and Paul West. "AFM modes". In: *Atomic Force Microscopy*. Oxford University Press, Mar. 2010, pp. 49–81. ISBN: 9780199570454. DOI: 10.1093/acprof:oso/9780199570454.001 (cit. on pp. 33, 49).

[63] Joseph I. Goldstein et al. *Scanning Electron Microscopy and X-Ray Microanalysis*. Ed. by Springer. 4th ed. Vol. 24. New York, NY: Springer New York, Dec. 2018, p. 550. ISBN: 978-1-4939-6674-5. DOI: 10.1007/978-1-4939-6676-9 (cit. on pp. 34–36).

[64] Albert C. Thompson et al. *X-Ray Data Booklet*. 3rd. Berkeley: University of California, Sept. 2009, p. 176. URL: https://xdb.lbl.gov (cit. on pp. 35, 71).

[65] Ewen Smith and Geoffrey Dent. *Modern Raman Spectroscopy – A Practical Approach*. Wiley, Dec. 2004, pp. 101–117. ISBN: 9780471496687. DOI: 10.1002/0470011831 (cit. on p. 37).

[66] Ian R. Lewis and Howell Edwards. *Handbook of Raman Spectroscopy*. CRC Press, Aug. 2001, p. 26. ISBN: 9781420029253. DOI: 10.1201/9781420029253 (cit. on p. 37).

[67] Jacobo Álvarez-García et al. "Raman Spectroscopy on Thin Films for Solar Cells". In: *Advanced Characterization Techniques for Thin Film Solar Cells*. Vol. 2-2. Wiley, Sept. 2016, pp. 469–499. ISBN: 9783527699025. DOI: 10.1002/9783527699025.ch17 (cit. on p. 37).

[68] Sven Rühle. "Tabulated values of the Shockley–Queisser limit for single junction solar cells". In: *Solar Energy* 130 (June 2016), pp. 139–147. ISSN: 0038092X. DOI: 10.1016/j.solener.2016.02.015 (cit. on p. 39).

[69] Susanne Siebentritt et al. "How photoluminescence can predict the efficiency of solar cells". In: *Journal of Physics: Materials* 4.4 (Oct. 2021), p. 042010. ISSN: 2515-7639. DOI: 10.1088/2515-7639/ac266e (cit. on p. 40).

[70] Daniel Abou-Ras, Thomas Kirchartz, and Uwe Rau. *Advanced Characterization Techniques for Thin Film Solar Cells: Second Edition*. Vol. 1-2. 2016, pp. 1–681. ISBN: 9783527699025. DOI: 10.1002/9783527699025 (cit. on pp. 40, 42, 43).

[71] Max Hilaire Wolter. "Optical investigation of voltage losses in high-efficiency Cu(In,Ga)Se2 thin-film solar cells". PhD thesis. University of Luxembourg, 2019, p. 253. URL: http://hdl.handle.net/10993/39611 (cit. on p. 40).

[72] Susanne Siebentritt. "What limits the efficiency of chalcopyrite solar cells?" In: *Solar Energy Materials and Solar Cells* 95.6 (June 2011), pp. 1471–1476. ISSN: 09270248. DOI: 10.1016/j.solmat.2010.12.014 (cit. on pp. 41, 42).

[73] A. S. Najm et al. "An in-depth analysis of nucleation and growth mechanism of CdS thin film synthesized by chemical bath deposition (CBD) technique". In: *Scientific Reports* 12.1 (Sept. 2022), p. 15295. ISSN: 2045-2322. DOI: 10.1038/s41598-022-19340-z (cit. on p. 41).

[74] Steven S. Hegedus and William N. Shafarman. "Thin-film solar cells: device measurements and analysis". In: *Progress in Photovoltaics: Research and Applications* 12.2-3 (Mar. 2004), pp. 155–176. ISSN: 1062-7995. DOI: 10.1002/pip.518 (cit. on pp. 42, 92).

[75] Jean-Francois Guillemoles et al. "Guide for the perplexed to the Shockley–Queisser model for solar cells". In: *Nature Photonics* 13.8 (Aug. 2019), pp. 501–505. ISSN: 1749-4885. DOI: 10.1038/s41566-019-0479-2 (cit. on p. 43).

[76] Myriam Paire et al. "Toward microscale Cu(In,Ga)Se2 solar cells for efficient conversion and optimized material usage: Theoretical evaluation". In: *Journal of Applied Physics* 108.3 (Aug. 2010), p. 034907. ISSN: 0021-8979. DOI: 10.1063/1.3460629 (cit. on p. 44).

[77] Myriam Paire et al. "Microscale solar cells for high concentration on polycrystalline Cu(In,Ga)Se2 thin films". In: *Applied Physics Letters* 98.26 (June 2011), p. 264102. ISSN: 0003-6951. DOI: 10.1063/1.3604789 (cit. on p. 44).

[78] Carlos Algora and Ignacio Rey-Stolle. *Handbook of Concentrator Photovoltaic Technology*. Ed. by Carlos Algora and Ignacio Rey-Stolle. Wiley, Apr. 2016. ISBN: 9781118472965. DOI: 10.1002/9781118755655 (cit. on p. 44).

[79] Seong-Uk Jun et al. "Surface Texturing and Anti-Reflection Coating of Multicrystalline Silicon Solar Cell". In: *Journal of the Korean institute of surface engineering* 40.3 (June 2007), pp. 138–143. ISSN: 1225-8024. DOI: 10.5695/JKISE.2007.40.3.138 (cit. on p. 47).

[80] Anil Kurella and Narendra B. Dahotre. "Review paper: Surface Modification for Bioimplants: The Role of Laser Surface Engineering". In: *Journal of Biomaterials Applications* 20.1 (July 2005), pp. 5–50. ISSN: 0885-3282. DOI: 10.1177/0885328205052974 (cit. on p. 47).

[81] Cheng Yang, Ching Ping Wong, and Matthew M. F. Yuen. "Printed electrically conductive composites: conductive filler designs and surface engineering". In: *Journal of Materials Chemistry C* 1.26 (2013), p. 4052. ISSN: 2050-7526. DOI: 10.1039/c3tc00572k (cit. on p. 47).

[82] Dr Kalliopi K. Aligizaki. "Surface Engineering for Corrosion and Wear Resistance". In: *Anti-Corrosion Methods and Materials* 51.1 (Feb. 2004). ISSN: 0003-5599. DOI: 10.1108/acmm.2004.12851aae.001 (cit. on p. 47).

[83] Mike Conroy and Joe Armstrong. "A comparison of surface metrology techniques". In: *Journal of Physics: Conference Series* 13 (Jan. 2005), pp. 458–465. ISSN: 1742-6588. DOI: 10.1088/1742-6596/13/1/106 (cit. on p. 47).

[84] L Brown and Liam Blunt. "Surface Metrology for the Automotive Industry". In: *Inaugural Automotive Researchers' Conference*. January. University of Huddersfield,

2008. URL: http://eprints.hud.ac.uk/id/eprint/4059/1/08AARC2008.pdf (cit. on p. 48).

[85] Margaret Stedman. "Mapping The Performance Of Surface-Measuring Instruments". In: ed. by Manfred Weck. Vol. d. 2. Jan. 1987, p. 138. DOI: 10.1117/12.941285 (cit. on p. 48).

[86] Hemraj M. Yadav and Jung-Sik Kim. "Fabrication of SiO2/TiO2 double layer thin films with self-cleaning and photocatalytic properties". In: *Journal of Materials Science: Materials in Electronics* 27.10 (Oct. 2016), pp. 10082–10088. ISSN: 0957-4522. DOI: 10.1007/s10854-016-5082-4 (cit. on pp. 49, 51).

[87] Ricardo G Poeira et al. "Optical Measurement of the Stoichiometry of Thin-Film Compounds Synthetized From Multilayers : Example of Cu(In,Ga)Se2". In: *Microscopy and Microanalysis* (2023). DOI: https://doi.org/10.1093/micmic/ozad105 (cit. on p. 51).

[88] Jinlian Bi et al. "Pulse electro-deposition of copper on molybdenum for Cu(In,Ga)Se2 and Cu2ZnSnSe4 solar cell applications". In: *Journal of Power Sources* 326 (2016), pp. 211–219. ISSN: 03787753. DOI: 10.1016/j.jpowsour.2016.07.005 (cit. on p. 52).

[89] Ridha Hamdi et al. "Electrodeposition Study of Silver: Nucleation Process and Theoretical Analysis". In: *Journal of Electronic Materials* 50.10 (2021), pp. 5507–5513. ISSN: 1543186X. DOI: 10.1007/s11664-021-09055-8 (cit. on p. 52).

[90] João C. Malaquias et al. "Tuning the gallium content of metal precursors for Cu(In,Ga)Se2 thin film solar cells by electrodeposition from a deep eutectic solvent". In: *Physical Chemistry Chemical Physics* 16.6 (2014), p. 2561. ISSN: 1463-9076. DOI: 10.1039/c3cp54509a (cit. on pp. 52, 54, 55, 58).

[91] Y. F. Lin et al. "Phase stabilities and interfacial reactions of the Cu–In binary systems". In: *Journal of Materials Science: Materials in Electronics* 31.13 (July 2020), pp. 10161–10169. ISSN: 0957-4522. DOI: 10.1007/s10854-020-03561-x (cit. on pp. 53, 57).

[92] W. M. Haynes. *CRC Handbook of Chemistry and Physics*. Ed. by W. M. Haynes, David R. Lide, and Thomas J. Bruno. 97th ed. Boca Raton: CRC Press, June 2016. ISBN: 9781315380476. DOI: 10.1201/9781315380476 (cit. on p. 56).

[93] H.-J. Fitting et al. "Electron beam excitation in thin layered samples". In: *Journal of Electron Spectroscopy and Related Phenomena* 159.1-3 (June 2007), pp. 46–52. ISSN: 03682048. DOI: 10.1016/j.elspec.2007.03.014 (cit. on p. 56).

[94] Hans Joachim Fitting et al. "EDX depths analysis of MIS-structures". In: *Mikrochimica Acta* 125.1-4 (Mar. 1997), pp. 235–238. ISSN: 0026-3672. DOI: 10.1007/BF01246189 (cit. on p. 56).

[95] Daniel Abou-Ras et al. "Inhomogeneities in Cu(In,Ga)Se2 Thin Films for Solar Cells: Band-Gap Versus Potential Fluctuations". In: *Solar RRL* 2.1 (Jan. 2018), p. 1700199. ISSN: 2367198X. DOI: 10.1002/solr.201700199 (cit. on p. 58).

[96] Peter O. Grabitz et al. "Spatial inhomogeneities in Cu(In,Ga)Se2 solar cells analyzed by an electron beam induced voltage technique". In: *Journal of Applied Physics* 100.12 (Dec. 2006), p. 124501. ISSN: 0021-8979. DOI: 10.1063/1.2402345 (cit. on p. 58).

[97] Thomas Schmid, Norbert Schafer, and Daniel Abou-Ras. "Raman microspectroscopy provides access to compositional and microstructural details of polycrystalline materials". In: *Spectroscopy Europe* 28.5 (2016), pp. 16–20. ISSN: 0966-0941 (cit. on pp. 59, 91).

[98] Wolfram Witte, Robert Kniese, and Michael Powalla. "Raman investigations of Cu(In,Ga)Se2 thin films with various copper contents". In: *Thin Solid Films* 517.2 (Nov. 2008), pp. 867–869. ISSN: 00406090. DOI: 10.1016/j.tsf.2008.07.011 (cit. on pp. 59, 63).

[99] Wolfram Witte et al. "Influence of the Ga Content on the Mo/Cu(In,Ga)Se2 Interface Formation". In: *2006 IEEE 4th World Conference on Photovoltaic Energy Conference*. Vol. 1. IEEE, May 2006, pp. 553–556. ISBN: 1-4244-0016-3. DOI: 10.1109/WCPEC.2006.279515 (cit. on pp. 59, 63).

[100] Pedro Santos et al. "Fabrication of semi-transparent Cu(In,Ga)Se2 solar cells aided by Bromine etching". In: *Thin Solid Films* 770.June 2022 (Apr. 2023), p. 139778. ISSN: 00406090. DOI: 10.1016/j.tsf.2023.139778 (cit. on p. 61).

[101] S. Roy et al. "Characterization of Cu(In,Ga)Se2 films by Raman scattering". In: *Materials Chemistry and Physics* 73.1 (Jan. 2002), pp. 24–30. ISSN: 02540584. DOI: 10.1016/S0254-0584(01)00345-5 (cit. on pp. 63, 73).

[102] Jun-feng Han et al. "Investigation of chalcopyrite film growth at various temperatures: analyses from top to the bottom of the thin films". In: *Journal of Materials Science: Materials in Electronics* 25.5 (May 2014), pp. 2237–2243. ISSN: 0957-4522. DOI: 10.1007/s10854-014-1864-8 (cit. on p. 63).

[103] Dahyun Nam, Jae-ung Lee, and Hyeonsik Cheong. "Excitation energy dependent Raman spectrum of MoSe2". In: *Scientific Reports* 5.1 (Nov. 2015), p. 17113. ISSN: 2045-2322. DOI: 10.1038/srep17113 (cit. on p. 63).

[104] A. H. Goldan et al. "Molecular structure of vapor-deposited amorphous selenium". In: *Journal of Applied Physics* 120.13 (Oct. 2016). ISSN: 0021-8979. DOI: 10.1063/1.4962315 (cit. on p. 63).

[105] T. P. Moffat et al. "Electrodeposition of Cu on Ru Barrier Layers for Damascene Processing". In: *Journal of The Electrochemical Society* 153.1 (2006), p. C37. ISSN: 00134651. DOI: 10.1149/1.2131826 (cit. on p. 64).

[106] E. Camacho-Espinosa, A. I. Oliva-Avilés, and A. I. Oliva. "Effect of the Substrate Cleaning Process on Pinhole Formation in Sputtered CdTe Films". In: *Journal of Materials Engineering and Performance* 26.8 (Aug. 2017), pp. 4020–4028. ISSN: 1059-9495. DOI: 10.1007/s11665-017-2842-0 (cit. on p. 64).

[107] Philip Jackson et al. "Properties of Cu(In,Ga)Se2 solar cells with new record efficiencies up to 21.7%". In: *physica status solidi (RRL) - Rapid Research Letters* 9.1 (Jan. 2015), pp. 28–31. ISSN: 18626254. DOI: 10.1002/pssr.201409520 (cit. on p. 67).

[108] Philip Jackson et al. "Effects of heavy alkali elements in Cu(In,Ga)Se2 solar cells with efficiencies up to 22.6%". In: *physica status solidi (RRL) – Rapid Research Letters* 10.8 (Aug. 2016), pp. 583–586. ISSN: 1862-6254. DOI: 10.1002/pssr.201600199 (cit. on pp. 67, 156).

[109] Bart Vermang et al. "Development of rear surface passivated Cu(In,Ga)Se2 thin film solar cells with nano-sized local rear point contacts". In: *Solar Energy Materials and Solar Cells* 117 (Oct. 2013), pp. 505–511. ISSN: 09270248. DOI: 10.1016/j.solmat.2013.07.025 (cit. on p. 67).

[110] Wei Peng et al. "Reducing nonradiative recombination in perovskite solar cells with a porous insulator contact". In: *Science* 379.6633 (Feb. 2023), pp. 683–690. ISSN: 0036-8075. DOI: 10.1126/science.ade3126 (cit. on p. 67).

[111] D. Rudmann et al. "Efficiency enhancement of Cu(In,Ga)Se2 solar cells due to post-deposition Na incorporation". In: *Applied Physics Letters* 84.7 (Feb. 2004), pp. 1129–1131. ISSN: 0003-6951. DOI: 10.1063/1.1646758 (cit. on pp. 68, 89, 127).

[112] Yazi Wang, Shasha Lv, and Zhengcao Li. "Review on incorporation of alkali elements and their effects in Cu(In,Ga)Se2 solar cells". In: *Journal of Materials Science & Technology* 96 (Jan. 2022), pp. 179–189. ISSN: 10050302. DOI: 10.1016/j.jmst.2020.07.050 (cit. on p. 68).

[113] Lei Tian and Rüdiger Dieckmann. "Bulk diffusion measurements to study the effectiveness of barrier layers: II. Exchange of sodium between liquid crystal display glass substrates with different barrier layers". In: *Journal of Applied Physics* 90.8 (Oct. 2001), pp. 3810–3815. ISSN: 0021-8979. DOI: 10.1063/1.1402151 (cit. on p. 68).

[114] N. Akcay et al. "Characterization of Cu2ZnSnS4 thin films prepared with and without thin Al2O3 barrier layer". In: *Solar Energy* 234.January (Mar. 2022), pp. 137–151. ISSN: 0038092X. DOI: 10.1016/j.solener.2022.01.074 (cit. on p. 68).

[115] William N. Shafarman, Susanne Siebentritt, and Lars Stolt. "Cu(InGa)Se2 Solar Cells". In: *Handbook of Photovoltaic Science and Engineering*. Vol. 346. 2010. Chichester, UK: John Wiley & Sons, Ltd, Mar. 2011, pp. 546–599. ISBN: 9780470721698. DOI: 10.1002/9780470974704.ch13 (cit. on p. 68).

[116] Pyuck-Pa Choi et al. "Comparative atom probe study of Cu(In,Ga)Se2 thin-film solar cells deposited on soda-lime glass and mild steel substrates". In: *Journal of Applied Physics* 110.12 (Dec. 2011). ISSN: 0021-8979. DOI: 10.1063/1.3665723 (cit. on p. 71).

[117] Jinwoo Lee et al. "Effect of Three-Stage Growth Modification on a CIGS Microstructure". In: *IEEE Journal of Photovoltaics* 6.6 (Nov. 2016), pp. 1645–1649. ISSN: 2156-3381. DOI: 10.1109/JPHOTOV.2016.2598264 (cit. on p. 71).

[118] V. Nadenau et al. "Sodium induced secondary phase segregations in CuGaSe2 thin films". In: *Journal of Crystal Growth* 233.1-2 (Nov. 2001), pp. 13–21. ISSN: 00220248. DOI: 10.1016/S0022-0248(01)01554-8 (cit. on p. 71).

[119] M R Balboul et al. "Sodium Induced Phase Segreations in CuGaSe2 and CuInSe2 Thin Films". In: *17th EC Photovoltaic Solar Energy Conferenc, Munich Germany, Oct* (2001), pp. 22–26 (cit. on p. 71).

[120] A. Vladar and M. Postek. "Electron Beam-Induced Sample Contamination in the SEM". In: *Microscopy and Microanalysis* 11.S02 (Aug. 2005), pp. 764–765. ISSN: 1431-9276. DOI: 10.1017/S1431927605507785 (cit. on p. 73).

[121] C. Rincón et al. "Raman spectra of the ordered vacancy compounds CuIn3Se5 and CuGa3Se5". In: *Applied Physics Letters* 73.4 (July 1998), pp. 441–443. ISSN: 0003-6951. DOI: 10.1063/1.121893 (cit. on pp. 73, 124, 125).

[122] Junfeng Han et al. "Raman and XPS studies of CIGS/Mo interfaces under various annealing temperatures". In: *Materials Letters* 136 (Dec. 2014), pp. 278–281. ISSN: 0167577X. DOI: 10.1016/j.matlet.2014.08.087 (cit. on p. 73).

[123] I. P. Kaminow, E. Buehler, and J. H. Wernick. "Vibrational Modes in ZnSiP2". In: *Physical Review B* 2.4 (Aug. 1970), pp. 960–966. ISSN: 0556-2805. DOI: 10.1103/PhysRevB.2.960 (cit. on p. 73).

[124] U. Rau et al. "Oxygenation and air-annealing effects on the electronic properties of Cu(In,Ga)Se2 films and devices". In: *Journal of Applied Physics* 86.1 (July 1999), pp. 497–505. ISSN: 0021-8979. DOI: 10.1063/1.370758 (cit. on p. 74).

[125] D. Braunger et al. "Influence of sodium on the growth of polycrystalline Cu(In,Ga)Se 2 thin films". In: *Thin Solid Films* 361-362 (Feb. 2000), pp. 161–166. ISSN: 00406090. DOI: 10.1016/S0040-6090(99)00777-4 (cit. on p. 75).

[126] Roland Scheer and Hans-Werner Schock. *Chalcogenide Photovoltaics*. Weinheim, Germany: Wiley-VCH Verlag GmbH & Co. KGaA, Feb. 2011. ISBN: 9783527633708. DOI: 10.1002/9783527633708 (cit. on pp. 75, 81, 83).

[127] B. H. Torrie. "Raman and Infrared Spectra of Na2SeO3, NaHSeO3, H2SeO3, and NaH3(SeO3)2". In: *Canadian Journal of Physics* 51.6 (Mar. 1973), pp. 610–615. ISSN: 0008-4204. DOI: 10.1139/p73-080 (cit. on p. 75).

[128] John Wiley Sons Inc. SpectraBase. "SpectraBase Compound ID: BC1pE7zBD5G SpectraBase Spectrum ID: CLdfl1Pbqau". URL: https://spectrabase.com/spectrum/CLdfl1Pbqau. *Last accessed: 2023-10-28*.

[129] John Wiley Sons Inc. SpectraBase. "SpectraBase Compound ID:LruCIP76Zzy SpectraBase Spectrum ID:9Fp1xiU5Xim". URL: https://spectrabase.com/spectrum/9Fp1xiU5Xim. *Last accessed: 2023-09-26*.

[130] Hamda A. Al-Thani et al. "The effect of Mo back contact on Na out-diffusion and device performance of Mo/Cu(In,Ga)Se2/CdS/ZnO solar cells". In: *Conference Record of the IEEE Photovoltaic Specialists Conference* April (2002), pp. 720–723. ISSN: 01608371. DOI: 10.1109/pvsc.2002.1190666 (cit. on p. 76).

[131] Robert V. Forest. "Diffusion of sodium in copper indium gallium diselenide based materials". PhD thesis. University of Delaware, 2015, p. 171. URL: http://udspace.udel.edu/handle/19716/17423 (cit. on pp. 76, 78, 79, 82, 83, 89).

[132] Dimitrios Hariskos and Michael Powalla. "Thermodynamic limitations for alkali metals in Cu(In,Ga)Se 2". In: *Journal of Materials Research* 32.20 (Oct. 2017), pp. 3789–3800. ISSN: 0884-2914. DOI: 10.1557/jmr.2017.394 (cit. on p. 79).

[133] Howard C. Berg. *Random Walks in Biology*. Princeton University Press, Dec. 1984. ISBN: 9781400820023. DOI: 10.1515/9781400820023 (cit. on p. 79).

[134] Anke Laemmle et al. "Investigation of the diffusion behavior of sodium in Cu(In,Ga)Se2 layers". In: *Journal of Applied Physics* 115.15 (2014). ISSN: 10897550. DOI: 10.1063/1.4871457 (cit. on p. 79).

[135] Xiaoli Sun and Zhiguo Wang. "Sodium adsorption and diffusion on monolayer black phosphorus with intrinsic defects". In: *Applied Surface Science* 427 (Jan. 2018), pp. 189–197. ISSN: 01694332. DOI: 10.1016/j.apsusc.2017.08.199 (cit. on p. 80).

[136] E Seebauer. "Estimating surface diffusion coefficients". In: *Progress in Surface Science* 49.3 (July 1995), pp. 265–330. ISSN: 00796816. DOI: 10.1016/0079-6816(95)00039-2 (cit. on p. 80).

[137] F. Hergert et al. "Formation reactions of chalcopyrite compounds and the role of sodium doping". In: *Thin Solid Films* 515.15 (May 2007), pp. 5843–5847. ISSN: 00406090. DOI: 10.1016/j.tsf.2006.12.037 (cit. on p. 81).

[138] Marika Bodegard, Karin Granath, and Lars Stolt. "Growth of Cu(In,Ga)Se2 thin films by coevaporation using alkaline precursors". In: *Thin Solid Films* 361-362 (Feb. 2000), pp. 9–16. ISSN: 00406090. DOI: 10.1016/S0040-6090(99)00828-7 (cit. on p. 81).

[139] Marika Bodegard. "The influence of sodium on the grain structure of CuInSe_2 films for photovoltaic applications". In: *Proc. 12th European Photovoltaic Solar Energy Conference, 1994* (1994), pp. 1743–1746. URL: https://cir.nii.ac.jp/crid/1572261549854625024 (cit. on p. 81).

[140] V. Probst et al. "The impact of controlled sodium incorporation on rapid thermal processed Cu(InGa)Se2-thin films and devices". In: *Proceedings of 1994 IEEE 1st World Conference on Photovoltaic Energy Conversion - WCPEC (A Joint Conference of PVSC, PVSEC and PSEC)*. Vol. 1. IEEE, 1994, pp. 144–147. ISBN: 0-7803-1460-3. DOI: 10.1109/WCPEC.1994.519828 (cit. on p. 81).

[141] Diego Colombara et al. "Deliberate and Accidental Gas-Phase Alkali Doping of Chalcogenide Semiconductors: Cu(In,Ga)Se2". In: *Scientific Reports* 7.1 (Apr. 2017), p. 43266. ISSN: 2045-2322. DOI: 10.1038/srep43266 (cit. on pp. 81, 89, 94, 111, 116, 127, 135).

[142] D. Rudmann et al. "Effects of NaF coevaporation on structural properties of Cu(In,Ga)Se2 thin films". In: *Thin Solid Films* 431-432 (May 2003), pp. 37–40. ISSN: 00406090. DOI: 10.1016/S0040-6090(03)00246-3 (cit. on p. 81).

[143] Stephan Brunken et al. "Co-evaporated CuInSe2: Influence of growth temperature and Na on solar cell performance". In: *2014 IEEE 40th Photovoltaic Specialist Conference (PVSC)*. IEEE, June 2014, pp. 3629–3632. ISBN: 978-1-4799-4398-2. DOI: 10.1109/PVSC.2014.6924893 (cit. on p. 81).

[144] B. Bissig et al. "Effects of NaF evaporation during low temperature Cu(In,Ga)Se2 growth". In: *Thin Solid Films* 582 (May 2015), pp. 56–59. ISSN: 00406090. DOI: 10.1016/j.tsf.2014.11.026 (cit. on p. 81).

[145] S. Puttnins et al. "Effect of sodium on material and device quality in low temperature deposited Cu(In,Ga)Se2". In: *Solar Energy Materials and Solar Cells* 119 (Dec. 2013), pp. 281–286. ISSN: 09270248. DOI: 10.1016/j.solmat.2013.08.029 (cit. on p. 83).

[146] A. Rockett et al. "Na in selenized Cu(In,Ga)Se2 on Na-containing and Na-free glasses: distribution, grain structure, and device performances". In: *Thin Solid Films* 372.1-2 (Sept. 2000), pp. 212–217. ISSN: 00406090. DOI: 10.1016/S0040-6090(00)01028-2 (cit. on p. 83).

[147] J.E. Granata et al. "Quantitative incorporation of sodium in CuInSe2 and Cu(In,Ga)Se2 photovoltaic devices". In: *Conference Record of the Twenty Sixth IEEE*

Photovoltaic Specialists Conference - 1997. IEEE, 1997, pp. 387–390. ISBN: 0-7803-3767-0. DOI: 10.1109/PVSC.1997.654109 (cit. on p. 83).

[148] "Diffusion in metals". In: *Smithells Metals Reference Book*. Ed. by E A Brandes and G B Brook. Seventh Ed. Oxford: Elsevier, 1992, pp. 13–1. ISBN: 978-0-08-051730-8. DOI: 10.1016/B978-0-08-051730-8.50018-2 (cit. on p. 84).

[149] Ramis Hertwig et al. "ALD-ZnMgO and absorber surface modifications to substitute CdS buffer layers in co-evaporated CIGSe solar cells". In: *EPJ Photovoltaics* 11.2020 (Jan. 2020). Ed. by Romain Carron et al., p. 12. ISSN: 2105-0716. DOI: 10.1051/epjpv/2020010 (cit. on p. 84).

[150] John K. Katahara and Hugh W. Hillhouse. "Quasi-fermi level splitting and sub-bandgap absorptivity from semiconductor photoluminescence". In: *Journal of Applied Physics* 116.17 (2014). ISSN: 10897550. DOI: 10.1063/1.4898346 (cit. on p. 87).

[151] Chan Bin Mo et al. "Impact of Buffer Layer Process and Na on Shunt Paths of Monolithic Series-connected CIGSSe Thin Film Solar Cells". In: *Scientific Reports* 9.1 (Mar. 2019), p. 3666. ISSN: 2045-2322. DOI: 10.1038/s41598-019-38945-5 (cit. on p. 88).

[152] Chuen-Lin Tien and Tsai-Wei Lin. "Thermal expansion coefficient and thermomechanical properties of SiNx thin films prepared by plasma-enhanced chemical vapor deposition". In: *Applied Optics* 51.30 (Oct. 2012), p. 7229. ISSN: 1559-128X. DOI: 10.1364/AO.51.007229 (cit. on p. 94).

[153] Friedrich Kessler and Dominik Rudmann. "Technological aspects of flexible CIGS solar cells and modules". In: *Solar Energy* 77.6 (Dec. 2004), pp. 685–695. ISSN: 0038092X. DOI: 10.1016/j.solener.2004.04.010 (cit. on p. 94).

[154] I. R. McKerracher et al. "Thermal expansion coefficients and composition of sputter-deposited silicon oxynitride thin films". In: *Journal of Physics D: Applied Physics* 43.33 (Aug. 2010), p. 335104. ISSN: 0022-3727. DOI: 10.1088/0022-3727/43/33/335104 (cit. on p. 94).

[155] A. Hultqvist et al. "Performance of Cu(In,Ga)Se2 solar cells using nominally alkali free glass substrates with varying coefficient of thermal expansion". In: *Journal of Applied Physics* 114.9 (Sept. 2013), p. 094501. ISSN: 0021-8979. DOI: 10.1063/1.4819802 (cit. on p. 94).

[156] F. Couzinié-Devy, N. Barreau, and J. Kessler. "Re-investigation of preferential orientation of Cu(In,Ga)Se2 thin films grown by the three-stage process". In: *Progress in Photovoltaics: Research and Applications* 19.5 (Aug. 2011), pp. 527–536. ISSN: 1062-7995. DOI: 10.1002/pip.1079 (cit. on p. 94).

[157] Diego Colombara, Billy J. Stanbery, and Giovanna Sozzi. "Revani diffusion model in Cu(In,Ga)Se 2". In: *Journal of Materials Chemistry A* 11.48 (2023), pp. 26426–26434. ISSN: 2050-7488. DOI: 10.1039/D3TA03690A (cit. on p. 94).

[158] Veronika Haug. "Cu(In,Ga)Se2 thin-film solar cells based on a simple sputtered alloy precursor and a low-cost selenization step". In: *Journal of Photonics for Energy* 1.1 (Jan. 2011), p. 018002. ISSN: 1947-7988. DOI: 10.1117/1.3659500 (cit. on p. 95).

[159] Junhyun Park and Woo Kyoung Kim. "Effect of sputtering conditions of co-sputtered Cu–In–Ga precursors on Cu(InGa)Se2 photovoltaic absorber formation". In: *Thin Solid Films* 572 (Dec. 2014), pp. 61–67. ISSN: 00406090. DOI: 10.1016/j.tsf.2014.08.017 (cit. on p. 95).

[160] Ricardo G. Poeira et al. "Direct fabrication of arrays of Cu(In,Ga)Se2 micro solar cells by sputtering for micro-concentrator photovoltaics". In: *Materials & Design* 225 (Jan. 2023), p. 111597. ISSN: 02641275. DOI: 10.1016/j.matdes.2023.111597 (cit. on pp. 104, 106).

[161] S. M. Rossnagel et al. "Collimated magnetron sputter deposition". In: *Journal of Vacuum Science & Technology A: Vacuum, Surfaces, and Films* 9.2 (Mar. 1991), pp. 261–265. ISSN: 0734-2101. DOI: 10.1116/1.577531 (cit. on p. 105).

[162] Zahra Bahari et al. "The equilibrium phase diagram of the copper–indium system: a new investigation". In: *Thermochimica Acta* 401.2 (May 2003), pp. 131–138. ISSN: 00406031. DOI: 10.1016/S0040-6031(02)00500-2 (cit. on p. 108).

[163] C Suryanarayana and Soon-Jik Hong. "Mechanism of low-temperature θ-CuGa2 phase formation in Cu-Ga alloys by mechanical alloying". In: *Journal of Applied Physics* 96.11 (2004), pp. 6120–6126. DOI: 10.1063/1.1808243 (cit. on p. 108).

[164] Roland Mainz et al. "Time-resolved investigation of Cu(In,Ga)Se2 growth and Ga gradient formation during fast selenisation of metallic precursors". In: *Progress in Photovoltaics: Research and Applications* 23.9 (Sept. 2015), pp. 1131–1143. ISSN: 10627995. DOI: 10.1002/pip.2531 (cit. on p. 114).

[165] Yasuhiro Hashimoto et al. "Surface Characterization of Chemically Treated Cu(In,Ga)Se2 Thin Films". In: *Japanese Journal of Applied Physics* 35.Part 1, No. 9A (Sept. 1996), pp. 4760–4764. ISSN: 0021-4922. DOI: 10.1143/JJAP.35.4760 (cit. on pp. 114, 127).

[166] Wolfram Witte et al. "Gallium gradients in Cu(In,Ga)Se2 thin-film solar cells". In: *Progress in Photovoltaics: Research and Applications* 23.6 (June 2015), pp. 717–733. ISSN: 10627995. DOI: 10.1002/pip.2485 (cit. on p. 114).

[167] Jae-Cheol Park et al. "10% efficiency Cu(In,Ga)Se2 solar cell with strongly (220)/(204) oriented Cu-poor absorber layers sputtered using single quaternary

target". In: *Journal of Alloys and Compounds* 812 (Jan. 2020), p. 152065. ISSN: 09258388. DOI: 10.1016/j.jallcom.2019.152065 (cit. on p. 116).

[168] Sanping Wu et al. "Over 12% efficient low-bandgap CuIn(S, Se)2 solar cells with the absorber processed from aqueous metal complexes solution in air". In: *Nano Energy* 62 (Aug. 2019), pp. 818–822. ISSN: 22112855. DOI: 10.1016/j.nanoen.2019.06.010 (cit. on p. 116).

[169] Lung-Hsin Tu, Chung-Hao Cai, and Chih-Huang Lai. "Tuning Ga Grading in Selenized Cu(In,Ga)Se 2 Solar Cells by Formation of Ordered Vacancy Compound". In: *Solar RRL* 5.3 (Mar. 2021), p. 2000626. ISSN: 2367-198X. DOI: 10.1002/solr.202000626 (cit. on p. 117).

[170] Florian Oliva et al. "Optical methodology for process monitoring of chalcopyrite photovoltaic technologies: Application to low cost Cu(In,Ga)(S,Se)2 electrodeposition based processes". In: *Solar Energy Materials and Solar Cells* 158 (Dec. 2016), pp. 168–183. ISSN: 09270248. DOI: 10.1016/j.solmat.2015.12.036 (cit. on p. 119).

[171] Chuan-Ming Xu et al. "Composition dependence of the Raman A1 mode and additional mode in tetragonal Cu–In–Se thin films". In: *Semiconductor Science and Technology* 19.10 (Oct. 2004), pp. 1201–1206. ISSN: 0268-1242. DOI: 10.1088/0268-1242/19/10/006 (cit. on p. 119).

[172] C. Insignares-Cuello et al. "Raman scattering analysis of electrodeposited Cu(In,Ga)Se2 solar cells: Impact of ordered vacancy compounds on cell efficiency". In: *Applied Physics Letters* 105.2 (July 2014), p. 021905. ISSN: 0003-6951. DOI: 10.1063/1.4890970 (cit. on p. 119).

[173] M Marudachalam et al. "Phases , morphology , and diffusion in Cu(Inx,Ga1-x)Se2 thin films". In: *Journal of Applied Physics* 2896.May 2014 (2009). DOI: 10.1063/1.366122 (cit. on p. 120).

[174] Byungwoo Kim and Byoung Koun Min. "Strategies toward highly efficient CIGSe thin-film solar cells fabricated by sequential process". In: *Sustainable Energy and Fuels* 2.8 (2018), pp. 1671–1685. ISSN: 23984902. DOI: 10.1039/c8se00158h (cit. on p. 120).

[175] Thomas P. Weiss et al. "Bulk and surface recombination properties in thin film semiconductors with different surface treatments from time-resolved photoluminescence measurements". In: *Scientific Reports* 9.1 (Mar. 2019), p. 5385. ISSN: 2045-2322. DOI: 10.1038/s41598-019-41716-x (cit. on p. 120).

[176] Jean-François Guillemoles et al. "One step electrodeposition of CuInSe2: Improved structural, electronic, and photovoltaic properties by annealing under high selenium pressure". In: *Journal of Applied Physics* 79.9 (May 1996), pp. 7293–7302. ISSN: 0021-8979. DOI: 10.1063/1.361446 (cit. on p. 121).

[177] T. Wada et al. "Fabrication of Cu(In,Ga)Se2 thin films by a combination of mechanochemical and screen-printing/sintering processes". In: *physica status solidi (a)* 203.11 (Sept. 2006), pp. 2593–2597. ISSN: 1862-6300. DOI: 10.1002/pssa.200669652 (cit. on p. 121).

[178] Sejin Ahn et al. "Effects of selenization conditions on densification of Cu(In,Ga)Se2 (CIGS) thin films prepared by spray deposition of CIGS nanoparticles". In: *Journal of Applied Physics* 105.11 (June 2009). ISSN: 0021-8979. DOI: 10.1063/1.3141755 (cit. on p. 121).

[179] Alexander R. Uhl et al. "Liquid-selenium-enhanced grain growth of nanoparticle precursor layers for CuInSe2 solar cell absorbers". In: *Progress in Photovoltaics: Research and Applications* 23.9 (Sept. 2015), pp. 1110–1119. ISSN: 1062-7995. DOI: 10.1002/pip.2529 (cit. on p. 121).

[180] Grayson M. Ford et al. "CuIn(S,Se)2 thin film solar cells from nanocrystal inks: Effect of nanocrystal precursors". In: *Thin Solid Films* 520.1 (Oct. 2011), pp. 523–528. ISSN: 00406090. DOI: 10.1016/j.tsf.2011.08.007 (cit. on p. 121).

[181] Jonathan J. Scragg. "Studies of Cu2ZnSnS4 films prepared by sulfurisation of electrodeposited precursors". PhD thesis. University of Bath, 2010. URL: https://researchportal.bath.ac.uk/files/187949402/UnivBath_PhD_2010_J_Scragg.pdf (cit. on p. 121).

[182] Bing Li et al. "Smooth Cu electrodeposition for Cu(In, Ga)Se2 thin-film solar cells: Dendritic clusters elimination by Ag buffer layer". In: *Energy Reports* 8 (Nov. 2022), pp. 1847–1852. ISSN: 23524847. DOI: 10.1016/j.egyr.2021.12.079 (cit. on p. 121).

[183] J. Weszka et al. "Raman scattering in In2Se3 and InSe2 amorphous films". In: *Journal of Non-Crystalline Solids* 265.1-2 (Mar. 2000), pp. 98–104. ISSN: 00223093. DOI: 10.1016/S0022-3093(99)00710-3 (cit. on p. 125).

[184] Yun-ju Chu and Ching-hwa Ho. "Amorphous effect on the advancing of structural-phase transition in γ-In2Se3 polycrystalline layers". In: *2015 International Symposium on Next-Generation Electronics (ISNE)*. IEEE, May 2015, pp. 1–3. ISBN: 978-1-4799-4208-4. DOI: 10.1109/ISNE.2015.7131960 (cit. on p. 125).

[185] Diego Colombara et al. "Chemical instability at chalcogenide surfaces impacts chalcopyrite devices well beyond the surface". In: *Nature Communications* 11.1 (July 2020), p. 3634. ISSN: 2041-1723. DOI: 10.1038/s41467-020-17434-8 (cit. on p. 127).

[186] Conrad Spindler. "Optical detection of deep defects in Cu(In,Ga)Se2". PhD thesis. University of Luxembourg, 2018. URL: https://hdl.handle.net/10993/37016 (cit. on p. 137).

[187] A. Khadir. "Simulation of Effects of Defects and Layers Thickness on the Performance of CIGS Solar Cells". In: *Acta Physica Polonica A* 137.6 (June 2020), pp. 1128–1134. ISSN: 1898-794X. DOI: 10.12693/APhysPolA.137.1128 (cit. on p. 141).

[188] Jan Keller et al. "Wide-gap (Ag,Cu)(In,Ga)Se 2 solar cells with different buffer materials—A path to a better heterojunction". In: *Progress in Photovoltaics: Research and Applications* 28.4 (Apr. 2020), pp. 237–250. ISSN: 1062-7995. DOI: 10.1002/pip.3232 (cit. on p. 141).

[189] David Mackay. *Sustainable energy - without the hot air*. Cambridge: UIT Cambridge Ltd., 2009, p. 383. ISBN: 978-0-9544529-3-3 (cit. on p. 145).

[190] E4L Team. "Energy4Life". URL: https://e4l.uni.lu/. *Accessed on 05-03-2024*.

[191] ZenziWerken. "Kids Toy Scale cnc/laser". URL: https://www.thingiverse.com/thing:1643194. *Accessed on 10-09-2022*.

[192] Jan Keller et al. "Effect of Cu Content on Post-Sulfurization of Cu(In,Ga)Se 2 Films and Corresponding Solar Cell Performance". In: *physica status solidi (a)* 216.20 (Oct. 2019), p. 1900472. ISSN: 1862-6300. DOI: 10.1002/pssa.201900472 (cit. on p. 156).

[193] Yu-han Chang et al. "Impact of RbF and NaF Postdeposition Treatments on Charge Carrier Transport and Recombination in Ga-Graded Cu(In,Ga)Se 2 Solar Cells". In: *Advanced Functional Materials* 31.40 (Oct. 2021). ISSN: 1616-301X. DOI: 10.1002/adfm.202103663 (cit. on p. 156).